

AD610738

Band Structure and Surface Effects in Cadmium Sulfide Photoemission Studies

by
Neal B. Kindig

August 1964

Technical Report No. 5201-1

Prepared under
National Science Foundation Grant GP-1033, and
Center for Materials Research Contract
SD 87-4850-47

1 COPY	2	OF	3	100
COPY				\$.50
OFFICE				\$.12

177P

SOLID-STATE ELECTRONICS LABORATORY
STANFORD ELECTRONICS LABORATORIES
STANFORD UNIVERSITY • STANFORD, CALIFORNIA

ARCHIVE COPY



DISCLAIMER NOTICE

THIS DOCUMENT IS THE BEST
QUALITY AVAILABLE.

COPY FURNISHED CONTAINED
A SIGNIFICANT NUMBER OF
PAGES WHICH DO NOT
REPRODUCE LEGIBLY.

ERRATA SHEET

BAND STRUCTURE AND SURFACE EFFECTS IN CADMIUM SULFIDE PHOTOEMISSION STUDIES

Page	76	2nd line from bottom	Eq. (38) instead of Eq. (32).
page	76	Eq. (40)	$= B(\Delta E, \text{etc.}, \text{instead of}$ $= \beta(\Delta E, \text{etc.})$
page	125	Fig. 57	$T(E) = \frac{1}{2} \left[\sqrt{\frac{0.8}{E-6.4}} \right]$ instead of $\sqrt{\frac{0.8}{E-7.2}}$.
page	137	Fig. 65	Label abscissa $(E-h\nu)$ instead of $N(E_1-h\nu)$.
page	138	line 8	$E = 11.0 \text{ eV}$ instead of $E_b = 11.0 \text{ eV}$.
page	143	Fig. 68	Under SAMPLE, next to AC, should read AIR CLEAVED instead of AIR CLEANED.

SEL-64-095

BAND STRUCTURE AND SURFACE EFFECTS IN CADMIUM SULFIDE
PHOTOEMISSION STUDIES

by

Neal B. Kindig

August 1964

Reproduction in whole or in part
is permitted for any purpose of
the United States Government.

Technical Report No. 5201-1

Prepared under
National Science Foundation
Grant GP-1033
and
Center for Materials Research
Contract SD 87-4850-47

Solid-State Electronics Laboratory
Stanford Electronics Laboratories
Stanford University Stanford, California

ABSTRACT

Photoemission measurements have been made on single crystals of cadmium sulfide which were cleaved and tested in high vacuum at photon energies between 7.2 and 11.6 eV. The electron affinity is found to be 4.8 eV. Additional measurements have been made in an extended range from 6 to 21.2 eV using surfaces cleaved in air or in low vacuum and tested in low vacuum. The apparatus for cleaving and measuring photoemission is described.

Important features of the band structure are deduced from the energy distribution and quantum yield measurements. Two conduction band maxima are located about 6.7 and 8.2 eV above the top of the valence band. Two valence band maxima are located about 1.2 and 9.4 eV below the top of the valence band. The density of states is determined by assuming that direct conservation of crystal momentum is not an important selection rule. The results are used to study optical excitation processes and escape of electrons. In particular, the optical conductivity calculated from the density of states agrees with experimental values.

The effects of surface conditions on photoemission from cadmium sulfide have been studied by comparing measurements made on samples cleaved in high vacuum with the corresponding results from surfaces prepared by other techniques. The energy distribution curve is shown to be a sensitive tool for studying surface conditions. The theoretical effect of band bending on energy distributions is considered.

CONTENTS

	<u>Page</u>
I. INTRODUCTION	1
II. EXPERIMENTAL TECHNIQUES	5
A. Introduction	5
B. Cadmium Sulfide Sample Preparation	6
1. Orientation	6
2. Electrical Contacts	11
3. Cleaving	12
C. Sealed Phototube	16
D. High Vacuum Test Chamber	19
E. Windowless Experiments	26
F. Light Source and Electrical Measurements	28
1. Monochromator and Light Source	28
2. Measurement of the Quantum Yield	32
3. Measurement of Energy Distributions	38
4. Work Function and Surface Properties of the Collector	41
III. THEORY OF PHOTOEMISSION FROM SEMICONDUCTORS	46
A. Introduction	46
B. The Photoemission Equations	49
C. Absorption Coefficient, Attenuation Length, and Threshold Function	56
1. Absorption Coefficient and Optical Conductivity	56
2. Attenuation Length for Excited Electrons	58
3. The Threshold Function	61
D. The Density of States from Energy Distribution Curves	62

CONTENTS (Continued)

	<u>Page</u>
E. The Effect of Band Bending on Photoemission	70
1. Survey	70
2. The Bending Distribution Function	72
3. The Energy Distribution Curve with Band Bending	77
4. Quantitative Estimates of the Effects of Band Bending on Energy Distribution Curves	77
a. Exponential Potential-Versus- Distance Relation	78
b. Linear Potential-Versus- Distance Relation	82
c. Special Potential-Versus Distance Relation	85
F. The Effect of Electron-Electron Scattering on Photoemission from Semiconductors	85
IV. EXPERIMENTAL RESULTS OF PHOTOEMISSION FROM CdS INTERPRETED IN TERMS OF BULK PROPERTIES	89
A. Test Samples and Procedures	89
B. The Measured Energy Distribution of Photoemitted Electrons	91
1. Introduction	91
2. Determination of the Absolute Energy Scale	91
3. High-Vacuum-Cleaved (VC) CdS	94
4. Low-Vacuum-Cleaved (LVC) CdS	100
5. CdS Sealed Tubes (T)	106
6. Air Cleaved (AC) CdS	106
C. The Measured Band Structure of CdS Compared with Reflection Data	108
D. The Calculated Band Structure of CdS	111
E. Details of the Density of States of CdS	111
F. Optical Conductivity ($\omega\epsilon_2$) of CdS	116

CONTENTS (Continued)

	<u>Page</u>
G. The Quantum Yield	118
1. Measured Yield	118
2. Calculated Yield Curves	123
H. The Calculated Energy Distribution of Photoemitted Electrons	128
I. The Effects of Scattering	130
1. General Discussion of Effects	130
2. The Loss of High Energy Electrons Due to Scattering	131
3. The Energy Distribution of Once- Scattered Electrons	135
V. EXPERIMENTAL RESULTS OF PHOTOEMISSION FROM CdS INTERPRETED IN TERMS OF SURFACE PROPERTIES	140
A. Control of Surface Conditions	140
B. Effects of Exposure to Air - Simulation of the Sealed Phototube	141
C. Surface Effects on the Low-Vacuum-Cleaved Sample	149
D. Exposure of CdS to N ₂ and O ₂	151
E. The Effect of Ultraviolet Radiation	152
F. Conclusions About Surface Studies	154
VI. CONCLUSIONS	154
REFERENCES	159

TABLE

Table

1. Data on CdS Test Samples	90
---------------------------------------	----

ILLUSTRATIONS

<u>Figure</u>		<u>Page</u>
1	Range of photon energies and pressures for photoemission measurements on CdS	7
2	The wurtzite crystal structure	9
3	X-ray diffraction (Laue) pattern of the [0001] plane of CdS	9
4	Rotational orientation of CdS about the c axis from the Laue pattern	10
5	CdS cube with In contact and Ni back plate (three times actual size)	10
6	Air-cleaving mechanism	13
7	High-vacuum-cleaving mechanism	15
8	High-vacuum-cleaving mechanism and electron collector for photoemission measurements . . .	15
9	Sealed photodiode with cleaved CdS sample (1.2 x 1.2 cm) and LiF window	17
10	Test chamber (back view) and pumping equipment for photoemission measurements . . .	21
11	LiF window sealed to 0.010-in. silver expansion ring and gasket (actual size) . .	21
12	Pump station controls for the high-vacuum test chamber	23
13	Block diagram of high-vacuum test chamber and pumping equipment	23
14	Valves and gas control equipment for high-vacuum test chamber	25
15	Ring for introduction of probes and filters .	27
16	Electron collector and emitter assembly for the windowless experiments	27
17	Block diagram of the vacuum monochromator and light source	29

ILLUSTRATIONS (Continued)

<u>Figure</u>		<u>Page</u>
18	Hydrogen lamp spectrum	31
19	Experimental system for measuring quantum yield	33
20	LiF window transmission curve	33
21	Apparatus for applying sodium salicylate Coatings	37
22	Circuit for measuring electron energy distributions in the vacuum ultraviolet . . .	39
23	Energy distributions for determining scattering of electrons as a function of O_2 pressure	42
24	Fowler plot used to determine the work function of an aluminum collector	43
25	Energy level diagram for cutoff (a) and saturation (b) of photoemission current	45
26	Spatial diagram showing photon and power absorption in a solid	51
27	Energy versus distance diagram for optical absorption in a solid	53
28	E versus k diagram for absorption by direct (d) indirect (i) and nondirect (n) transitions	59
29	Comparison of corrected Monte Carlo calculations with age theory	63
30	Diagram illustrating calculation of energy distributions from the densities of states . .	65
31	Energy versus distance diagram for a solid with band bending	73
32	Use of the bending distribution function to relate energy distributions for bent and flat bands	79

ILLUSTRATIONS (Continued)

<u>Figure</u>		<u>Page</u>
33	Bending distribution functions for exponential dependence of energy on distance	81
34	Average energy (a), shift of average energy (b), and standard deviation (c) of the distribution function for exponential bands	81
35	Energy versus distance diagram and the corresponding bending distribution function for the case of a constant electric field . .	83
36	Bending distribution function calculated from data of Dousmanis and Duncan	87
37	Energy level diagram for electron-electron scattering and pair production in a semiconductor	87
38	Absolute energy scales for photoemission from semiconductors	93
39	Energy distributions from high-vacuum-cleaved CdS.	96
40	Energy distributions from high-vacuum-cleaved CdS as a function of $E_p - h\nu$	99
41	Energy distributions from low-vacuum-cleaved CdS	101
42	Energy distributions from low-vacuum-cleaved CdS	101
43	Energy distributions from low-vacuum-cleaved CdS	103
44	Energy distributions from low-vacuum-cleaved CdS	103
45	Energy distributions from low-vacuum-cleaved CdS	105

ILLUSTRATIONS (Continued)

<u>Figure</u>		<u>Page</u>
46	Energy distributions from low-vacuum-cleaved CdS	105
47	Energy distributions from the CdS phototube .	107
48	Energy levels of maxima in the CdS density of states	110
49	Reflection as a function of photon energy (Walker and Osantowski)	110
50	The calculated band structure of ZnS (Herman and Skillman)	113
51	The density of states of CdS	115
52	Ratios determining the shape of peaks in the CdS density of states as a function of photon energy	117
53	Graphical illustration of the procedure for calculating optical conductivity, yield and energy distributions from the density of states	119
54	Comparison of the measured and the calculated optical conductivity ($\omega\epsilon_2$) of CdS	119
55	The measured absolute quantum yield of high-vacuum-cleaved CdS	121
56	The measured absolute quantum yield of low-vacuum-cleaved CdS	121
57	Comparison of the measured and calculated absolute yield of CdS	125
58	Calculated absorption above and below the vacuum level	126
59	The absorption length $1/\alpha$ in CdS as a function of photon energy	126
60	Comparison of measured and calculated energy distributions	129

ILLUSTRATIONS (Continued)

<u>Figure</u>		<u>Page</u>
61	Graphical relation between the attenuation length $L(E)$, the elastic scattering mean free path l_p , and the inelastic scattering mean free path l_e	132
62	The integrated scattering probability for CdS	132
63	Graphical illustration of the attenuation of high energy electrons due to scattering . .	134
64	Hypothetical illustration of the effect of variations in absorption length on the calculated energy distributions	134
65	Measured energy distributions at 16.3 and 21.2 eV compared with the calculated energy distribution of once-scattered electrons	137
66	The ratio of peak heights in the energy distributions for low-vacuum-cleaved CdS at $E_b = 0.9$ and 2.4 eV	139
67	Hypothetical energy distribution of once-scattered electrons	139
68	Comparison of energy distributions at $h\nu = 10.8$ eV from CdS surfaces prepared by different methods	143
69	Comparison of absolute quantum yield curves from CdS surfaces prepared in different ways	147
70	Comparison of energy distributions from high-vacuum-cleaved and low-vacuum-cleaved CdS at $h\nu = 10.8$ eV	150
71	Comparison of the effects of exposing CdS to O_2 or N_2 for a short time	153
72	Comparison of energy distributions at $h\nu = 8.0$ and 11.2 eV from a freshly cleaved CdS surface, the same surface exposed to nitrogen, and the same surface exposed to oxygen after the nitrogen was removed	153

ILLUSTRATIONS (Continued)

Figure

Page

- 73 The effect of ultraviolet radiation
on photoemission from a sealed phototube
for $h\nu = 8 \text{ eV}$ 155

LIST OF SYMBOLS

B	bending distribution function
df	differential photon flux per unit energy range per unit length
dF	differential photon flux per unit length
dn	differential number of generated electrons per unit energy range per unit length
e	electronic charge
E	electron energy referred to the top of the valence band (referred to the corresponding bulk value in band bending discussions)
E'	electron energy referred to the top of the valence band (band bending discussion)
E'	energy of excited electron before scattering (scattering discussion)
E _A	magnitude of electron affinity
E _b	electron energy in the vacuum referred to the collector
E _{b co}	cutoff electron energy in the vacuum
E _{b s}	saturation electron energy
E _F	energy of the Fermi level referred to the top of the valence band

LIST OF SYMBOLS (Continued)

E_G	magnitude of the band gap energy
\mathcal{E}	electric field strength
F	photon flux
F_i	incident photon flux
F_r	reflected photon flux
F_t	transmitted photon flux (at the surface)
g	generation rate per unit energy range of once-scattered electrons
$h\nu$	photon energy
$\hbar\omega$	photon energy
k	extinction coefficient
\bar{k}	crystal momentum
l_e	inelastic scattering mean free path
l_p	elastic scattering mean free path
L	attenuation length
n	number of electrons per unit energy range arriving at a unit area of the surface
n_b	number of electrons per unit energy range arriving at a unit area of the surface (with band bending)
N	complex index of refraction
$N(E)$	number of photoemitted electrons per unit area per unit energy range
N_c	conduction band density of states
N_s	surface charge density
N_v	valence band density of states
p	momentum

LIST OF SYMBOLS (Continued)

p_c	critical momentum
p_o	excitation probability per unit of final energy range
p_s	inelastic scattering probability
p_l	electron escape probability
P_o	integrated excitation probability
P_s	integrated inelastic scattering probability
q	electronic charge
\vec{r}	vector distance
R	reflectivity
\vec{S}	poynting vector
T	threshold function
v_g	group velocity
x	length
Y	quantum yield
z_o	impedance of free space
α	absorption coefficient
$1/\alpha$	absorption length
α'	absorption per unit energy range
α_a	absorption above the vacuum level
α_b	absorption below the vacuum level
$\beta = \alpha + 1/L$	reciprocal of the combined characteristic length for absorption and escape
γ	reciprocal of the characteristic length for exponential dependence of band bending

LIST OF SYMBOLS (Continued)

ΔE	energy as a function of distance for a bent band, referred to the bulk energy
ΔE_m	difference between the surface and the bulk potential for bent bands
ϵ	dielectric constant
ϵ_2	imaginary dielectric constant
η	real index of refraction
λ	wavelength
ν	frequency
σ	optical conductivity ($\omega\epsilon_2$)
σ'	optical conductivity per unit energy range
τ	electron lifetime for inelastic scattering
ϕ_m	collector (metal) work function
ϕ_s	collector (semiconductor) work function
ψ	Bloch wave

ACKNOWLEDGMENT

The author wishes to express his appreciation to Professor W. E. Spicer for excellent advice and steady encouragement throughout the course of this work. He wishes to thank Professor R. H. Bube for helpful suggestions and for careful reading of the manuscript. He also wishes to thank Phillip McKernan and Nick Andrews for work on the phototubes and test chamber, and C. N. Berglund for setting up much of the electronic instrumentation and for many helpful discussions. In addition he is grateful for the assistance of Mrs. Marjolaine Andrews in preparing the manuscript.

I. INTRODUCTION

Semiconducting II-VI compounds have been the subject of considerable investigation in recent years since they provide a potentially useful class of electronic materials that have only begun to be exploited. In contrast with the elemental semiconductors silicon and germanium, and to a lesser extent the III-V compounds, the energy band structure of the II-VI compounds are not well understood at energies much larger than the band gap. Therefore, a systematic study of the band structure of these compounds by photoemission techniques is expected to produce much new information about their electronic properties. Properties which can be studied by photoemission include band structure, optical transitions and selection rules, electron scattering, surface effects, and relationship between photoemission and optical properties. Cadmium sulfide (CdS) has been chosen for the initial photoemission studies, since a large body of auxiliary experimental and theoretical knowledge is available and the technology for producing large single crystals is well developed.

Photoemission from CdS has been studied experimentally by several investigators. Shuba [Ref. 1] investigated the yield and energy distribution of photoemitted electrons from CdS in the range of photon energies from 5 to 6.5 eV. The layers were reported to consist of fine, dispersed hexagonal and cubic modifications of CdS formed by evaporation. If special precautions are not taken, CdS is known to decompose during

evaporation. Shuba's results have been discussed by Spicer [Ref. 2]. More recently, Scheer and van Laar [Ref. 3] have investigated photoemissive yield near the threshold for both CdTe cleaved in vacuum and CdS broken in air and then measured in the vacuum. Bibik [Ref. 4] has attempted to lower the photoemissive threshold by deposition of BaO on the surface. Photoemission studies have been undertaken here on single crystals of CdS which have been cleaved in high vacuum to obtain clean surfaces. The maximum photon energy at which measurements can be made has been extended significantly to 21.2 eV.

The optical properties of CdS have been measured in several different experiments. Reflection measurements have been made on CdS layers evaporated by special techniques by Cardona [Refs. 5 and 6], who used polarized or unpolarized light to a maximum photon energy of about 9 eV. Walker and Osantowski [Refs. 7 and 8] have measured reflection to photon energies of about 25 eV from single crystals of CdS which were cleaved in air. They have used the resulting data to calculate the optical constants. Hall [Ref. 9] has measured the optical absorption through evaporated layers of CdS to a photon energy of about 6 eV. Bube [Ref. 10] has studied photoconductivity and related phenomena. All of these measurements can be used to determine important features of the band structure of CdS related to the separation between energy levels, and they can be used in conjunction with photoemission measurements to establish absolute energy levels.

The information obtained from photoemission measurements can be distorted as a result of band bending and physical or chemical phenomena which are related to surface conditions. Williams [Ref. 11] has studied the effects of various gases on the surface by means of surface photovoltage measurements. Contact potential changes in the presence of light have also been studied by Wlerick [Ref. 12] using an electron beam technique. Photochemical reactions have been reported by Bøer [Ref. 13] based on resistance measurements in the presence or absence of light at various temperatures. These surface-related effects must be understood to allow interpretation of the results of photoemission measurements. In some cases, photoemission can be used to study these phenomena.

Theoretical investigations of the band structure of CdS have been made by Herman [Ref. 14] who used an OPW method without the introduction of spin orbit splitting. Recently, he has investigated the results of spin orbit splitting on the band structure [Ref. 15]. Birman [Refs. 16-19] has studied the effects of crystal symmetry on band structure, optical transitions, and selection rules in materials with the wurtzite structure (e.g. CdS).

From theoretical considerations it is evident that the Bloch representation is not adequate to represent the valence band in materials with small hole mobilities [Refs. 20-22]. Mort and Spear [Ref. 23] have found that the hole mobility of CdS is of the order of $10 \text{ cm}^2/\text{volt-sec}$ independent of temperature.

Spicer [Ref. 24] has suggested on the basis of experimental evidence that direct conservation of crystal momentum (\bar{k} vector) may not be required for optical transitions in materials with low hole mobility. Additional experimental evidence with which to check the band structure calculations and the requirements for conservation of crystal momentum for optical transitions in CdS can be obtained from the photoemission data.

Scattering of optically excited electrons as they escape from a material can significantly affect the results of photoemission measurements. Apker, Tift, and Dickey [Ref. 25] suggested a method for detecting the onset of pair production in semiconductors. Spicer [Ref. 26] has used energy distribution curves to determine the mean free path for pair production. Williams [Ref. 27] has studied the effect of high electric fields on voltage breakdown in CdS. He found that breakdown is due to tunneling and not to avalanche effects. Information about electron scattering processes can be obtained from photoemission measurements on CdS.

Many of the experimental techniques developed for studying CdS are applicable to similar photoemission studies of the other II-VI compounds. Therefore, an effort has been made to understand a large variety of secondary phenomena associated with the experiments, and to extend the measurements over as large a range of photon energies and physical environments as possible. The experimental techniques are reported in Chapter II. The applicable theory is presented in Chapter III and the experimental results appear in Chapters IV and V along with their

interpretation. Conclusions drawn from this work and suggestions for further work are contained in Chapter VI.

II. EXPERIMENTAL TECHNIQUES

A. INTRODUCTION

Photoemission measurements have been made on single crystals of CdS on which a clean surface was obtained by cleaving in an ultra-high vacuum system. The photon energies which can be used for the measurements are limited at the low end of the range by the energy barrier against emission (band gap plus electron affinity) and at the high end of the range by either the LiF window (in a high vacuum experiment) or the monochromator plus light source (in lower vacuum experiments). The various arrangements and their characteristic ranges of pressure and photon energy are illustrated in Fig. 1. The diagram indicates the approximate pressure (ordinate) which can be achieved in the sample chamber for each type of experiment and the corresponding range of photon energies (abscissa) which can be used. The factors which limit both pressure and photon energy are indicated.

The photoemitting surface must be carefully prepared to avoid conditions which may lead to chemical reactions, severe nonstoichiometry or other conditions which may modify the photoemission characteristics. Cleaved surfaces have been used to obtain all of the experimental results reported here. Initial measurements have been made on samples cleaved in air and sealed into a glass phototube after baking for a minimum of eight hours at 140°C . A test chamber has been designed in

which CdS samples can be cleaved consistently in a vacuum of less than 10^{-9} torr. At this pressure, several minutes are required before enough gas atoms or molecules can strike the surface to form a monolayer. If every particle which strikes the surface does not stick, a much longer time will be required. Provisions have been made to admit high purity gas into the system so that the effect of the gas on the surfaces can be determined. Experimental studies have been extended into the far vacuum ultraviolet region beyond the cutoff of LiF in the range of photon energies from 11.6 to 21.2 eV by using a windowless monochromator system in which the sample is exposed to a pressure of approximately 10^{-4} torr. This pressure is produced by the gas (hydrogen, helium, or neon) used to operate the lamp. An attempt to reduce the electron affinity of CdS by adding Cs to the surface was unsuccessful due to a reaction between Cs and JdS.

Absolute quantum yield has been measured by a dc method, and the energy distribution of photoemitted electrons has been measured by an ac method. Possible sources of distortion have been investigated, including the effect of the geometrical configuration, the effect of a gaseous atmosphere in the inter-electrode space, and the effect of stray fields.

B. CADMIUM SULFIDE SAMPLE PREPARATION

1. Orientation

The clean surfaces necessary for reliable photoemission measurements have been obtained by cleaving the CdS crystal

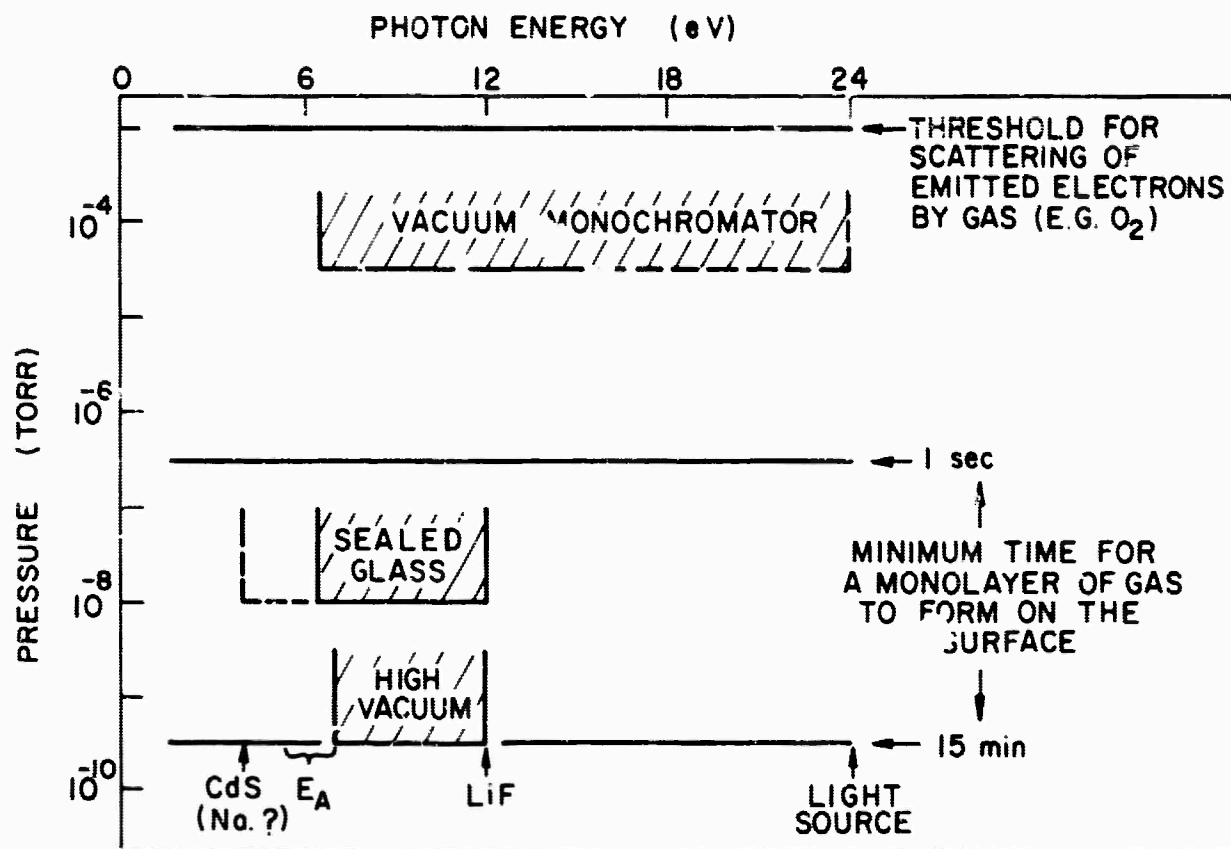


FIG. 1. RANGE OF PHOTON ENERGIES AND PRESSURES FOR PHOTO-EMISSION MEASUREMENTS ON CdS.

in vacuum or in air. A square surface with a minimum area of 1 cm^2 is required by the optics of the available vacuum monochromator. Prior to being cleaved, the samples were cubes with edges at least 1 cm in length. To successfully cleave a crystal of this size it is necessary to accurately locate the c and a axes of the hexagonal wurtzite structure by x-ray diffraction techniques. The basic cell of the wurtzite structure is shown in Fig. 2 [Ref. 28]. The approximate orientation is established on samples which have a fractured or broken surface by visual observation of apparent easy cleavage planes which usually lie parallel to the c axis ([0001] direction). The crystal is mounted on a goniometer mount with the (0001) plane nearly perpendicular to the x-ray beam. The exact location of the (0001) plane is then established by standard x-ray techniques [Ref. 29], and a face is cut parallel to the (0001) plane. A Laue x-ray diffraction pattern for CdS with the proper orientation is shown in Fig. 3. Before the crystal is removed from the goniometer mount, lines are scribed in the sawed surface corresponding to the lines in the film plate holder, to establish the rotational orientation of the crystal with respect to the film. Faces are then sawed perpendicular to the original (0001) cut, parallel to the $(10\bar{1}0)$ and the $(1\bar{2}10)$ planes as shown in Fig. 4. The cube of CdS with accurately oriented faces is then completed by one additional cut parallel to the (0001) plane. Figure 5 shows a cube of CdS to which electrical contacts have been attached.

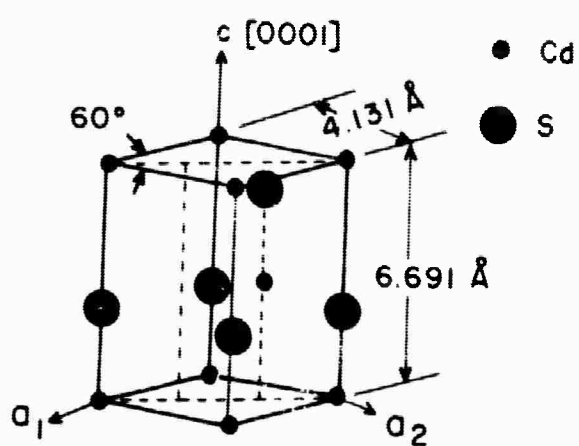


FIG. 2. THE WURTZITE CRYSTAL STRUCTURE.

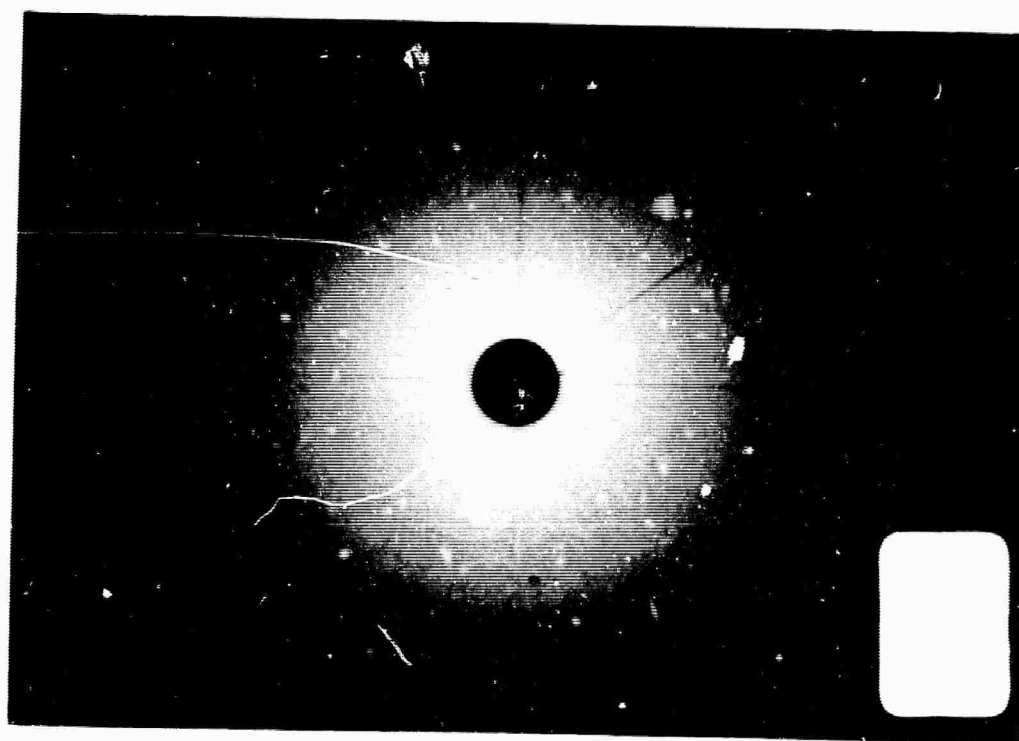


FIG. 3. X-RAY DIFFRACTION (LAUE) PATTERN OF THE $[0001]$ PLANE OF CdS .

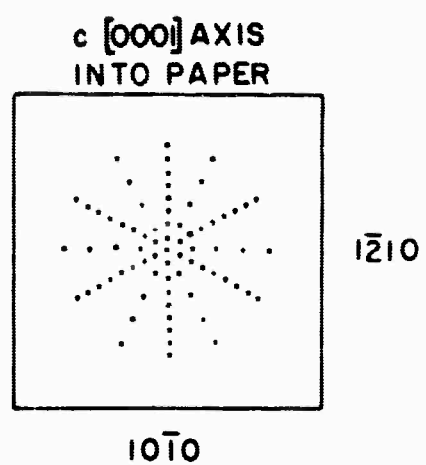


FIG. 4. ROTATIONAL
ORIENTATION OF CdS
ABOUT THE c AXIS FROM
THE LAUE PATTERN.

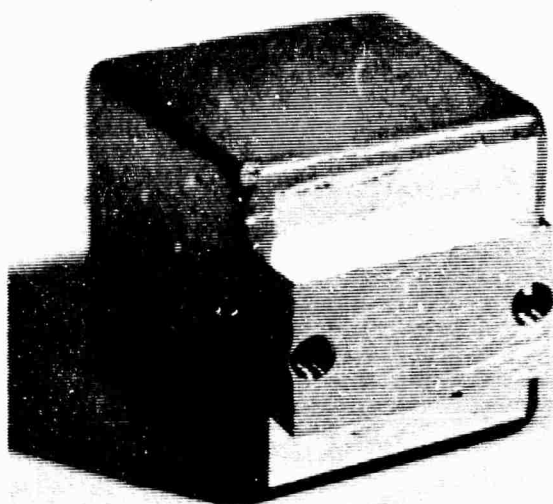


FIG. 5. CdS CUBE WITH In
CONTACT AND Ni BACK PLATE
(THREE TIMES ACTUAL SIZE).

2. Electrical Contacts

Electrical contact and mechanical support is established by bonding a small nickel plate or sheet to the CdS surface with indium. Prior to application of the contact, the edges of the cube are rounded to a radius of about .010" to minimize the distorted electric fields which may appear in the vicinity of sharp corners during the retarding potential measurements. Indium is then evaporated in a vacuum of 10^{-7} torr on the appropriate CdS surface, which is at room temperature, through a mask somewhat smaller than the face of the cube. For cleaving in the $(10\bar{1}0)$ plane the indium is evaporated on the $(10\bar{1}0)$ face of the cube, and for cleaving in the $(1\bar{2}10)$ plane the indium is evaporated on the $(1\bar{2}10)$ plane. After the sample is removed from the vacuum, a nickel contact is clipped to the indium coated face with a tungsten spring. The assembly is then inserted into a furnace operating at a temperature of 400°C through which a reducing atmosphere is flowing (90% N_2 - 10% H_2). The sample remains in the furnace for a period of 2.5 minutes (a time which has been determined empirically) until the sample temperature rises to approximately $200\text{--}250^{\circ}\text{C}$. If the assembly remains in the furnace for too short a time, the indium fails to melt and no contact is established; if the assembly remains in the furnace for too long a time, the indium becomes brittle and tends to flake off the CdS. Contacts have been placed on opposite faces or on a single face, depending on the intended use of the crystal.

3. Cleaving

Previously reported methods for cleaving small samples of CdS depend on splitting the crystal with the impact of a wedge [Ref. 30] or on bending a thin filament of the material until it breaks [Ref. 31] to obtain the desired surface. For a crystal with a large (1 cm^2) surface area used in these experiments, impact methods of cleaving are not applicable since they cause the crystal to shatter or to break in an unpredictable cleavage plane. In addition, it is doubtful if the relatively weak indium contacts could withstand the impact. The crystal is mounted in such a way that it can be moved into the electrical collector after cleaving with the cleaved surface normal to the path of the incident light. The mount must be placed so that it is not illuminated by the light source during the measurements. To overcome the cleaving difficulties and to meet the other requirements of the system, a cleaving mechanism has been developed which uses opposing knife edges between which the sample is squeezed with a slow uniform application of force until it splits in the desired cleavage plane.

The mechanism used for cleaving in air is shown in Fig. 6. The jaws of a standard bench vise have been modified so that stainless steel razor blades which are mounted opposite each other move in the same plane. A line has been scribed on the base plate designed for use with the cleaving mechanism to aid in visual alignment of the crystal. Cleaving is accomplished by tightening the screw until the sample splits.

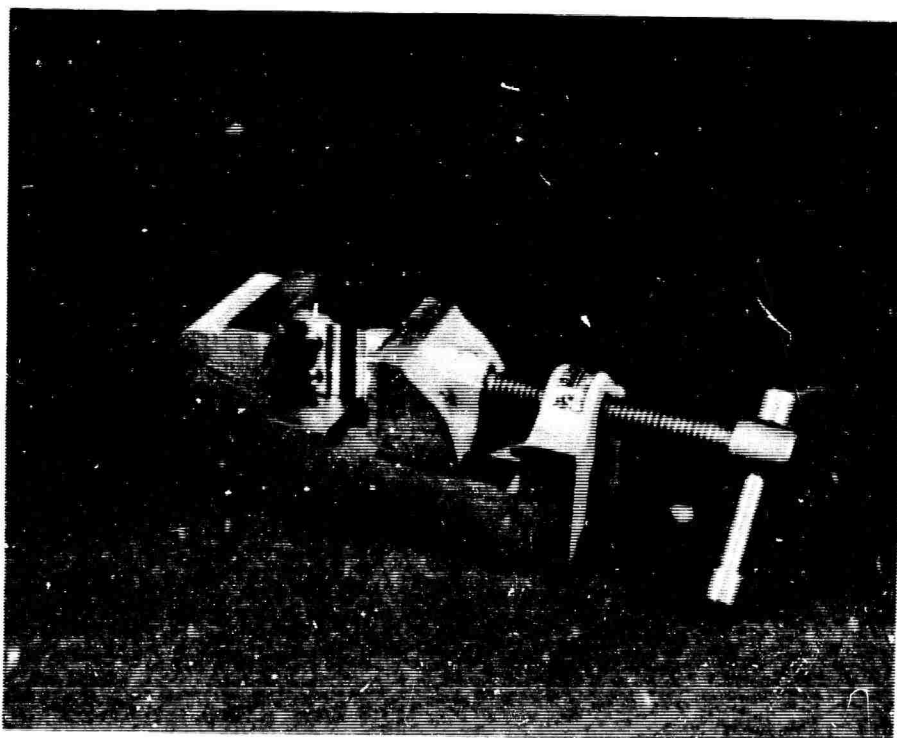


FIG. 6. AIR-CLEAVING MECHANISM.

The electrical contact and mounting wire assembly is attached to the sample prior to cleaving. The emitter assembly is connected into the measuring circuit after cleaving, by means of screws or by spot welding.

The vacuum cleaving mechanism is shown in schematic form in Fig. 7. A photograph of the mechanism is shown in Fig. 8. Approximately 80% of the attempted cleavages have been successful. The unsuccessful attempts usually resulted from attempting to break off a slab thinner than 1.5 to 2 mm. In the vacuum cleaving mechanism, the sample (A, Fig. 7) is mounted on a shaft (B) which extends through the center post (C) of the cleaving jaws (D) and through the tube (E) which is rigidly connected to the flange (F) at the movable end of a stainless steel bellows (G). A spacer (H) is mounted at the opposite end of the tube in such a way that it moves back and forth as the flange (and tube) is moved. The spacer can move freely in a direction perpendicular to the axis of the tube so that it automatically centers between the inclines (I). The shaft and tube are not connected during the cleaving operation. The crystal is properly positioned between the razor blades (J) with the c axis oriented as shown. Cleaving is accomplished by moving the flange to the rear by means of the wing nut (K) which presses against the yoke (L) and the back flange of the chamber (M). The spacer (H) forces the inclines apart and causes the razor blades to squeeze the sample until it splits along the desired cleavage plane. After cleaving, the shaft is connected to the tube by means of a

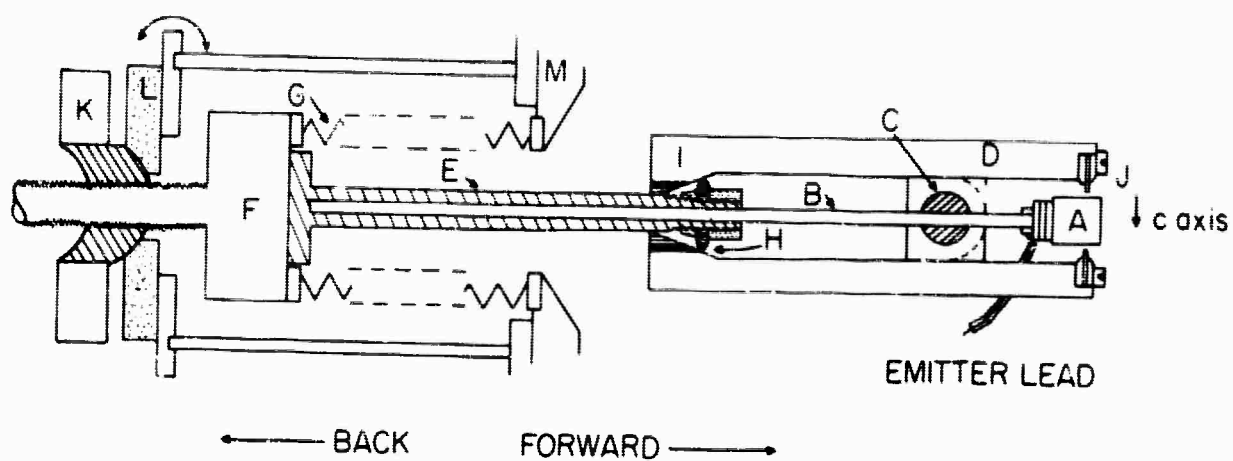


FIG. 7. HIGH-VACUUM-CLEAVING MECHANISM.

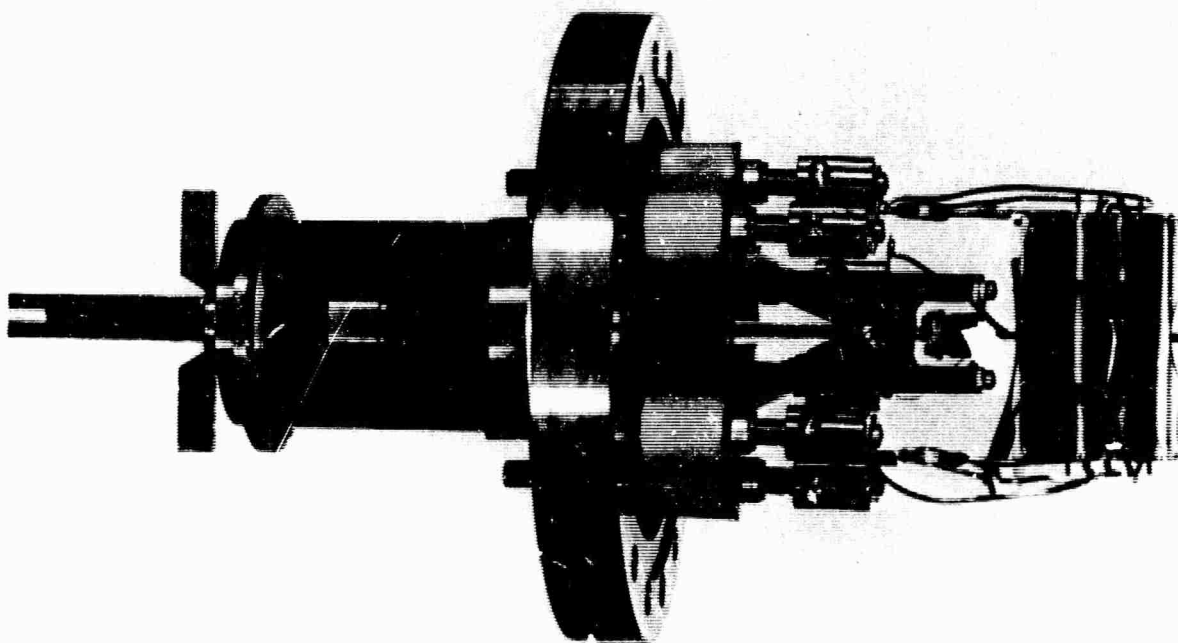


FIG. 8. HIGH-VACUUM-CLEAVING MECHANISM AND ELECTRON COLLECTOR FOR PHOTOEMISSION MEASUREMENTS.

magnetic latch, and then the sample is moved forward into the electron collector. A more recent design uses two bellows which transmit the linear motions to the cleaver and the test sample independently, allowing easier control of the sample position. Either cleaving mechanism can be operated any desired number of times without bringing the test chamber back to air pressure. The collector assembly in Fig. 8 is discussed in detail in Sec. D.

C. SEALED PHOTOTUBE

A CdS sample cleaved in air and sealed into a pyrex glass envelope as shown in Fig. 9 has been used for the initial photo-emission experiments. Ultraviolet light is admitted through a 1-in.-diameter LiF window which is mounted by a method described by Berglund [Ref. 32]. The CdS sample is mounted by means of two .040-in. nickel rods which extend from the nickel contact on the crystal to the pins on the uranium glass header. The collector can is made of .005-in. nichrome sheet which is rolled into a $1\frac{1}{2}$ -in.-diameter cylinder with a 1-in.-diameter hole through which light is admitted. The ends of the cylinder are closed with flat sheets of the same material and the entire collector assembly is cleaned by degreasing and then by firing in a hydrogen atmosphere for ten minutes at 1000°C . The collector assembly is then spot welded to the pins in the opposite uranium glass header and the envelope is assembled.

The tube is processed on a liquid-nitrogen-trapped oil

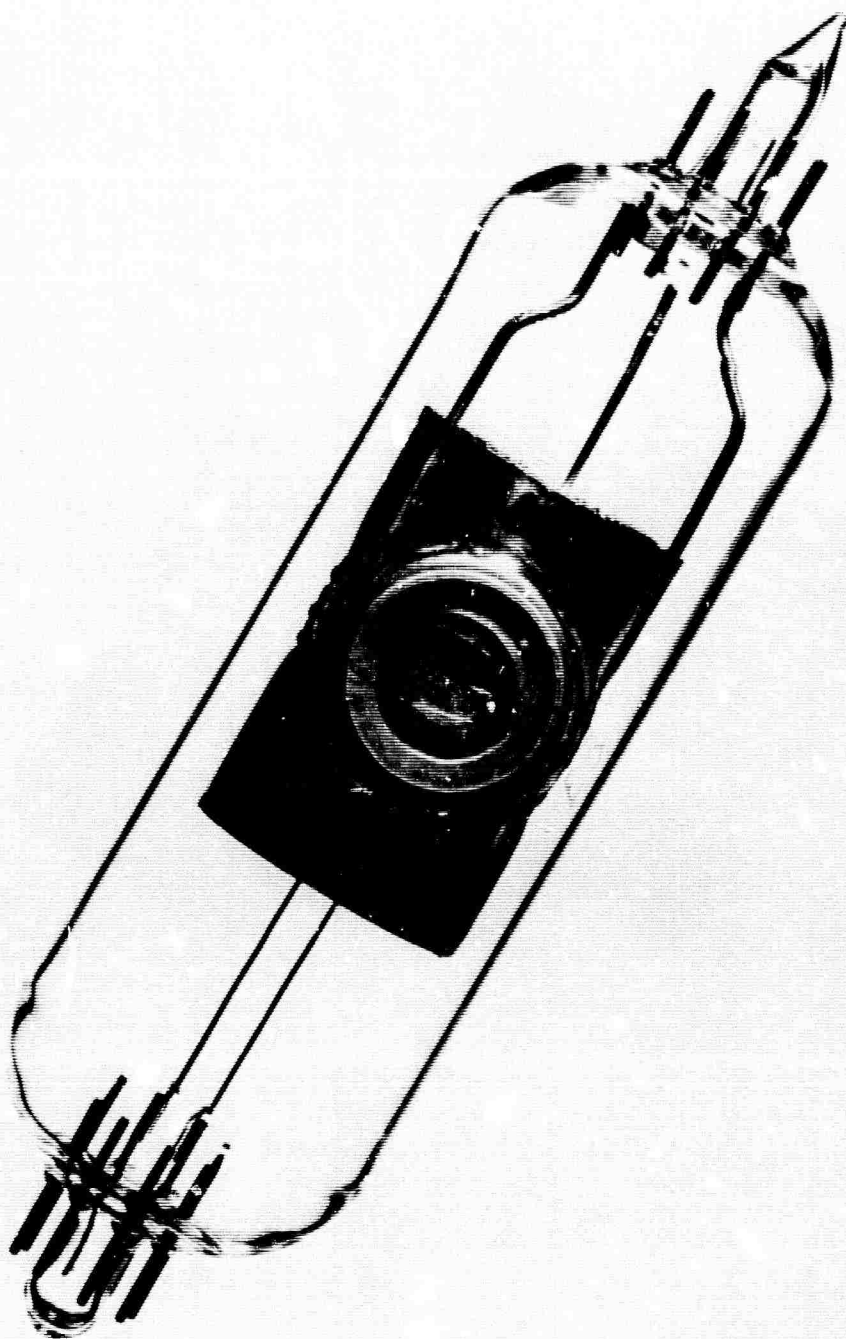


FIG. 9. SEALED PHOTODIODE WITH CLEAVED CdS SAMPLE
(1.2×1.2 cm) AND LiF WINDOW.

diffusion pump system by baking at 140°C until the pressure is reduced to the 10^{-8} torr range. This takes about eight hours. The tube is tipped off and sealed after it has cooled to room temperature.

An attempt has been made to lower the electron affinity of CdS by depositing a monolayer of cesium on the surface. A phototube similar to the one previously described has been constructed with "cesium" channels containing Cs_2CrO_4 , a shield to prevent direct exposure of the test sample to the cesium, and a wire mesh attached to the same header as the collector to allow easy circulation of the cesium. The tube was processed as before except that an attempt was made to deposit a monolayer of Cs on the CdS surface prior to the sealing operation. The current through the cesium channel is slowly increased until photoemission is observed from the shield to one of the unused pins in the header. Then photoemission from the collector and the sample is observed alternately as a function of time as more Cs is generated. The emission from the collector rises slowly to a peak value and then decreases. At this time the current to the Cs channels is reduced to zero and the tube is sealed after the pressure drops to the low 10^{-8} torr range.

The attempt to lower the electron affinity of CdS with Cs was unsuccessful because of a chemical reaction. The reaction was verified in two different ways. First, the color of the cleaved CdS surface changed noticeably from orange to black after exposure to Cs. Second, the structure in energy distribution curves made on the cesiated sample was completely different

from the structure in curves at the same photon energies for freshly cleaved CdS.

D. HIGH VACUUM TEST CHAMBER

The high vacuum test chamber designed by the author has been fabricated by Varian Associates of Palo Alto, California, and is shown in Fig. 10. The cleaving mechanism and test sample holder is mounted on the specially designed 6-in. OD back flange. Linear motion is transmitted through a stainless steel bellows which is restrained against the pull of the vacuum by a threaded shaft and wing nut. The operation of the cleaving mechanism is described in Sec. B3.

Electrical connections (see Fig. 8) are made to the collector, the emitter, and the aluminum evaporators by means of six $\frac{1}{4}$ -in.-diameter electrical leads through ceramic insulators mounted in the back flange. The emitter is connected to one of the electrical leads with a 0.005-in.-diameter annealed copper wire. The wire is insulated with segmented quartz sleeves to prevent shorting to the cleaving mechanism, and it is positioned so that the insulators are outside the collector. The collector is made of 0.005-in. nichrome sheet rolled into a $1\frac{1}{2}$ -in.-diameter cylinder with 1-in.-diameter holes on opposite sides used for admitting light and for inserting the sample into the collector can. The holes can be masked by means of magnetically operated swinging doors which prevent chips of CdS from flying into the collector can during the cleaving operation and which mask the test sample and LiF

window while aluminum is evaporated on the collector can. The collector is supported by three nichrome leads attached to the electrical leads. The electrical continuity of two of these leads is broken by means of glass beads in series so that the electrical connections can be used for other purposes. The third lead provides electrical connection to the collector.

In order to insure a uniform collector work function, aluminum has been evaporated on the inner surface of the collector after the system has been evacuated to less than 10^{-9} torr. During evaporation the pressure remains below 10^{-7} torr. The evaporators are made by interweaving 0.010-in. aluminum wire in a $\frac{1}{2}$ -in.-long coil of 0.010-in. tungsten wire.

A $1\frac{1}{2}$ -in.-diameter pyrex glass viewing port is attached to the top of the test chamber to allow visual control of the cleaving operation. Another flange is provided for attaching an ion gauge or other auxiliary equipment which may be required.

Light from the monochromatic source is admitted to the test chamber through a 1-in.-diameter, $1/16$ -in. to $1/8$ -in.-thick, cleaved LiF window. This window is sealed to a specially designed silver gasket which has been machined to have the profile of the standard gaskets used with the Varian Conflat flange as shown in Fig. 11. The window is prepared for sealing by sandblasting a $1/8$ -in. ring on the edge of one surface with fine alumina powder. The silver gasket is prepared by annealing in a hydrogen furnace for ten minutes at 750°C . While hot, the painted areas of the window and the silver gasket are tinned with silver chloride which melts at approximately 500°C . Then

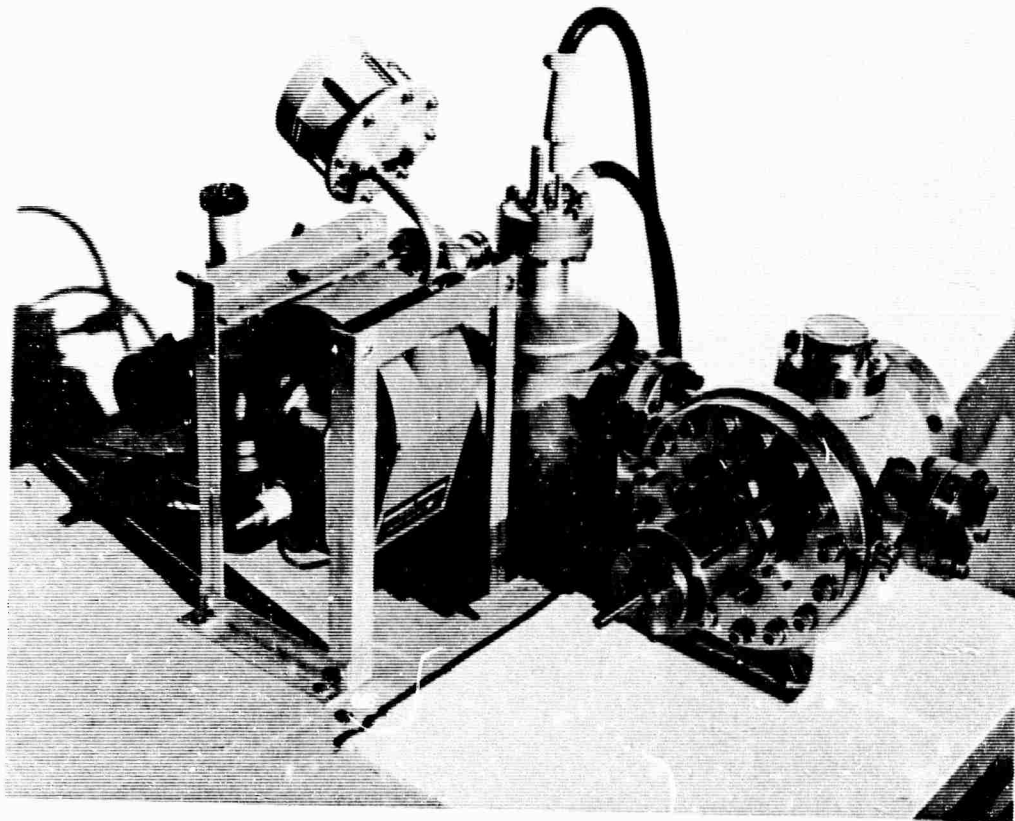


FIG. 10. TEST CHAMBER (BACK VIEW) AND PUMPING EQUIPMENT FOR PHOTOEMISSION MEASUREMENTS. (Photo courtesy of Varian Assoc.)

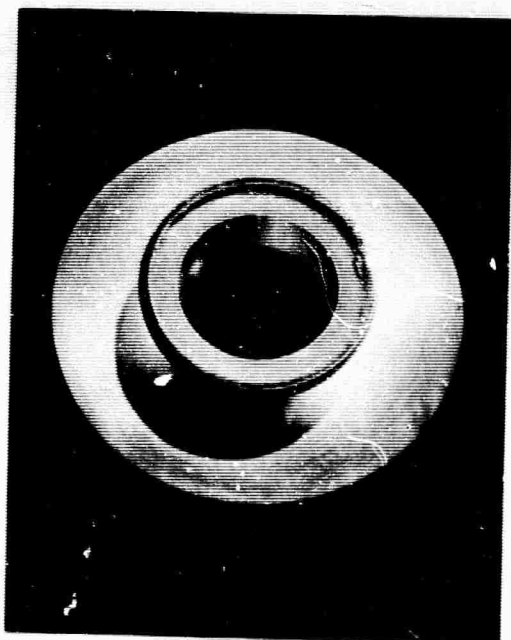


FIG. 11. LiF WINDOW SEALED TO 0.010-in. SILVER EXPANSION RING AND GASKET (ACTUAL SIZE).

the window is placed in the silver gasket and the temperature is raised until the silver chloride just melts. Additional silver chloride is painted around the seal and the oven is allowed to cool overnight.

The LiF window is attached to the front flange of the test chamber by tightening the six bolts on the periphery of the flange. A new window assembly can be installed in a few minutes by removing and reconnecting the flange. All of the high vacuum tests reported in this experiment have been made using a single LiF window. This window has been subjected to differential pressures as large as atmospheric pressure in either direction without damage to the seal. The only precaution taken was to change the differential pressure slowly over a period of a few minutes using a leak valve.

The high vacuum test chamber and its associated pumping equipment is mounted on a mobile stand, shown in Fig. 12, which can be raised or lowered on screws to the correct position for attachment to the vacuum monochromator. The stand contains all of the pump station controls and an oven controller which is used for temperature regulation when the test chamber is baked.

A block diagram of the vacuum chamber and the Varian VacIon pumping system is shown in Fig. 13. The test chamber is evacuated through a $1\frac{1}{2}$ -in.-diameter port to which a titanium sublimation pump and an 8 lit/sec VacIon pump are attached. The titanium evaporators in the sublimation pump are positioned to prevent line-of-sight evaporation into the test chamber. The VacIon pump is positioned so that ions cannot move directly

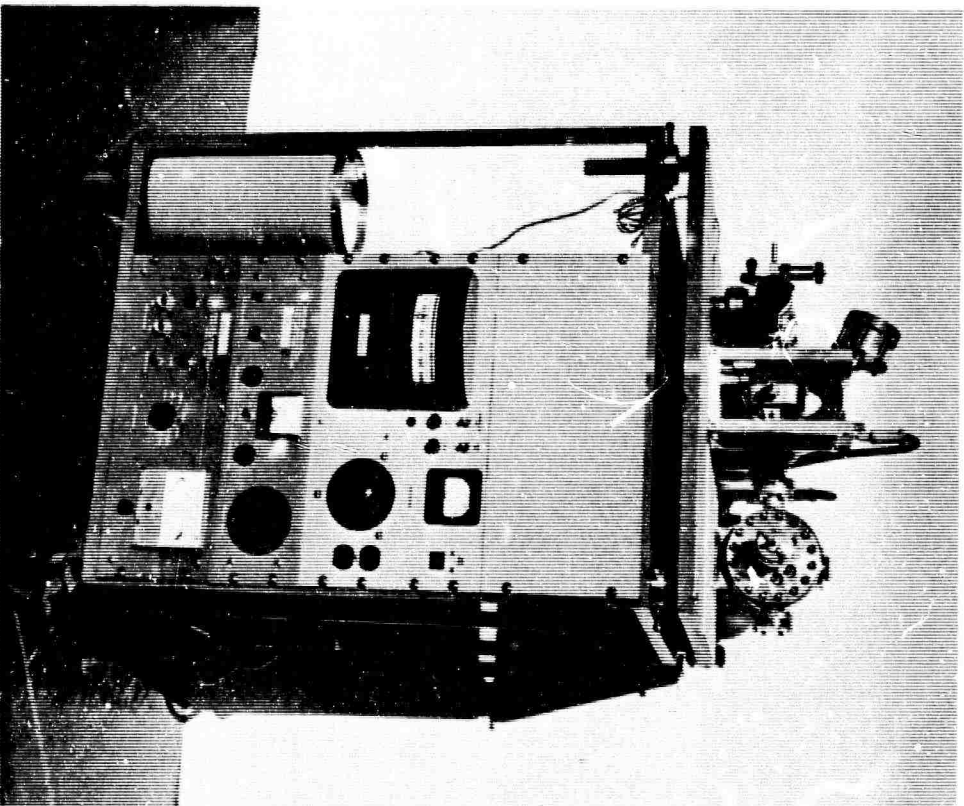


FIG. 12. PUMP STATION CONTROLS FOR THE HIGH-VACUUM TEST CHAMBER. (Photo courtesy of Varian Assoc.)

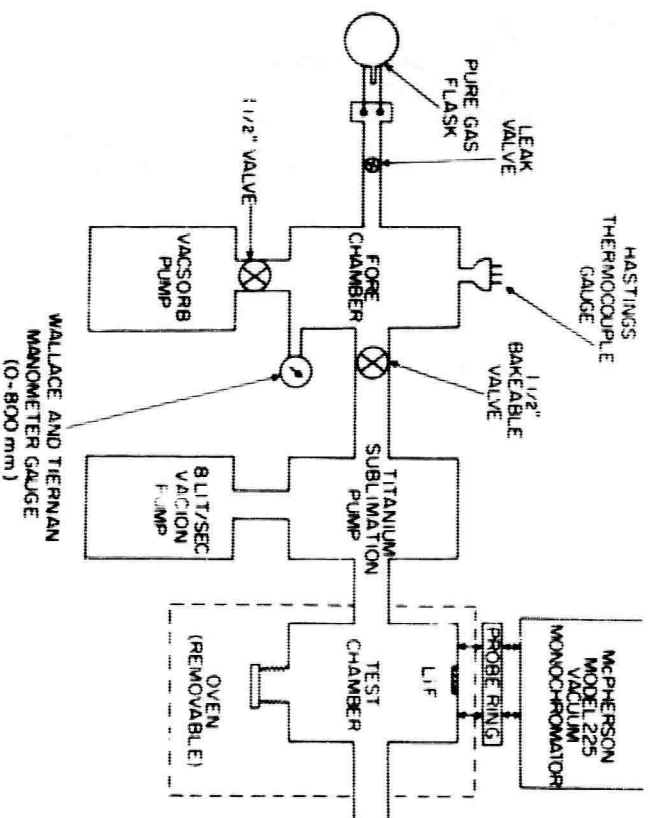


FIG. 13. BLOCK DIAGRAM OF HIGH-VACUUM TEST CHAMBER AND PUMPING EQUIPMENT.

into the test chamber. The entire high vacuum region of the test chamber is isolated from the forechamber by a bakeable valve which has a copper gasket. The high vacuum region of the test chamber enclosed by the dotted line in Fig. 13 can be baked at a temperature up to 400°C by using a portable temperature-regulated oven. The indium contacts used with CdS limit the bake out temperature to about 140°C when the sample is in the chamber. The remaining portions of the high vacuum region, including the bakeable valve, can be baked at temperatures up to 400°C by using heater strips. Pressures below 10^{-9} torr can easily be achieved in the high vacuum region of the system.

The forechamber region is also shown in block diagram form in Fig. 13, and is pictured in Fig. 14. The forechamber is connected to the Varian VacSorb pump through a $1\frac{1}{2}$ -in. valve with a viton gasket. A leak valve with a viton seat is also attached to the forechamber. This valve is used to return the system to air pressure at a controlled rate to prevent damage to the LiF window. In addition it can be used to introduce controlled pressures of high purity gasses for environmental experiments from one liter pyrex glass containers which are attached by a quick connector with a viton O-ring (not shown). The pressure in the forechamber is monitored with a Wallace and Tiernan manometer gauge for pressures between 10 torr and air pressure (760 torr). A Hastings thermocouple gauge is used for pressures down to about 10^{-3} torr (1 micron) which is the low pressure limit of the roughing pump.

The entire region between the test chamber and the vacuum

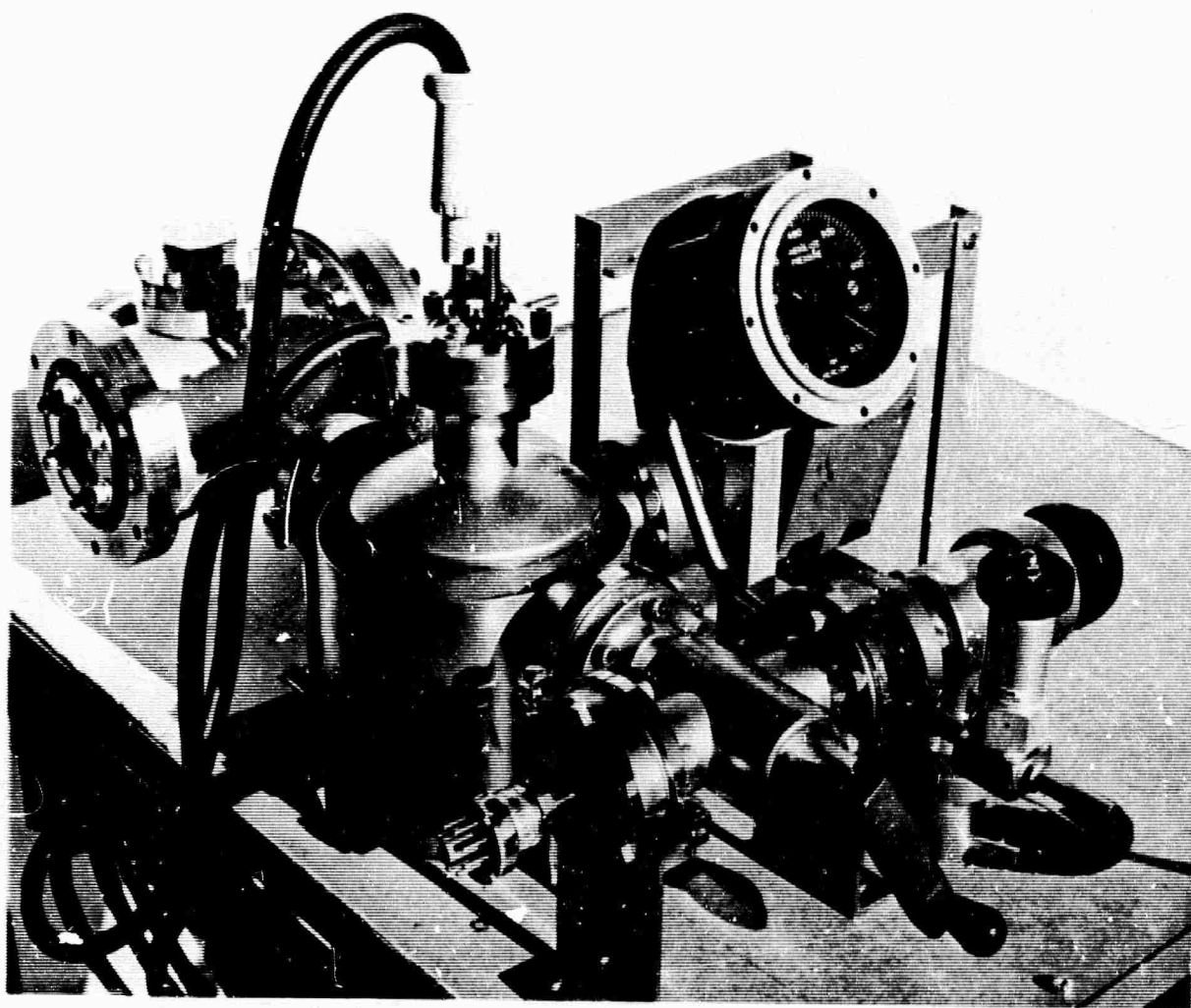


FIG. 14. VALVES AND GAS CONTROL EQUIPMENT FOR HIGH-VACUUM TEST CHAMBER. (Photo courtesy of Varian Assoc.)

monochromator must be evacuated to pressures below 10^{-4} torr to allow propagation of the ultraviolet light. Therefore, the front flange of the test chamber is machined so that it will seal against the O-ring in the exit port of the monochromator. Provisions have been made for measuring the intensity of the incident light and for inserting filters in the beam, by using sliding vacuum seals through a 7/8-in.-thick brass ring as shown in Fig. 15. One face of the ring is machined to seal against the vacuum monochromator, and the other face contains an O-ring which seals against the flange on the test chamber.

E. WINDOWLESS EXPERIMENTS

The range of photon energies available for measurements when using the sealed phototube or the high vacuum test chamber is limited by the upper transmission cutoff energy of LiF at 11.7 eV. The measurements have been extended to photon energies as high as 21.2 eV by removing all windows from the light path between the lamp and the test sample. The test sample and the collector are supported from a 7-pin tube header which can be plugged into a ceramic tube socket in the test chamber, as shown in Fig. 16. The dimensions of the collector and the methods of mounting the sample are similar to those used with the high vacuum test chamber. The samples tested have been cleaved in air and mounted in the test chamber, in which a pressure of approximately 10^{-4} torr is maintained by the 6-in. oil diffusion pump in the vacuum monochromator.

Measurements have also been made using the high vacuum

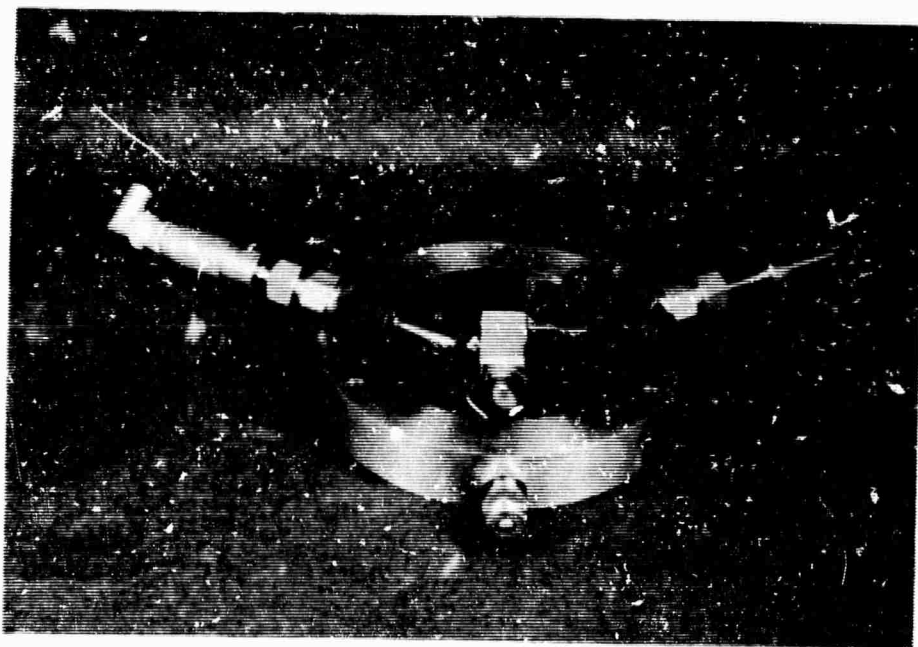


FIG. 15. RING FOR INTRODUCTION OF PROBES
AND FILTERS.

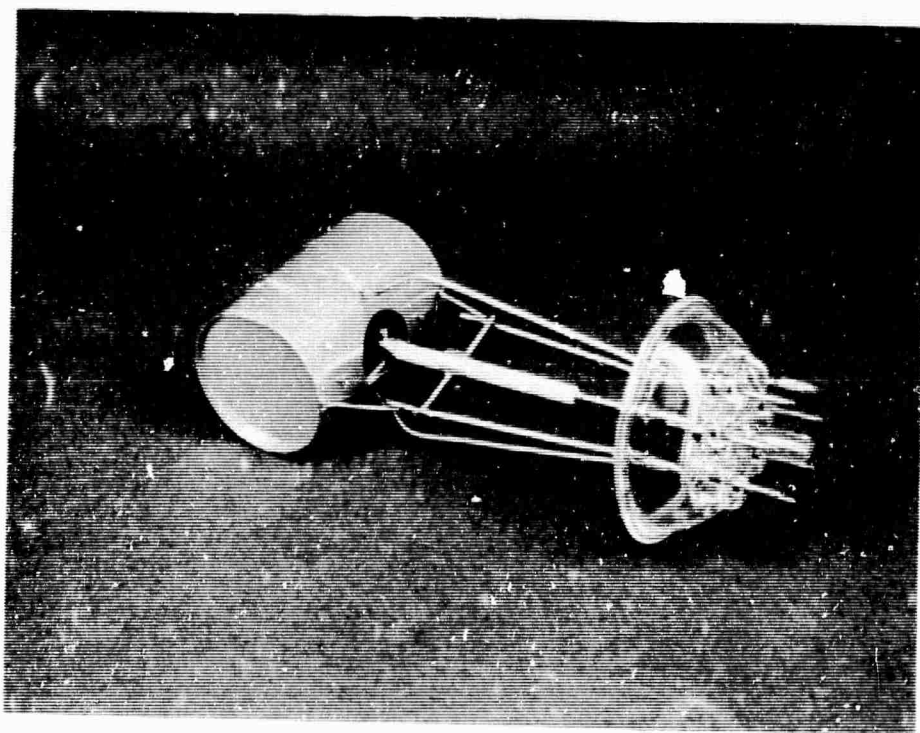


FIG. 16. ELECTRON COLLECTOR AND EMITTER
ASSEMBLY FOR THE WINDOWLESS EXPERIMENTS.

test chamber with the VacIon pumping port sealed off and the LiF window removed. The test sample is cleaved after the test chamber has been evacuated to a pressure of about 10^{-4} torr. The atmosphere in the test chamber is determined by the type of gas with which the lamp is operated. The test chamber is carefully cleaned after this type of measurement before it is reconnected to the VacIon pumping system to minimize the possibility of contamination due to the oil diffusion pump.

The results of windowless measurements are compared with the results of measurements made in the clean high vacuum system to determine the effect of surface contamination on the validity of the results. The comparisons are discussed in detail in Chapter V.

F. LIGHT SOURCE AND ELECTRICAL MEASUREMENTS

1. Monochromator and Light Source

Monochromatic light for all of the measurements has been provided by a McPherson Model 225 1-meter vacuum ultraviolet scanning monochromator in the system illustrated in Fig. 17. Light is generated in a Hinterregger type gas discharge lamp operated in the dc mode from a variable 3000-v, 500-ma power supply which has a peak-to-peak ripple of approximately 5%. The lamp is stabilized by means of a series resistance and reactance as indicated. Use of the dc mode reduces the 120-cps ripple below that of an ac source by at least 10 db.

Gas for the lamp is supplied through a two stage regulator to a manifold at a pressure of about 20 lb above atmospheric pressure. Gas flows from the manifold into the lamp

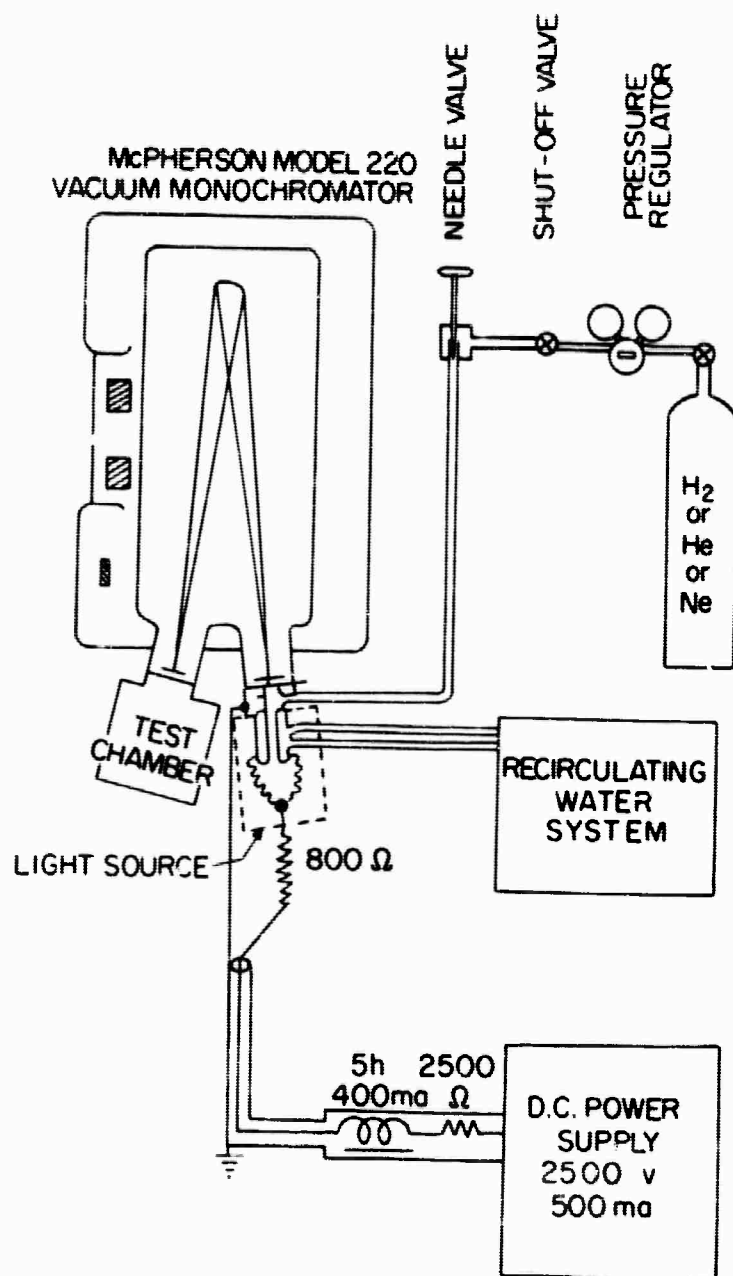


FIG. 17. BLOCK DIAGRAM OF THE
VACUUM MONOCHROMATOR AND LIGHT
SOURCE.

chamber through a good quality Nupro needle valve, and is then pumped through the input slits into the main chamber of the monochromator where it is removed by the 6-in. oil diffusion pump. The lamp is operated at pressures in the range from 1 to 5 torr with the exact pressure controlled by the needle valve to give the most stable operation of the lamp. The pressure in the main chamber is maintained at about 3×10^{-4} torr.

A hydrogen discharge operating at a pressure of 2 torr and a current of 300 ma has been used for measurements in the range of photon energies up to about 14.5 eV. A typical hydrogen lamp spectrum is shown in Fig. 18. Measurements have been made at higher photon energies using the strong spectral lines of neon at 16.8 eV and of helium at 21.2 eV.

The diffraction grating is ruled with 600 lines/mm and is blazed at 1500 \AA , giving a horizontal dispersion of 16.6 \AA per mm of slit width. The horizontal aperture is $\phi 10$ and the vertical is $\phi 15$. The horizontal slit width may be adjusted continuously by means of a micrometer from 10 microns to 2 mm. The slit height may be fixed at any value up to 2 cm. The exit slit housing may be sealed off from the main chamber using flat valves, so that the sample chamber can be changed or adjustments can be made without returning the entire monochromator to air pressure. This allows continuous operation of the lamp. A separate roughing pump is used to evacuate the slit housing, and in some cases the test chamber, before it

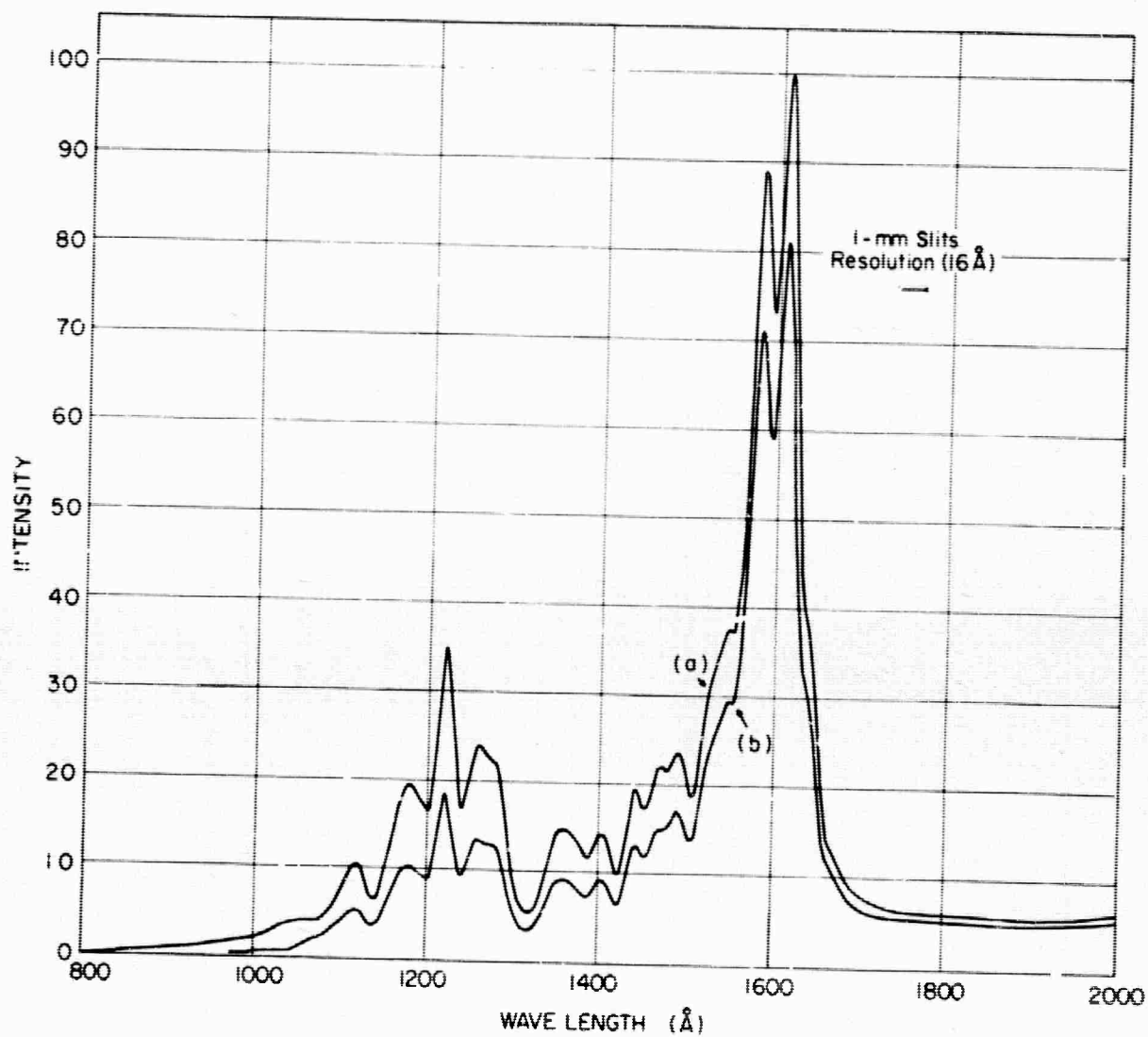
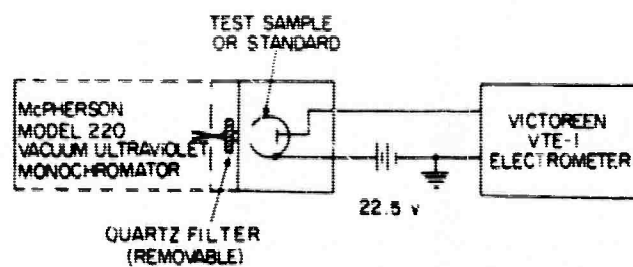


FIG. 18. HYDROGEN LAMP SPECTRUM.
 (a) Without LiF window. (b) With LiF window.

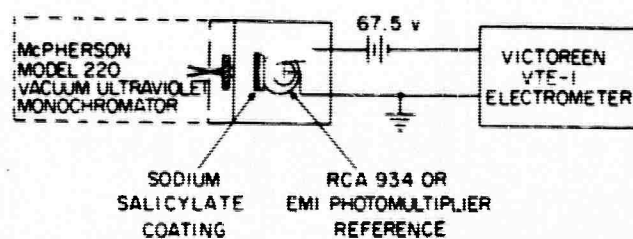
is reconnected to the main chamber.

2. Measurement of the Quantum Yield

The system used for measurement of quantum yield using the vacuum monochromator is shown in Fig. 19. The collector of the photodiode is biased positive with respect to the emitter by a potential corresponding to about twice the highest photon energy to be used. The bias voltage is made large enough so that the photocurrent will not be space-charge limited and so that electrons emitted from the collector due to light reflected from the emitter will have insufficient energy to reach the emitter. Excessive voltage must be avoided to prevent high field emission from corners of the sample. The dc photocurrent from the test sample is measured with an electrometer and compared with the current from a detector with constant quantum efficiency. (The detector which consists of a sodium salicylate coating on a photodiode or photomultiplier will be described in detail in a following paragraph.) This measurement establishes the relative quantum yield over the entire energy range. A correction must be made for the transmission of the LiF window, for which a typical transmission curve is shown in Fig. 20. A transmission curve is measured for each LiF window prior to installation, and it has been established that the installation process does not significantly change the transmission characteristics. A correction is also made for reflection from the CdS sample using the reflection data measured by Walker and Osantowski [Ref. 7]. The absolute yield is established by comparing the current from the test sample at a given photon



MEASUREMENT OF PHOTOEMISSION FROM THE TEST SAMPLE



MEASUREMENT OF PHOTOEMISSION FROM THE REFERENCE

FIG. 19. EXPERIMENTAL SYSTEM FOR MEASURING QUANTUM YIELD.

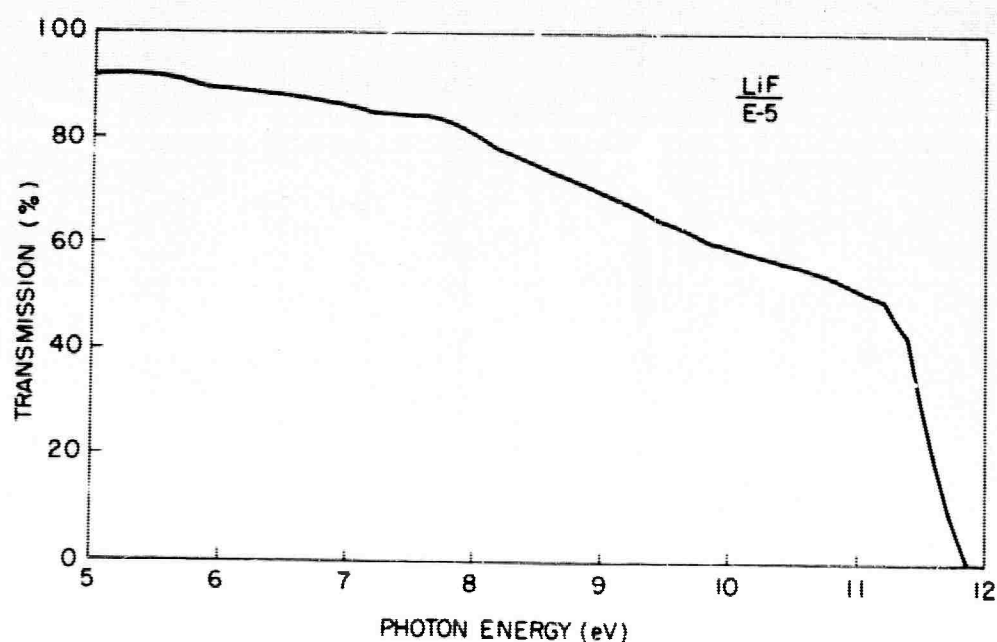


FIG. 20. LIF WINDOW TRANSMISSION CURVE.

energy with the current from a Cs_3Sb photodiode with known absolute yield in the vacuum ultraviolet region.

Errors may be introduced in the yield measurement if precautions are not taken to determine the effects of leakage current, and to eliminate second and higher order lines and scattered light produced by the grating. The magnitude of the leakage current is determined by interrupting the light beam with the flap valve at the monochromator exit slit and by measuring the current. Then the leakage current is subtracted from the measured photoemission current. In the spectral region from 2100 Å to 1700 Å an optical grade quartz filter can be used to eliminate second order lines from the strong hydrogen spectrum occurring between about 900 Å and 1650 Å. If the system is operated without windows, a LiF filter may be used to eliminate second order lines at wavelengths down to 1060 Å resulting from strong lines occurring in the He and Ne spectra at shorter wavelengths. Scattered light from longer wavelengths can be detected during measurements below 1000 Å by inserting quartz, LiF, or other filters. If the threshold in yield occurs in the spectral range above 1600 Å, as is the case with CdS, a quartz filter must be installed to eliminate scattered light from the intense hydrogen spectrum below 1600 Å.

All electrodes inside the collector, except the emitter, are operated at collector potential during the quantum yield measurement on sealed glass photodiodes. It is also necessary that the entire incident light beam strike the photoemitting surface so that the total amount of light incident on the test

samples or the reference tube is the same. The envelope of the high vacuum test chamber is grounded and provides a return path for the photoemitted electrons which escape through the hole in the collector. Yield measurements made with the collector connected to the metal envelope have been compared with measurements made when the collector was operated at a large positive potential and have been found to be in substantial agreement provided that the photocurrent is measured in the emitter arm of the circuit.

The sodium salicylate coating is applied as illustrated in Fig. 21 by spraying a saturated solution of sodium salicylate in alcohol from a modified DeVilbiss #40 glass nebulizer onto an optical filter or directly on the envelope of the photodetector. The nozzle of the nebulizer has been modified by drilling a hole through a rubber stopper and inserting a 1/16-in. ID brass tube as illustrated. The vaporizer is operated with nitrogen (or air) at a pressure of approximately 5 psi. The N_2 or air is humidified by bubbling through a flask of water before it is introduced into the vaporizer. The surface to be coated is held about 4 to 8 in. from the nozzle so that the coating appears to dry on contact. If the coating is to be used for detection in the region from 4 to 6 eV, it must be made thick enough so that an object viewed through the coating cannot be easily distinguished. The method described above is similar to a method described by Smith [Ref. 33].

The absolute quantum yield is established by comparing the test sample with a Cs_3Sb standard with a LiF window. The

Cs_3Sb standard has been calibrated at 3 eV by comparison with an RCA 934 photodiode which has been calibrated for absolute quantum yield by W. E. Spicer, and checked with the aid of H. R. Philipp at General Electric Research Laboratories [Ref. 34]. The absolute yield of the Cs_3Sb standard has been measured to 6 eV by comparison with a bolometer or a thermocouple standard. The relative yield has been measured in the vacuum monochromator using the sodium salicylate standard over the energy range from 4 to 11.6 eV. The two yield curves overlap in the energy range from 4 to 6 eV so that the absolute yield in the vacuum ultraviolet region is established within an estimated error of $\pm 15\%$.

Under ultraviolet radiation for photon energies greater than 4 eV, Watanabi and Inn [Ref. 35] have found that sodium salicylate emits photons at approximately 4300 \AA with constant quantum efficiency. Their measurements cover the continuous range of wavelengths from 3000 \AA (4.1 eV) to 850 \AA (14.6 eV) and include a point at 584 \AA (21.2 eV). The quantum efficiency is reported to be down by 15% at the 584 \AA wavelength. If the layer of sodium salicylate is not sufficiently thick, some of the incident photons in the energy range from 4 to 6 eV will not be absorbed by the sample and there will be a corresponding loss in quantum efficiency [Ref. 36]. This loss of efficiency has been confirmed by recent experiments in this laboratory. The quantum efficiency may change slowly over a period of several days depending on the history of the sodium salicylate coating; however, it will remain constant over a period

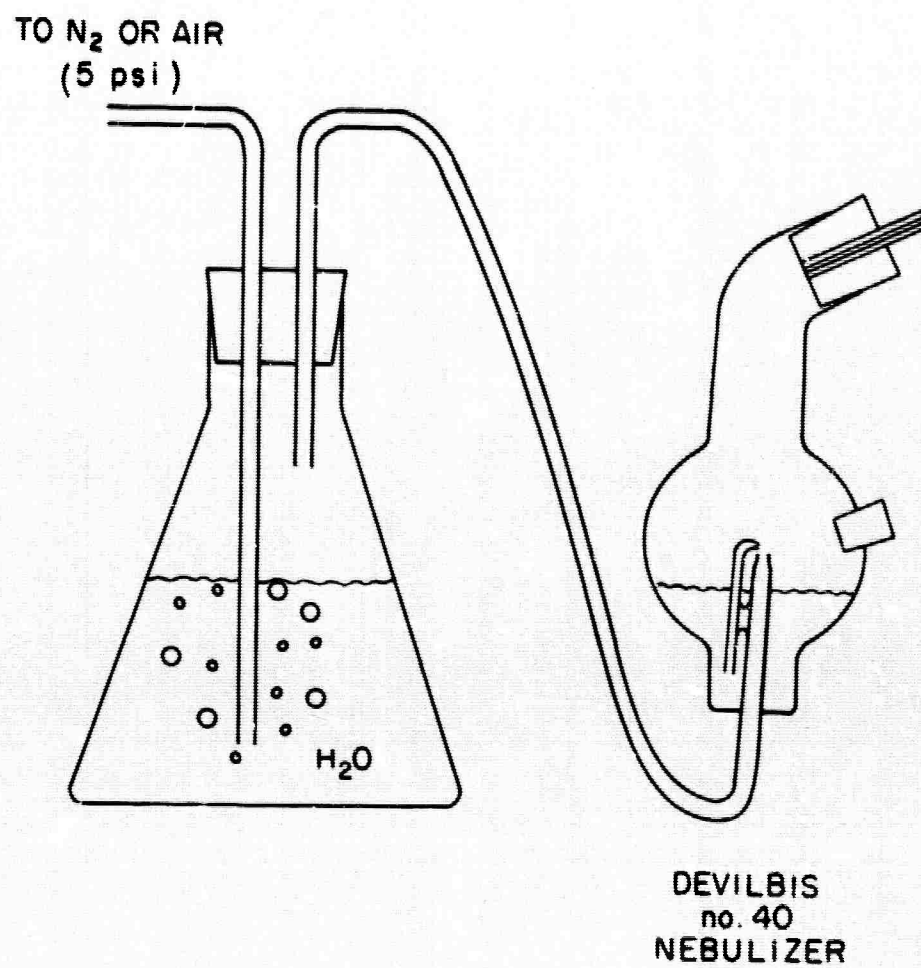


FIG. 21. APPARATUS FOR APPLYING SODIUM SALICYLATE COATINGS.

of several hours which allows ample time for measurement of relative quantum yield. Smith [Ref. 33, p. 5] gives a summary of the previous literature.

3. Measurement of Energy Distributions

The energy distribution of photoemitted electrons is determined by measuring the small signal conductance of the photodiode as a function of dc retarding potential for a fixed incident photon energy. Spicer has developed a measuring technique which has been modified by Berglund [Ref. 37] as shown in Fig. 22. This uses a motor driven dc voltage sweep and an ac drive with a synchronous detector that eliminates the capacitive component of tube current and reduces noise in the measurement. Each energy distribution curve is plotted automatically on an XY recorder. A set of 15 to 25 energy distribution curves can be plotted within an hour after cleaving a CdS sample in the high vacuum. Since the minimum time to form a monolayer of gas on the surface at 10^{-9} torr is approximately fifteen minutes, changes in the energy distributions due to changing surface conditions should be observable.

Previously reported measurements using the ac method have been made on sealed glass tubes in which no dc current could flow to the envelope. The effect of using a grounded metal envelope has been investigated by operating the bridge (Fig. 22) either with the collector grounded or with the node between the load resistors grounded. This has been done to determine if electrons which escape to the metal case, through the hole in the collector used to admit light, would produce

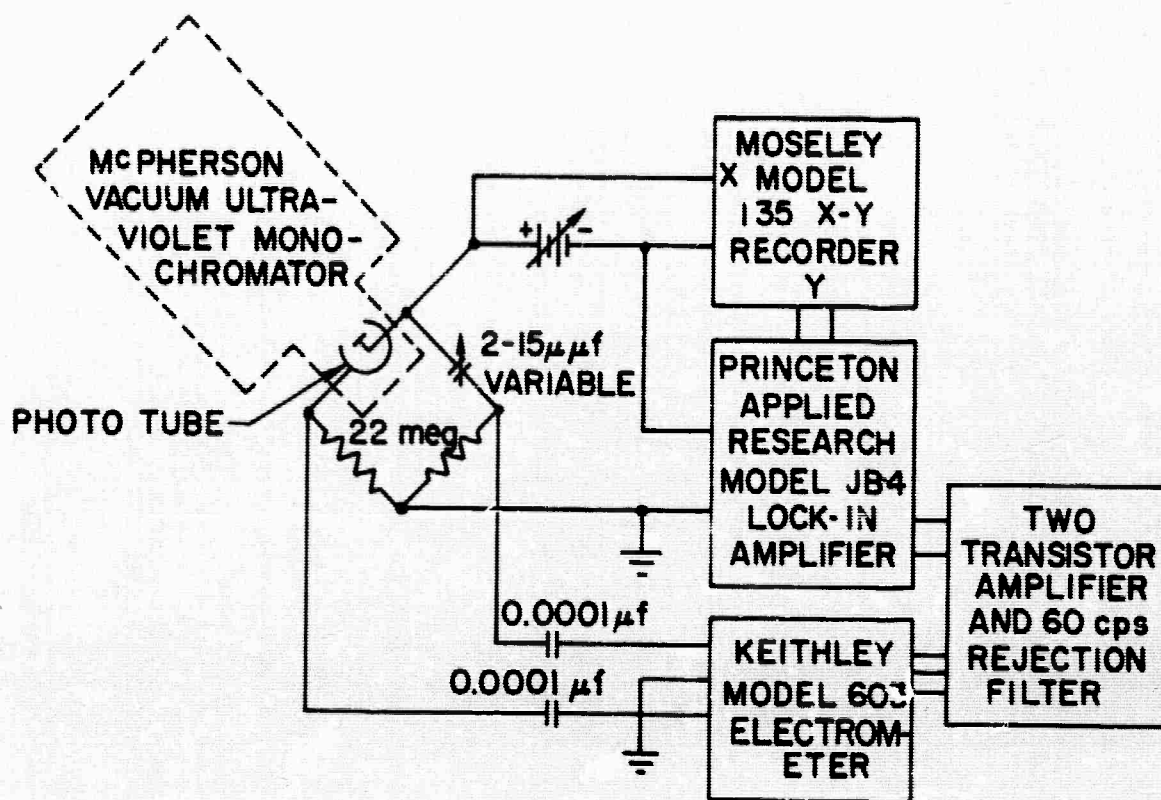


FIG. 22. CIRCUIT FOR MEASURING ELECTRON ENERGY DISTRIBUTIONS IN THE VACUUM ULTRAVIOLET.

different energy distributions for the different field configurations. The field distortion has also been reduced in one experiment by covering the hole in the collector with a mesh of 0.005-in. wire with a spacing of approximately 0.2-in. No difference in the energy distributions measured by the various methods has been observed. Therefore, the measurements have been made by the method in which the load resistors are grounded for stability and low noise. The collector hole is not covered with a mesh in order to maximize the front-to-back ratio.

Magnetic fields in the test chamber can cause the energy distribution curves to be distorted because of the change in electron trajectories. The effect of the earth's magnetic field has been found to be negligible by spacially orienting the energy distribution experiment in different directions. Energy distribution curves measured at the same photon energy were found to be the same regardless of orientation. The ion pump used with the system requires a very strong magnetic field provided by a permanent magnet. This magnet is removed during the measurements since its field is sufficiently large to distort the energy distributions. Residual magnetic fields in the test chamber have a negligible effect on the measured energy distribution. This has been determined by measuring energy distributions before and after a demagnetizing field was applied to the test chamber.

A gaseous atmosphere at a pressure of approximately 10^{-4} torr exists in the analyzer can of the photodiode during windowless photoemission experiments, in which neither the

BLANK PAGE

sample chamber nor the lamp is isolated from the main chamber by a window. This gaseous ambient can affect an energy distribution curve by scattering the photoemitted electrons. Figure 23 shows energy distribution curves taken in an oxygen atmosphere at several pressures. The shape of the curves is approximately constant for pressures below 10^{-3} torr and the amplitude is constant for pressures below 10^{-4} torr. Since the mean free path for electrons in H_2 , He, and Ne is more than twice the mean free path in O_2 [Ref. 38], it is apparent that the energy distributions will not be affected by scattering of the electrons with the gas molecules under the conditions of the experiment.

4. Work Function and Surface Properties of the Collector

In photoemission measurements it is convenient to use a metallic collector. For reasons given below it is important to know the value of the collector work function and to know the magnitude of variations in work function over the surface. A Fowler plot of the threshold of photoemission from the collector is used here to determine its work function. A typical plot for a freshly evaporated aluminum collector surface is shown in Fig. 24.

During a sequence of experiments, the collector surface which is originally prepared by hydrogen firing may be coated with an evaporated layer of aluminum, or it may be exposed to gases such as oxygen, nitrogen, hydrogen, or water vapor. The electron affinity of the semiconductor may change as a result of exposure to the same gases. In addition the energy bands near the surface of the semiconductor may be bent with respect

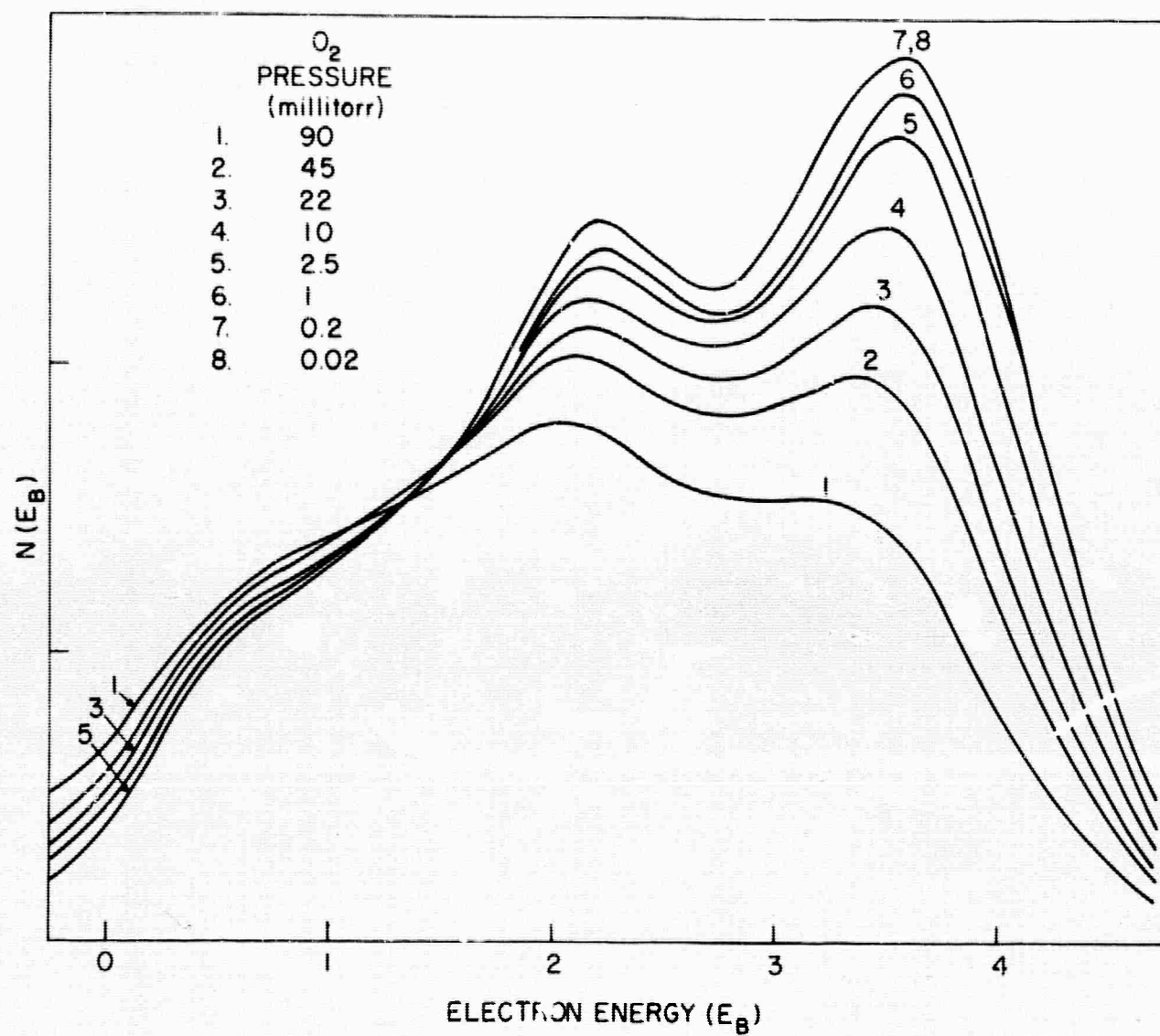


FIG. 23. ENERGY DISTRIBUTIONS FOR DETERMINING SCATTERING OF ELECTRONS AS A FUNCTION OF O_2 PRESSURE.

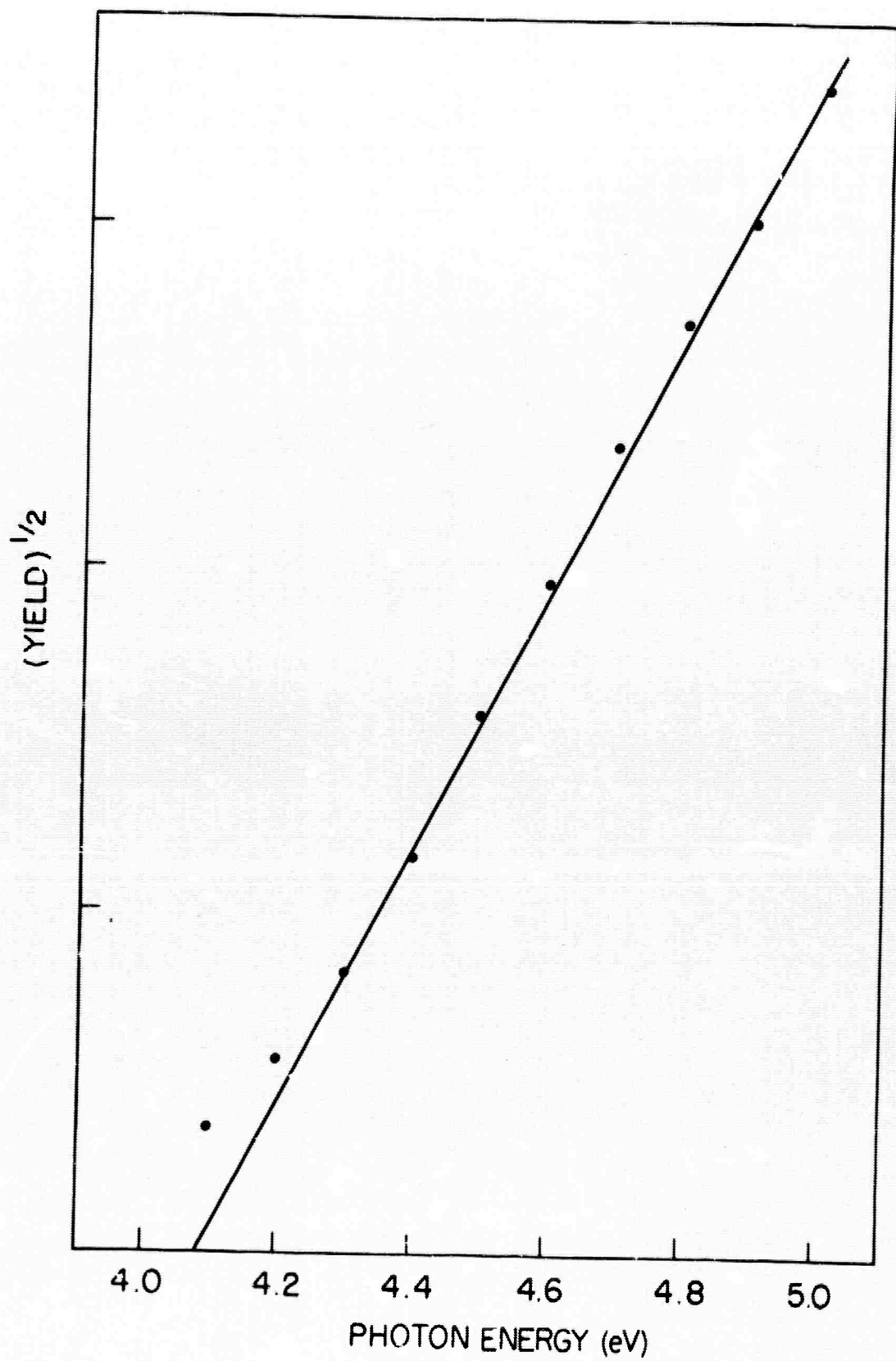


FIG. 24. FOWLER PLOT USED TO DETERMINE THE WORK FUNCTION OF AN ALUMINUM COLLECTOR.

to the bands far from the surface resulting in an apparent change in the electron affinity. A knowledge of the work function of each of the surfaces aids in understanding the effects of band bending, in estimating the impurity level in the semiconductor by locating the Fermi level, and in estimating the effect of intentional or unintentional chemical treatment or contamination on both the semiconductor and metal surfaces.

The energy level versus distance diagram for a semiconductor emitter and a metal collector is shown in Fig. 25. This situation has been discussed in detail by Apker, Taft, and Dickey [Ref. 39]. The diagram corresponding to cutoff of photocurrent is shown in Fig. 25a. The potentials satisfy the relation

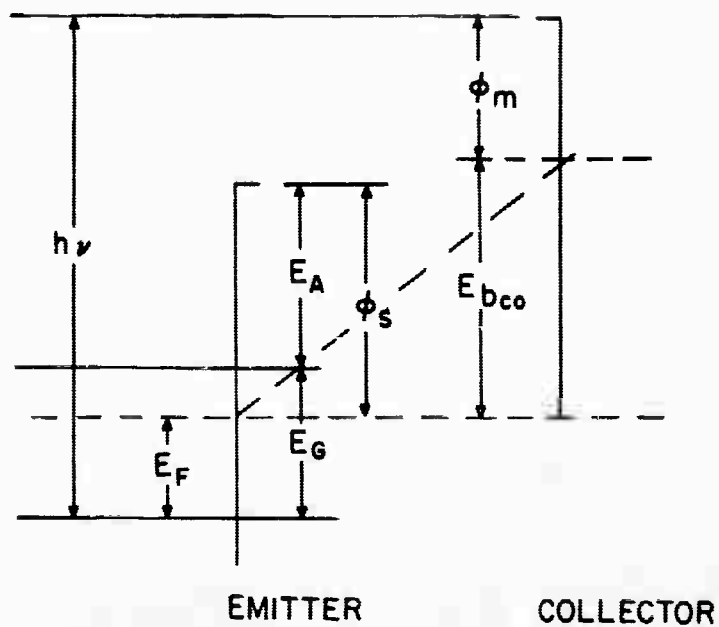
$$E_{b_{co}} + \phi_m = h\nu - E_F \quad (1)$$

in which $E_{b_{co}}$ is the electron energy corresponding to the applied voltage, $h\nu$ is the photon energy, E_F is the Fermi level referred to the top of the valence band, and ϕ_m is the work function of the collector. The semiconductor work function is related to the Fermi level through the expression

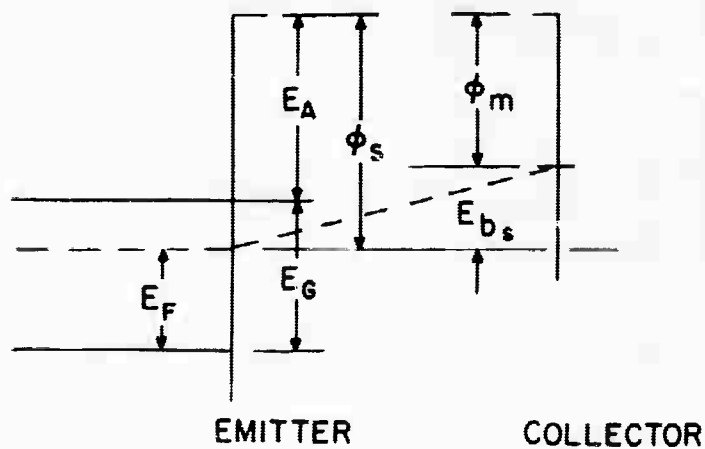
$$E_F + \phi_s = E_A + E_G \quad (2)$$

in which E_A is the electron affinity and E_G is the band gap energy.

The diagram corresponding to saturation of photocurrent is shown in Fig. 25b. The potential satisfy the relation



(a)



(b)

FIG. 25. ENERGY LEVEL DIAGRAM FOR CUTOFF (a) AND SATURATION (b) OF PHOTOEMISSION CURRENT.

$$\phi_m + E_{bs} = \phi_s \quad (3)$$

in which E_{bs} corresponds to the applied voltage at which saturation occurs.

A nonuniform collector work function will cause a loss of resolution in the energy distribution experiment since an electron which has just enough energy to be collected in one region of the collector may have insufficient energy to be collected in another region. The effect has been estimated by measuring energy distribution curves at the same photon energy for similar freshly cleaved CdS emitters while using one of four different types of collectors. Comparisons have been made between a collector which was cleaned by degreasing and hydrogen firing prior to assembly, a collector which was coated with a fresh layer of aluminum evaporated in high vacuum, and two similarly aluminized collectors which were subsequently exposed to oxygen or nitrogen. The shape of the measured energy distributions agreed in detail, but the zero of energy shifted with the work function of the collector. This led to the conclusion that variations of collector work function have negligible effect on the resolution of the experiments reported here.

III. THEORY OF PHOTOEMISSION FROM SEMICONDUCTORS

A. INTRODUCTION

Photoemission has been used previously by many investigators to study band structure, optical transitions, escape of electron from solids, and pair production (or electron-electron

scattering) in both semiconductors and metals. Measurements of quantum yield have been used [Refs. 1, 2, and 3] to determine the type of optical transitions which occur near the threshold for photoemission. Both quantum yield and the energy distribution of photoemitted electrons have been used [Ref. 40] to determine the absolute energy level of high density initial and final states and to estimate the selection rules coupling these states. Pair production [Refs. 25 and 26] has been studied using the same techniques. Distortion of the measurements due to band bending [Refs. 41-47] and scattering [Refs. 25, 27, and 48] has also been considered. Theoretical calculations of photoemission have been based on the Bloch model of the electron. The wave function of an electron in the periodic crystalline potential of a solid in the Bloch model is of the form

$$\psi(\vec{k}, \vec{r}) = u_{\vec{k}}(\vec{r}) e^{i\vec{k} \cdot \vec{r}} \quad (4)$$

in which $u_{\vec{k}}(\vec{r})$ is a periodic function of distance with the same period as the crystal lattice. The product of the propagation vector \vec{k} and the reduced Plank's constant \hbar is called the crystal momentum. The probability of transition between a pair of Bloch states depends on the magnitude of the matrix element of the Hamiltonian which couples the two states, i.e., on selection rules which are contained in the matrix element. The transition probabilities between a group of initial and final states depend, in addition, on the density of initial and final states in \vec{k} space.

If the potential which the electron sees is not completely periodic, a summation of Bloch states must be used to represent each electron. This nonperiodicity may occur as a result of strong electron-lattice coupling [Ref. 24]. In this situation the assumptions on which the one electron approximation is based may break down. In cases where the quantum state cannot be represented by the simple Bloch states of Eq. (4), selection rules determined using that representation may not be meaningful even though certain features of the Bloch representation remain approximately correct.

Consideration of the Bloch model leads to two familiar types of optical transitions, the direct and the indirect transitions. A third type of transition, the nondirect transition [Ref. 49], is defined in this section to include situations in which the Bloch model is inadequate. In the direct transition both energy and crystal momentum \bar{k} are directly conserved and the transition probability depends on the joint density of states [Ref. 50]. In the indirect transition both energy and crystal momentum are conserved with the aid of phonons. The transition probability depends on the product of the initial and final density of states. The energy gained or lost by the phonon is small. If the Bloch representation is inadequate so that conservation of crystal momentum is no longer an important selection rule, the transition probability will, again, depend on the product of the initial and final densities of states [Ref. 49]. Nondirect transitions include indirect transitions and transitions in

which conservation of \bar{k} is not important as a selection rule.

A large amount of information about the density of states can be obtained from photoemission measurements by assuming that the matrix elements at a given photon energy are constant [Ref. 50] so that the transition probabilities depend only on the initial and final densities of states in energy space. The density of states determined from the results of photoemission measurements can be used to calculate photoemissive yield and optical constants. It can also be used to reproduce the energy distribution curves from which it is obtained.

Distortion in energy distribution curves due to band bending has not been considered previously in a quantitative fashion. A method for calculating the effects of band bending on energy distribution curves is developed here. Effects of elastic and inelastic scattering of the excited electrons are also considered.

B. THE PHOTOEMISSION EQUATIONS

The photoemission equations are derived by assuming that all of the nonreflected photons from a normally incident light beam are absorbed by optical excitation of electron-hole pairs in the solid. Some of the optically excited electrons travel to the surface with or without loss of energy. Those electrons which arrive at the surface with sufficient energy, and which are not reflected back into the solid, escape into the vacuum and contribute to the photoemission current. The remaining electrons are unable to escape and lose energy inside the solid. The ratio of emitted electron flux to incident photon

flux is the quantum yield. The emitted electron flux per unit energy range is the energy distribution of photoemitted electrons.

Consider a photon flux F traveling to the left at a distance x from the surface of a semi-infinite solid as shown in Fig. 26. The differential loss of photon flux dF in a distance dx is proportional to the product of the photon flux and the thickness of the absorbing region. The constant of proportionality is the absorption coefficient. This may be expressed in terms of the differential equation

$$\frac{dF}{F} = -\alpha(h\nu)dx \quad (5)$$

The solution of Eq. (5) for photon flux as a function of distance is

$$F(x, h\nu) = F_t(h\nu)e^{-\alpha x} \quad (6)$$

in which $F_t(h\nu)$ is the value of the photon flux (nonreflected) just inside the surface of the sample. Substitution of Eq. (6) in Eq. (5) results in the expression

$$dF(x) = -\alpha F_t(h\nu)e^{-\alpha x}dx \quad (7)$$

The optical absorption of the photons results from excitation of valence band electrons to final energy levels in the conduction band in the range of energies between the conduction band minimum and an energy level which exceeds the valence band maximum by the photon energy. The probability

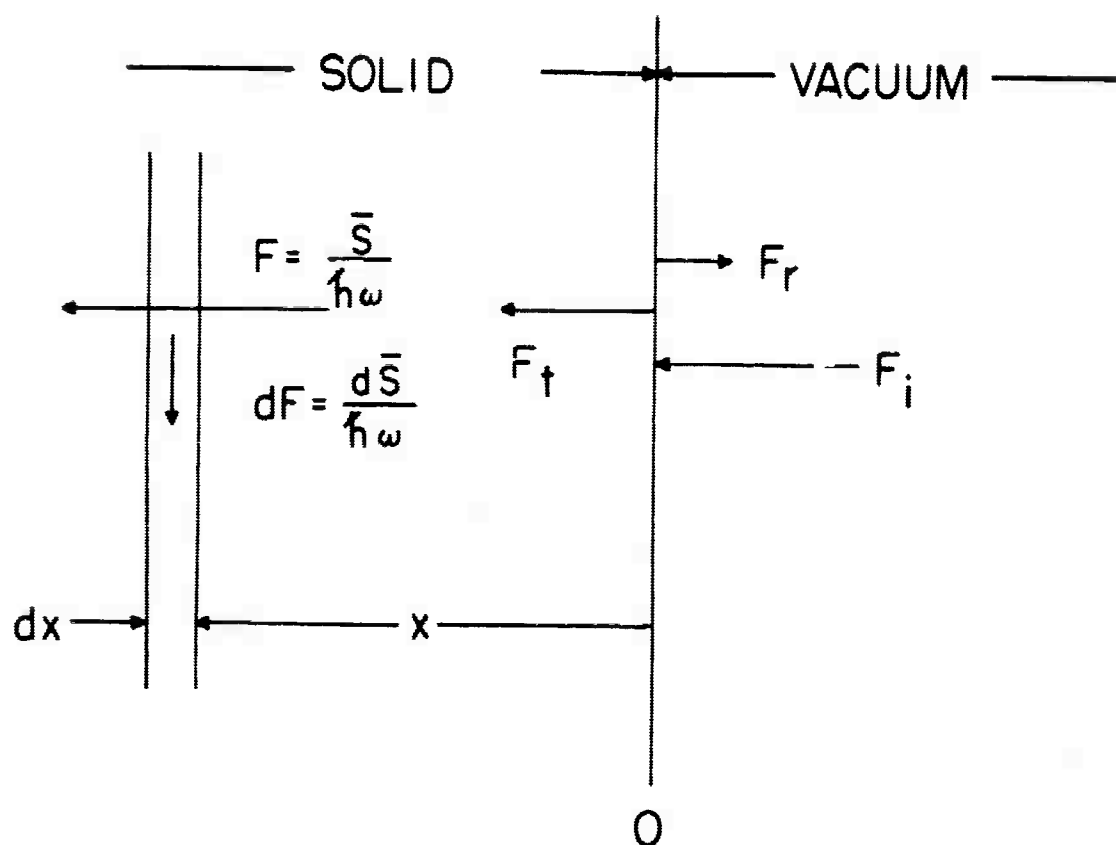


FIG. 26. SPATIAL DIAGRAM SHOWING PHOTON AND POWER ABSORPTION IN A SOLID.

that the optical excitation will occur to a final energy level between E and $E+dE$ as illustrated in Fig. 27 may be expressed in terms of a probability density function, $p_o(E, hv)$. This function may be normalized by dividing by its integral over all final states given by

$$P_o(hv) = \int_{E_G}^{hv} p_o(E, hv) dE \quad (8)$$

That portion df of the differential photon flux dF which is absorbed in an energy range between E and $E+dE$ can be expressed using Eqs. (7) and (8) by the relation

$$df(E, hv, x) dE = -\alpha(hv) \frac{p_o(E, hv)}{P_o(hv)} F_t(hv) e^{-\alpha x} dE dx \quad (9)$$

In Eq. (9) the probability density function for absorption $p_o(E, hv)/P_o(hv)$ may be combined with the absorption coefficient $\alpha(hv)$ to give the absorption per unit of final energy range $\alpha'(E, hv)$ in the solid.

The probability that an electron will travel to the surface and escape after being excited to an energy E at a distance x from the surface can be expressed in terms of an energy dependent attenuation length $L(E)$ and a threshold function $T(E)$ [Ref. 32] which are interdependent. The details of the relationship between $T(E)$ and $L(E)$ in the presence of phonon scattering and specular or diffuse reflection of electrons at the surface is not well understood (see Secs. C2 and C3 for more discussion of these quantities). In this discussion, it

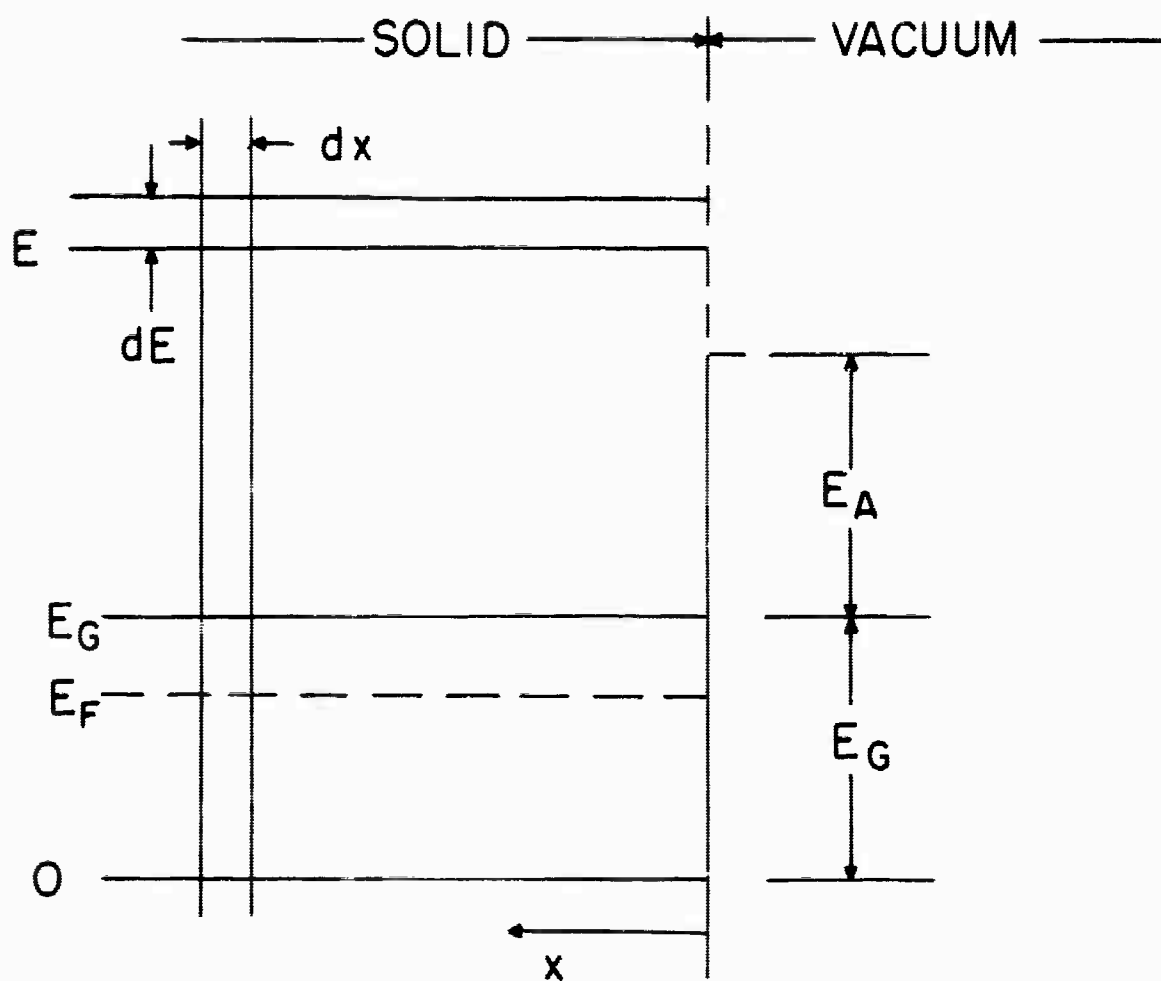


FIG. 27. ENERGY VERSUS DISTANCE DIAGRAM FOR OPTICAL ABSORPTION IN A SOLID.

will be assumed that $L(E)$ is independent of $T(E)$ and represents an attenuation length in the solid with no surface present. Thus, the probability that an electron escapes to the surface is given by

$$p_1 = e^{-x/L(E)} \quad (10)$$

The product of Eqs. (9) and (10) gives the probable number of electrons dn in energy range between E and $E+dE$ which are excited at a distance x from the surface and subsequently travel to the surface without loss of energy. The result is

$$dn(E, hv, x)dE = -\alpha'(E, hv)F_t(hv)e^{-\alpha x}e^{-x/L(E)}dE dx \quad (11)$$

Integration of Eq. (11) over x from 0 to ∞ gives the number of electrons n per unit energy range which are excited and which arrive at the surface. The electrons which disappear due to attenuation are assumed to be lost from the energy distribution. The resulting expression is:

$$n(E, hv) = F_t(hv) \frac{\alpha'(E, hv)}{\alpha(hv)} \frac{1}{1 + \frac{1}{\alpha(hv)L(E)}} dE \quad (12)$$

in which $p_0(E, hv)/P_0(hv) = \alpha'(E, hv)/\alpha(hv)$.

Equation (12) is now multiplied by the energy dependent threshold function $T(E)$ which takes into account the directional dependence of the escape probability for electrons arriving at the surface. As mentioned previously, and as discussed in detail in Secs. C2 and C3, the threshold function and the

attenuation length are not actually independent. The result is the expression for the energy distribution of photoemitted electrons $N(E)$ given by

$$N(E)dE = F_t(h\nu)T(E) \frac{\alpha'}{\alpha} \frac{1}{1 + \frac{1}{\alpha(h\nu)L(E)}} dE \quad (13)$$

The quantum yield is determined by integrating Eq. (13) over all energies from the threshold to the photon energy (referred to the top of the valence band) and dividing by the incident photon flux F_1 resulting in the expression

$$Y(h\nu) = \frac{\int_{E_G+E_A}^{h\nu} N(E)dE}{F_1(h\nu)}$$

$$= \frac{F_t}{F_1} \int_{E_G+E_A}^{h\nu} T(E) \frac{\alpha'}{\alpha} \frac{1}{1 + \frac{1}{\alpha(h\nu)L(E)}} dE \quad (14)$$

in which $F_t/F_1 = 1-R$ accounts for the fact that a fraction of the photons are reflected. R is the reflection coefficient.

The equations derived in this section for yield and the energy distribution of photoemitted electrons are used to derive methods of determining the density of states (Sec. D) and to determine the effects of band bending and scattering on photoemission measurements (Sec. E). The results will be used in the next chapter to aid in the interpretation of photoemission data and to make calculations based on the derived density of states.

C. ABSORPTION COEFFICIENT, ATTENUATION LENGTH, AND THRESHOLD FUNCTION

1. Absorption Coefficient and Optical Conductivity

The absorption coefficient and optical conductivity of a material are proportional at a fixed photon energy, as is shown below. The Poynting vector \bar{S} and the photon flux \bar{F} are related by the expressions

$$\left. \begin{aligned} \bar{S} &= h\nu \cdot \bar{F} \\ d\bar{S} &= h\nu \cdot d\bar{F} \end{aligned} \right\} \quad (15)$$

so that Eq. (5) may be rewritten as

$$\frac{d\bar{S}}{\bar{S}} = -\alpha dx \quad (16)$$

The average power absorbed in a slab of unit area and thickness dx is by definition

$$d\bar{S} = -\frac{1}{2} \sigma \mathcal{E}^2 dx \quad (17)$$

in which σ is the optical conductivity and \mathcal{E} is the peak value of the sinusoidal electric field. The power incident on the slab is given by the time average value of the Poynting vector as

$$\bar{S} = \frac{1}{2} \frac{\eta}{z_0} \mathcal{E}^2 \quad (18)$$

in which z_0 is the impedance of free space and η is the real part of the index of refraction. To derive Eq. (18) the electric and magnetic fields are assumed to be represented by their magnitudes multiplied by the appropriate unit polarization

vectors and by a propagation term given by $e^{i\omega(t-Nz/c)}$ with $N = \eta - ik$ as the complex index of refraction. Substitution of Eqs. (17) and (18) into Eq. (16) results in a relationship between α and σ given by

$$\alpha = \sigma \frac{z_0}{\eta} \quad (19)$$

The optical conductivity is determined quantum mechanically by calculating the transition probability per unit time per unit volume between an initial and a final state and then by summing over all combinations of states for which transitions are allowed [Ref. 50]. The summation may be done over states in \bar{k} space (if Bloch waves are used) or in energy space by the appropriate transformation from \bar{k} space. For direct transitions, the transition probability depends on the combined density of states [Ref. 50] in energy space and on a matrix element. (See transition d in Fig. 28.) For indirect transitions such as phonon-assisted transitions, the transition probability depends on the product of the initial and final density of states, and on matrix elements connecting the initial and final states through a virtual state. (See transition i in Fig. 28.) Other mechanisms such as polarization of the lattice [Ref. 51], low hole mobility [Ref. 20, 21, and 22], or nonperiodic crystal structure may exist for which the Bloch representation of the electron is not the best representation. Then it is necessary to take a summation of Bloch states to represent the electron, and the coupling between electronic states can no longer depend on conservation of a single value of \bar{k} vector. Under these

circumstances, nondirect transitions may occur so that the transition probability will depend on the product of the initial and final densities of states in energy space and on matrix elements. (See transition n in Fig. 28.) The matrix element includes the selection rules and other terms which determine the magnitude of the transition.

If the transition probabilities for a given photon energy are of the same order of magnitude, then Eq. (19) may be written as

$$\alpha'(E, hv) = \sigma'(E, hv) \frac{z_0}{\eta} = \frac{K}{\eta} \frac{N_c(E) N_v(E-hv)}{hv} \quad (20)$$

in which α' and σ' represent the contribution to the absorption coefficient and to the optical conductivity from electrons absorbed in a given final energy range, and K contains all of the physical constants. Equation (20) is used to calculate optical conductivity for comparison with experimental values. This serves as a check on the importance of nondirect transitions.

2. Attenuation Length for Excited Electrons

An optically excited electron either moves through the solid at a constant energy level until it escapes, or it changes energy. The energy changes can be grouped into two important categories: those processes in which the amount of energy change is small in comparison with the resolution of the experiment such as phonon or impurity scattering, and those processes in which the amount of energy lost is significantly larger than the resolution of the experiment such as pair production. In

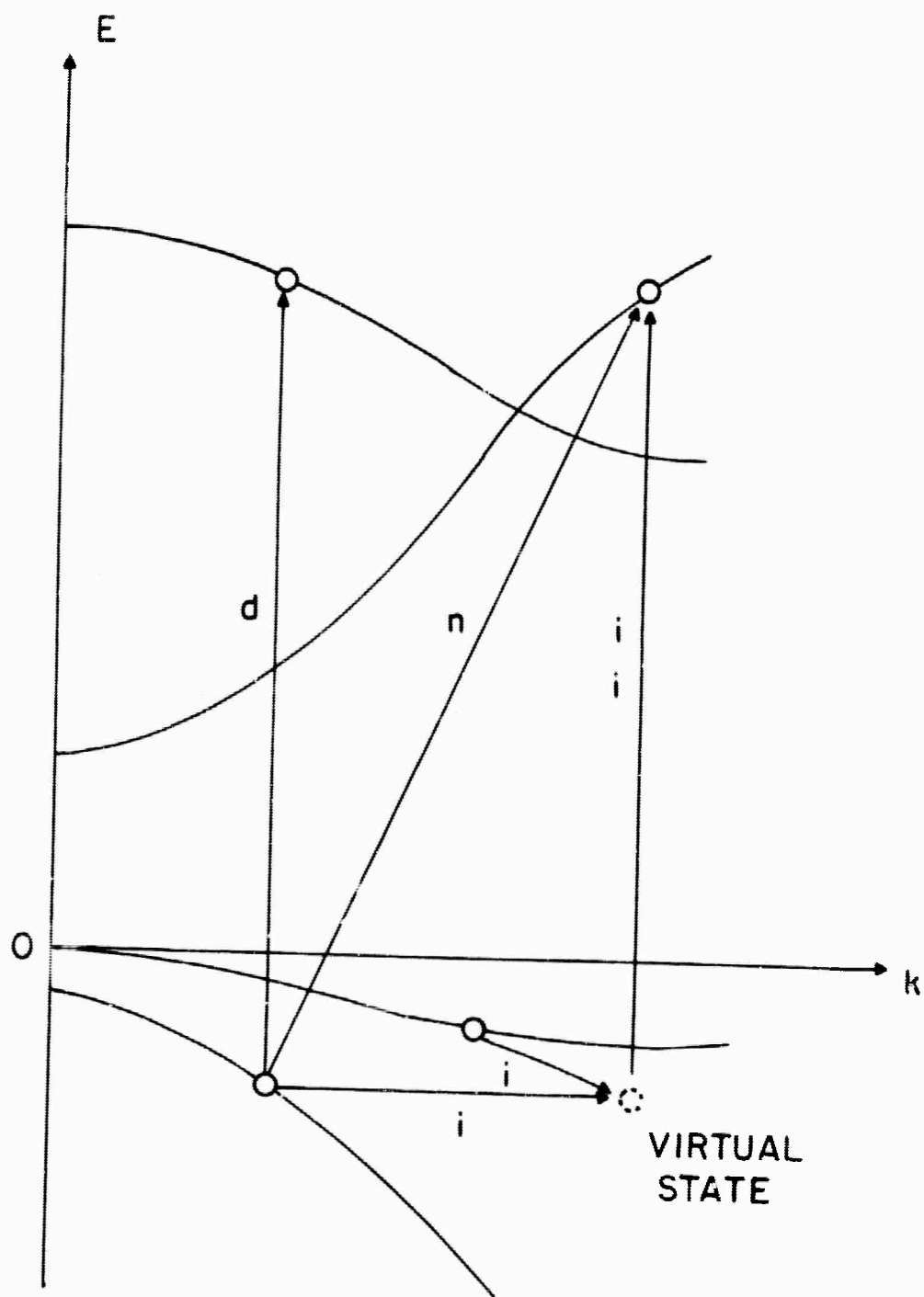


FIG. 28. E VERSUS k DIAGRAM FOR ABSORPTION BY DIRECT (d) INDIRECT (i) AND NONDIRECT (n) TRANSITIONS.

pair production, part of the energy of an excited conduction band electron is given up by exciting a valence band electron to the conduction band, with energy being conserved.

The average distance traveled by an electron before suffering a low loss collision is represented here by a phonon collision mean free path ℓ_p . The average distance travelled by an electron before suffering a high energy loss collision is represented here by an electron mean free path ℓ_e . The attenuation length $L(E)$ represents the average net distance traveled (in the x direction) perpendicular to an infinite plane source of infinitesimal thickness before electrons originating isotropically from the source suffer a high loss collision. The way in which $L(E)$ depends on both ℓ_p and ℓ_e is complicated, and has been studied by a number of people.

If no surface is present in the region of interest, age theory (the theory of diffusion with loss) [Ref. 52] may be used to determine $L(E)$. If a surface exists in the region of interest, as in photoemission, age theory does not apply exactly since the total integrated distance traveled by an electron in the x direction may be much longer than its attenuation length. Electrons arriving at a surface may escape, or they may undergo specular or diffuse reflection. Age theory yields a relation between the parameters given by

$$L(E) = \frac{\ell_e}{\sqrt{3}} \sqrt{\frac{1}{1 + \ell_e/\ell_p}} \quad (21)$$

According to this theory, $L(E)$ is proportional to ℓ_e for

$l_e \ll l_p$, and to $\sqrt{l_e l_p}$ for $l_e \gg l_p$.

Stuart, Wooten, and Spicer [Ref. 53] have done an extensive investigation of the interrelation of mean free paths and attenuation lengths by the Monte Carlo method for thin film photoemitters illuminated on the surface opposite the escape surface. They considered specular and diffuse reflection separately. Figure 29 shows a typical set of results from their calculations. Their results indicate that age theory predicts too small an attenuation length for small values of l_e and too large a value for large value of l_e .

The electron-electron scattering mean free path in metals has been related to the density of states in a simple way by Berglund [Ref. 32]. The mean free path for scattering due to pair production in a semiconductor can be treated in the same way if nondirect transitions are highly probable in the scattering process. The relation between the attenuation length and the absorption length is important in determining the absolute yield from CdS. In addition, the energy dependence of the attenuation length may cause significant structure to appear in energy distribution curves of semiconductors as shown in Chapters IV and V.

3. The Threshold Function

Optically excited electrons which arrive at the surface with an energy exceeding the vacuum level $[(E_G + E_A)$ in Fig. 27] can escape if they are not reflected back into the solid at the interface. Reflection may be either specular or diffuse. The probability that the electron will escape depends on its

direction of travel when it arrives at the surface. Energy and momentum must be conserved in the process. These factors can be combined into a threshold function $T(E)$ which represents an average probability that electrons arriving at the surface with energy E will escape. The attenuation length and the threshold function are interdependent but will be separated in this work.

The Sommerfeld model yields a threshold function of the form

$$T(E) \propto \sqrt{1 - \frac{p_c}{p(E)}} \quad (22)$$

in which $p(E)$ represents the electron momentum normal to the surface with a critical minimum value, $p_c(E_A + E_G)$. The form of threshold function for a semiconductor is probably much more complicated since more details of the band structure and crystal momentum must be included. For example, Herring [Ref. 54] has shown that reflections will be comparatively large for energy levels lying near a Brillouin zone edge. In spite of these difficulties, the above threshold function, or a step threshold function will be used in Chapter IV to give some insight into its effect on the photoemission process.

D. THE DENSITY OF STATES FROM ENERGY DISTRIBUTION CURVES

Energy distribution curves have been used [Ref. 40] to determine important features of the density of states for filled and empty energy levels in metals and semiconductors by observing the change in position of peaks as the photon energy

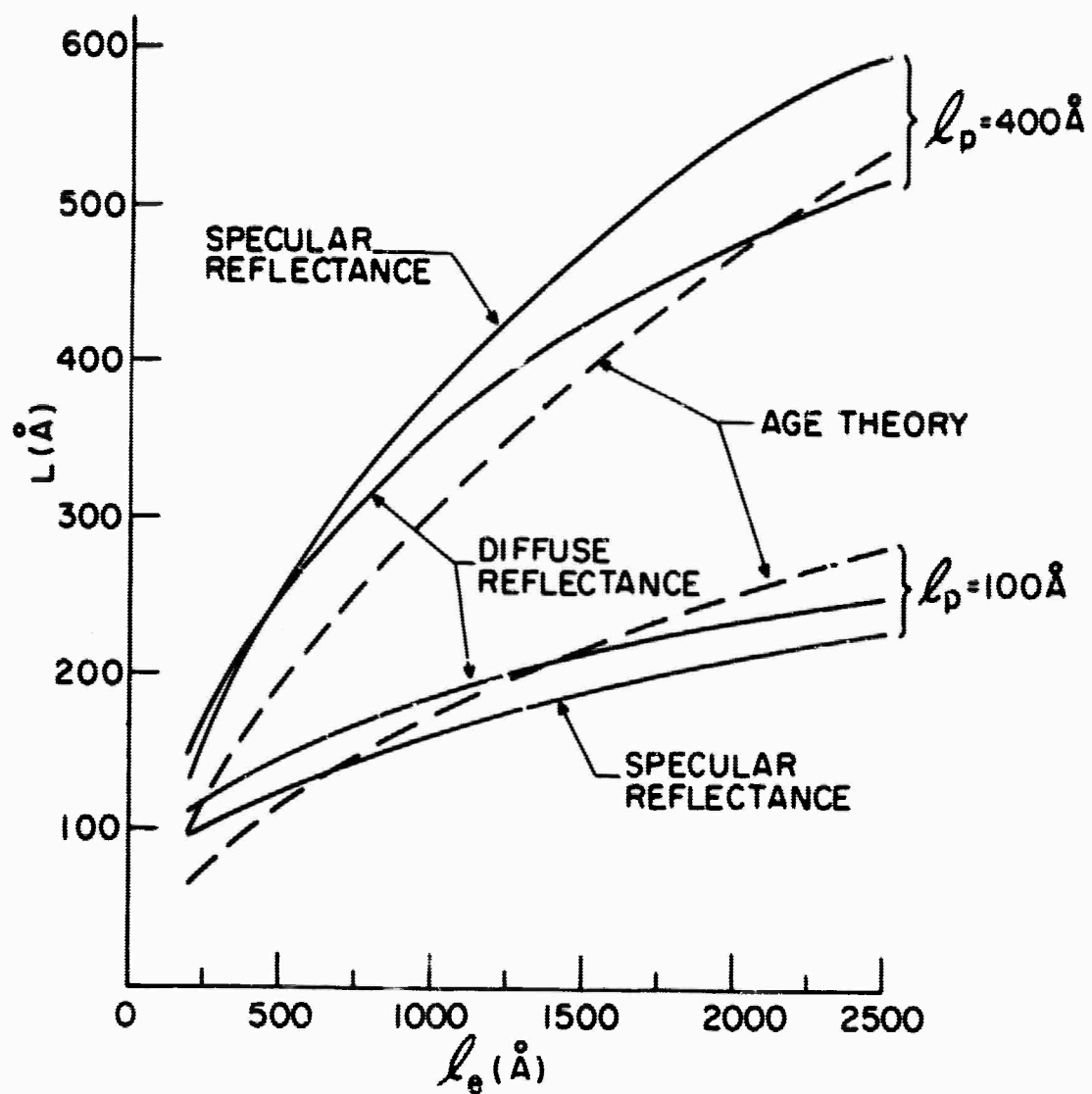


FIG. 29. COMPARISON OF CORRECTED MONTE CARLO CALCULATIONS WITH AGE THEORY.

is varied. These methods have been used primarily to determine the energy levels of peaks and to determine the shape of peaks if either the conduction band or valence band density of states is flat over a large range of energies. If neither density of states is flat over the region of energies which can be observed in photoemission, the shape of the density of states can still be determined by a method described in this section.

The location of peaks in the densities of states can be determined as follows. Peaks which appear in the energy distributions at a constant final energy satisfying the relation

$$E = \text{const.} \quad (23)$$

independent of the photon energy can be associated with large densities of states in the conduction band. Peaks which satisfy the relation

$$E = h\nu - \text{const.} \quad (24)$$

as the photon energy is changed can be associated with large densities of states in the valence band. When the above relations are satisfied over a wide photon energy range, they provide evidence of predominantly nondirect transitions, as illustrated in Fig. 30. Peaks in the energy distributions which appear and disappear or which do not satisfy either Eq. (23) or Eq. (24) over a wide range of photon energies can often be associated with direct transitions. However, the same types of behavior can occur in semiconductors as a result

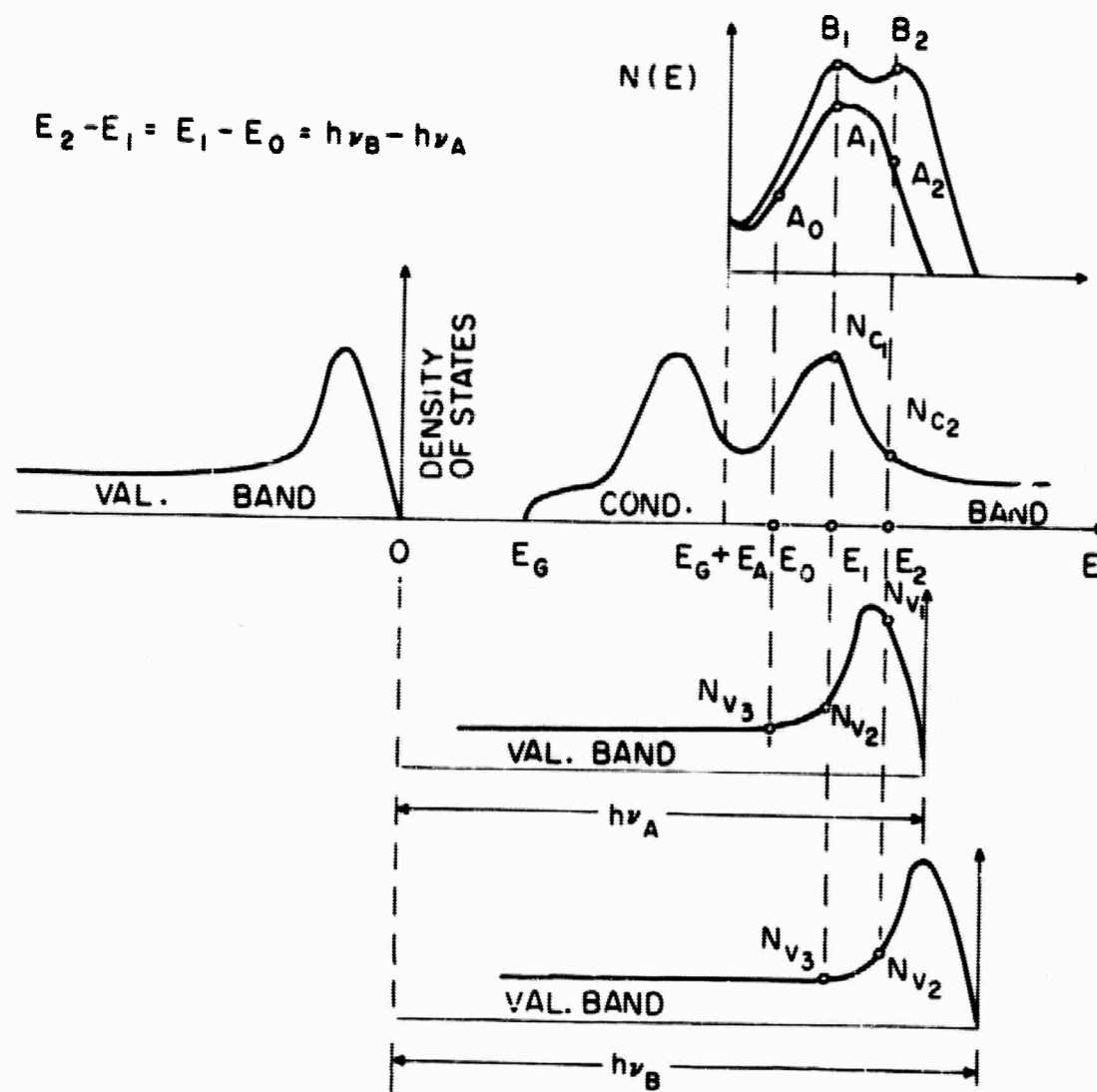


FIG. 30. DIAGRAM ILLUSTRATING CALCULATION OF THE DENSITIES OF STATES FROM ENERGY DISTRIBUTIONS.

of band bending or scattering.

If nondirect transitions predominate, details of the effective density of states may be determined. If Eq. (20) is substituted into Eq. (13), the resulting expression for the energy distribution of emitted electrons is

$$N(E) = K_1 T(E) N_c(E) N_v(E-h\nu) \quad (25)$$

K_1 is an unknown constant which includes physical constants, matrix elements that are assumed to be constant, and gain settings of the amplifier used to record the energy distributions. It is assumed that the term $[1 + 1/\alpha(h\nu)L(E)]^{-1}$ is approximately constant over the range of electron energies involved in the measurement. Equation (25) shows that in a mathematical sense the energy distributions represent the individual members of a family of convolutions of the valence band density of states with the conduction band density of states. The effect of monochromatic photon illumination is represented mathematically by shifting the valence band density of states with respect to the conduction band density of states by an amount equal to the photon energy as shown in Fig. 30.

Under the assumption above, if optical excitation occurs from a region of the valence band density of states which is constant over a large energy range to a conduction band energy range with significant structure, then, in the corresponding range of the energy distribution, Eq. (25) reduces to

$$N(E) = K_2 T(E) N_c(E) \quad (26)$$

Equation (26) indicates that the shape of the energy distribution is determined by the product of the threshold function and the conduction band density of states. Similarly, if optical excitation occurs from a valence band energy range with significant structure to a region of the conduction band density of states which is constant and which is far enough from the threshold that the threshold function is also constant, then Eq. (25) reduces to

$$N(E) = K_3 N_v (E - h\nu) \quad (27)$$

Equation (27) indicates that the shape of the energy distribution is determined by the valence band density of states.

If neither density of states is constant over a large energy range, the density of states can still be determined from the energy distributions. The area under an energy distribution curve is proportional to the yield if the absorption coefficient α is constant as is shown by Eq. (14); therefore, the measured energy distribution curves can be normalized approximately by using the measured yield curve. If the energy distribution curves in Fig. 30 are normalized, their amplitudes A_1 and B_1 at a final energy E_1 are given by

$$\left. \begin{aligned} A_1 &= K_1 T_1 N_{c1} N_{v2} \\ \text{and} \\ B_1 &= K_1 T_1 N_{c1} N_{v3} \end{aligned} \right\} \quad (28)$$

so that two points in the valence band density of states are determined by the ratio $B_1/A_1 = N_{v3}/N_{v2}$. By proceeding in

this fashion the shape of the entire valence band can be determined. The amplitude B_2 at energy $E_2 = E_1 + h\nu_B - h\nu_A$ is written as

$$B_2 = K_1 T_2 N_{c2} N_{v2} \quad (29)$$

so that two points in the conduction band density of states are determined by the ratio $B_2/A_1 = T_2 N_{c2} / T_1 N_{c1}$; therefore, the shape of the entire conduction band density of states can also be determined.

If $L(E)$ is a significant function of electron energy, the term $[1 + 1/\alpha(h\nu)L(E)]^{-1}$ in Eq. (20) is no longer constant over the entire range of electron energies. The normalization procedure is valid, but the product relation applies only over that portion of the range of final energies in which electrons are neither lost due to scattering nor gained due to either secondary electrons or inelastically scattered primary electrons. In this case, or if α is a significant function of photon energy, the multiplying constant K_1 can no longer be determined. The amplitudes of the two energy distribution curves in Fig. 30 at energies E_0 , E_1 , and E_2 which are separated by an energy $h\nu_B - h\nu_A$ can be written as

$$\left. \begin{aligned} A_0 &= K_A T_0 N_{c0} N_{v3} \\ A_1 &= K_A T_1 N_{c1} N_{v2} \\ A_2 &= K_A T_2 N_{c2} N_{v1} \\ B_1 &= K_B T_1 N_{c1} N_{v3} \\ B_2 &= K_B T_2 N_{c2} N_{v2} \end{aligned} \right\} \quad (30)$$

in which K_A and K_B are unknown multipliers. The entire valence band density of states can be found within an unknown constant multiplier using one pair of energy distribution curves. The ratios B_2/A_2 and B_1/A_1 are now given by

$$B_2/A_2 = (K_B/K_A)(N_{v_2}/N_{v_1}) \quad (31a)$$

$$B_1/A_1 = (K_B/K_A)(N_{v_3}/N_{v_2}) \quad (31b)$$

so that N_{v_3} can be found in terms of N_{v_1} and the unknown ratio K_B/K_A which is the same for all pairs of points, by multiplying Eqs. (31a) by (31b). Division of Eqs. (31a) by (31b) determines the shape of features in the valence band density of states in terms of a geometric mean ratio given by

$$N_{v_1} N_{v_3} = \frac{B_1 A_2}{A_1 B_2} N_{v_2}^2 \quad (32)$$

This ratio should be the same regardless of the pair of energy distribution curves from which it is obtained and can be used to check the consistency of the assumed product relation. A similar procedure is used for the conduction band density of states, except that it is not possible to separate the threshold function T from the density of states function N_c .

The methods described in this section will be used in Chapter IV with the experimental results to determine details of the CdS density of states.

E. THE EFFECT OF BAND BENDING ON PHOTOEMISSION

1. Survey

Band bending in semiconductors occurs as a result of the requirement for overall charge neutrality in the material in the presence of charged surface states. For bent bands, the energy with respect to the Fermi level of a given initial or final quantum mechanical state depends on the distance from the semiconductor surface at which the absorption takes place. Optical properties which depend only on the separation between quantum mechanical states such as optical absorption, optical conductivity and reflection are not changed as a result of band bending. However, some characteristics of photoemission depend both on the separation between energy levels and on the electron energy referred to the Fermi level. Yield near the threshold and energy distribution curves over the whole range of energies are modified if band bending is present.

Band bending in semiconductors can affect the results of photoemission measurements in several different ways. Spicer [Refs. 41 and 42] has considered photoemission from defect levels and the effect of band bending on quantum yield. He also considered the impurity concentrations which would be required to produce observable effects from band bending. Van Laar and Scheer [Refs. 43, 44, and 45], Gobeli and Allen [Ref. 46] and Redfield [Ref. 47] have discussed the effect of band bending on the apparent threshold of photoemission. Band bending is only one of many possible effects which can modify the shape of the yield curve near the threshold. This also depends on

the type of transitions (direct or indirect, allowed or unallowed) occurring near the threshold, the presence of defect levels from which photoelectrons may be excited, patchy surfaces, and on the extent to which phonon or impurity scattering modifies the escape conditions.

Measurement of the energy distribution of photoemitted electrons from semiconductors has been used by Spicer [Ref. 40] and others to obtain information about band structure, optical transitions, and scattering processes. Each point on an energy distribution curve represents a single final energy in the vacuum, which corresponds to a single optical transition in the absence of band bending and scattering. Most of the information in an energy distribution curve appears in an energy range far from the threshold. An understanding of the effect of band bending on energy distribution curves is necessary to aid in correct interpretation of the energy distribution curves obtained from semiconductors. Conversely, once these effects are well understood, energy distribution curves may be used to investigate band bending.

Before band bending is considered in detail, it should also be mentioned that the discontinuity of bonds at the surface may introduce new allowed energy levels from which photoemission can occur. This source of distortion is expected to be small, since the surface extends over a thickness of a few Angstroms as compared with the absorption depths which usually exceed 100 Å. The density of surface states is also small [Ref. 55] compared with the density of states in the volume. Therefore,

photoemission from surface states should comprise a small fraction of the total. Even if such photoemission is observable, it will appear in localized regions of the energy distribution curve and, therefore, can be distinguished from the effects of band bending.

Charged surface states cause energy bands to be bent with respect to the Fermi level as shown in Fig. 31. The resulting effect on quantum efficiency near the threshold has been discussed by van Laar and Scheer [Refs. 43, 44, and 45] and Spicer [Refs. 41 and 42]. The energy distributions for surfaces with bent bands will be different from those for surfaces with unbent bands at the same photon energy. The mathematical relationship between the two types of energy distributions is determined as follows. First, a bending distribution function is used to determine the energy distribution in the vacuum, of electrons excited to the same final quantum mechanical state at different distances from the surface. Second, the number of electrons emitted in a small differential energy range in the vacuum is determined by adding the contribution from each of the available final quantum mechanical states.

2. The Bending Distribution Function

An energy level diagram for a semiconductor with bent bands is shown in Fig. 31. Let E' represent the energy level referred to the top of the valence band (corresponding to identical quantum states), and let E represent the energy level referred to the top of the valence band far from the surface (corresponding to a fixed energy level with respect to the

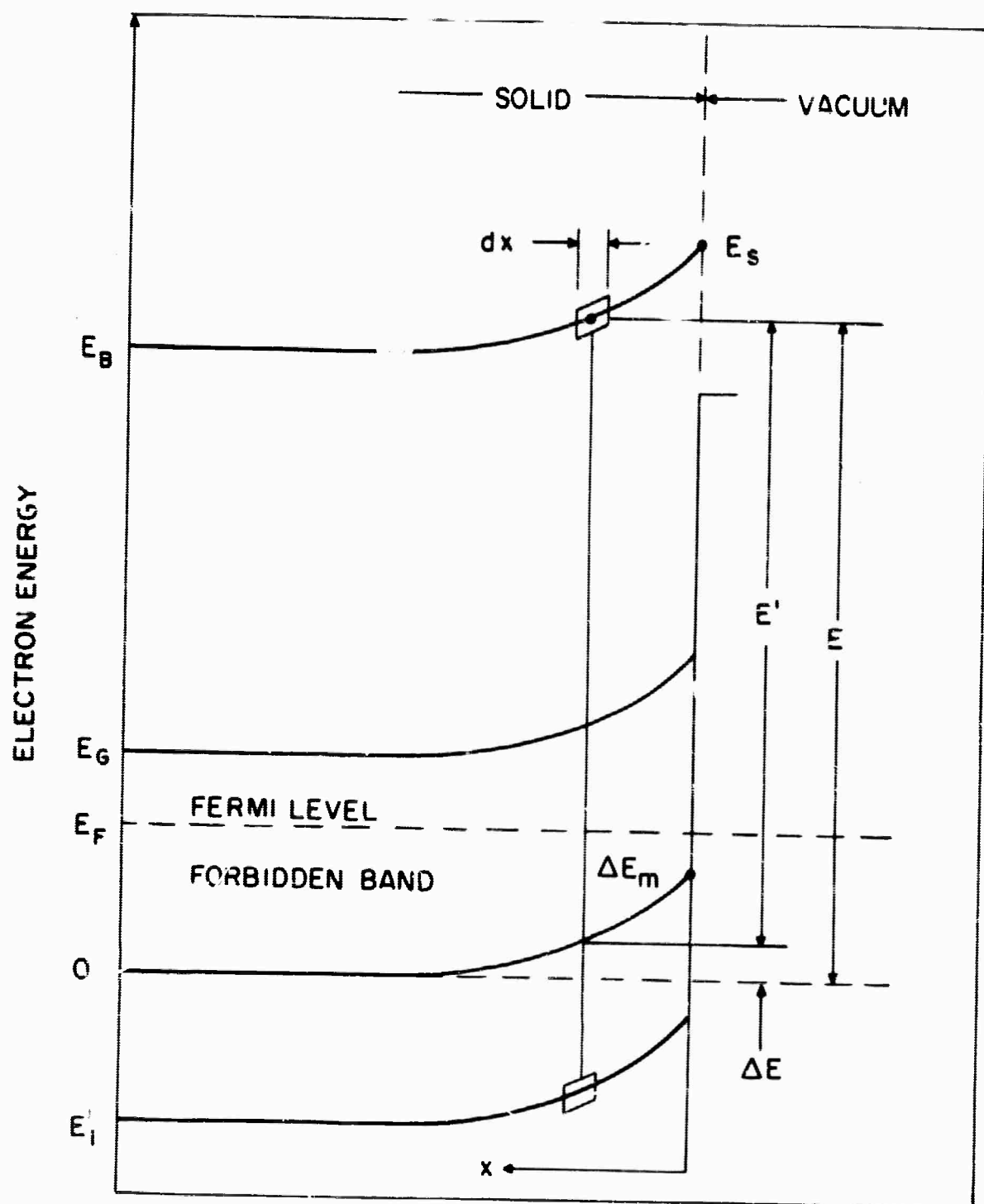


FIG. 31. ENERGY VERSUS DISTANCE DIAGRAM FOR A SOLID WITH BAND BENDING.

Fermi level). The illumination is assumed to be weak, so that the position of the Fermi level remains unchanged after illumination. For a given photon energy, the matrix element connecting the initial state E_i to the final state E_f is assumed to be independent of the distance from the surface at which the transition occurs. This assumption may not be valid if the field due to band bending is sufficiently large.

The bending distribution function determines the distribution of energies in vacuo of electrons which are excited at different distances from the surface inside the solid to identical final quantum states. The details of the identical bending distribution function depend on the potential as a function of distance in the material for a given quantum state. Many conclusions can be made about the bending distribution function without a detailed knowledge of the band shape. The band shape as a function of distance in the material depends on the mechanisms which neutralize surface charge. Dousmanis and Duncan [Ref. 56] have calculated the band shape for several specific situations.

As the escaping electron travels toward the surface, its energy E with respect to the Fermi level remains constant in the absence of scattering; however, its probability of scattering is determined by the energy E' which in turn depends on the distance between the electron and the surface, if the bands are bent. Therefore, an average attenuation length must be used. In the following discussion, average attenuation

lengths, $\bar{L}(E)$ and $\bar{L}(E')$, will be assumed. Since in this treatment E and E' are almost identical, these attenuation lengths can be used interchangeably except in a few limited energy ranges where the scattering probability changes rapidly with a change in E or E' . Equation (11) with E' substituted for E , since transition probabilities are determined by E' , gives the probable number of electrons dn in the energy range between E' and $E'+dE'$ which are excited at a distance x from the surface and which subsequently escape to the surface without losing energy. After substitution of E' and $\beta(E',h\nu) = \alpha(h\nu) + 1/\bar{L}(E')$ Eq. (11) becomes

$$dn(E',h\nu,x) = -\alpha'(E',h\nu)F_t(h\nu)e^{-\beta(E',h\nu)x}dx \quad (33)$$

Integration of Eq. (33) over all x , holding E' fixed, results in an expression similar to Eq. (12) for the number of electrons per unit energy range excited to a final energy level E' given by

$$n(E',h\nu,x) = \frac{\alpha'(E',h\nu)F_t(h\nu)}{\beta(E',h\nu)} \quad (34)$$

Substitution of Eq. (34) in Eq. (33) results in the relation

$$dn(E',h\nu,x) = -\beta(E',h\nu)n(E',h\nu)e^{-\beta x}dx \quad (35)$$

In Eq. (35) x depends on the energy difference $\Delta E = E-E'$ through the functional relation

$$x = x(\Delta E) \quad (36)$$

for which the corresponding differential relation is

$$dx = \frac{dx}{d(\Delta E)} d(\Delta E) = - \left| \frac{dx}{d(\Delta E)} \right| d(\Delta E) \quad (37)$$

Substitution of Eqs. (36) and (37) in Eq. (35) gives

$$dn(E, \Delta E, hv) = \frac{n(E - \Delta E, hv) \beta(E, hv) e^{-\beta x} d(\Delta E)}{\left| \frac{d(\Delta E)}{dx} \right|} \quad (38)$$

in which E and ΔE are used in place of E' and x to specify the location of the differential element, and $\beta(E', hv)$ is replaced by $\beta(E, hv)$ since $\bar{L}(E') \approx \bar{L}(E)$ for reasons previously discussed.

A bending distribution function is defined by separating Eq. (38) into two parts. The first part represents the number of electrons per unit energy range which are available for photoemission from a pair of quantum states with final energy $E' = E - \Delta E$ in the absence of band bending. The second part represents the fraction of electrons per unit energy range due to the above transition which have their final energy shifted to energy E as a result of band bending, and is called the bending distribution function, given by

$$B(\Delta E, E, hv) = \frac{\beta(E, hv) e^{-\beta x(\Delta E)}}{\left| \frac{d(\Delta E)}{dx} \right|} \quad (39)$$

Equation (32) may then be written as follows

$$dn(\Delta E, E, hv) = \beta(\Delta E, E, hv) n(E - \Delta E, hv) d(\Delta E) \quad (40)$$

3. The Energy Distribution Curve with Band Bending

The energy distribution with band bending is related to the energy distribution without band bending through the bending distribution function by multiplying Eq. (40) by a threshold function and then integrating over all ΔE resulting in the expression

$$n_B(E, hv) = \int_0^{\Delta E_m} B(\Delta E, E, hv) n(E - \Delta E, hv) T(E) d(\Delta E) \quad (41)$$

Figure 32 shows the relationship between hypothetical energy distribution curves without (solid) and with (dotted) band bending. The threshold function is omitted for clarity. Note that the bending distribution function is a function of E . Equation (41) can be used to calculate energy distributions with band bending, from specific unbent energy distributions. In general it is more useful to understand the relationship between the energy distributions based on the properties of the bending distribution function as discussed in the following paragraph.

4. Quantitative Estimates of the Effects of Band Bending on Energy Distribution Curves

Three principal effects of band bending on the energy distribution curve are discussed. First, peaks appearing in an energy distribution curve for unbent bands have their absolute energy level shifted as a result of band bending, whereas the spacing between peaks is not greatly affected by band bending (see Fig. 32). The amount of shift can be

estimated by calculating the mean value of the bending distribution function given by Eq. (39). Second, band bending causes the peaks to broaden by an amount which can be estimated by determining the standard deviation of the bending distribution function. Third, the surface states which produce band bending may also cause a change in the electron affinity of the material, resulting in a different threshold function. The magnitudes of the first two of these effects, which are estimated from the bending distribution function, are determined for the special cases of an exponential-potential-versus-distance relation and a linear potential versus distance relation. The results differ only in a minor way from similar results which have been calculated using a more exact band shape for a specific case from the data of Dousmanis and Duncan [Ref. 56].

a. Exponential Potential-Versus-Distance Relation

For exponential bands the band shape as a function of distance from the surface is given by

$$\Delta E = (E - E') = \Delta E_m e^{-\gamma x} \quad (42)$$

in which $1/\gamma$ is the characteristic length for band bending in the material. The bending distribution function calculated from Eqs. (39) and (42) is given by

$$B(E, \Delta E, h\nu) = \frac{1}{\Delta E_m} \frac{\beta}{\gamma} \left(\frac{\Delta E}{\Delta E_m} \right)^{(\beta/\gamma)-1} \quad (43)$$

and is plotted in Fig. 33 for several different values of the parameter β/γ . For $\beta/\gamma < 1$ the function goes to infinity at

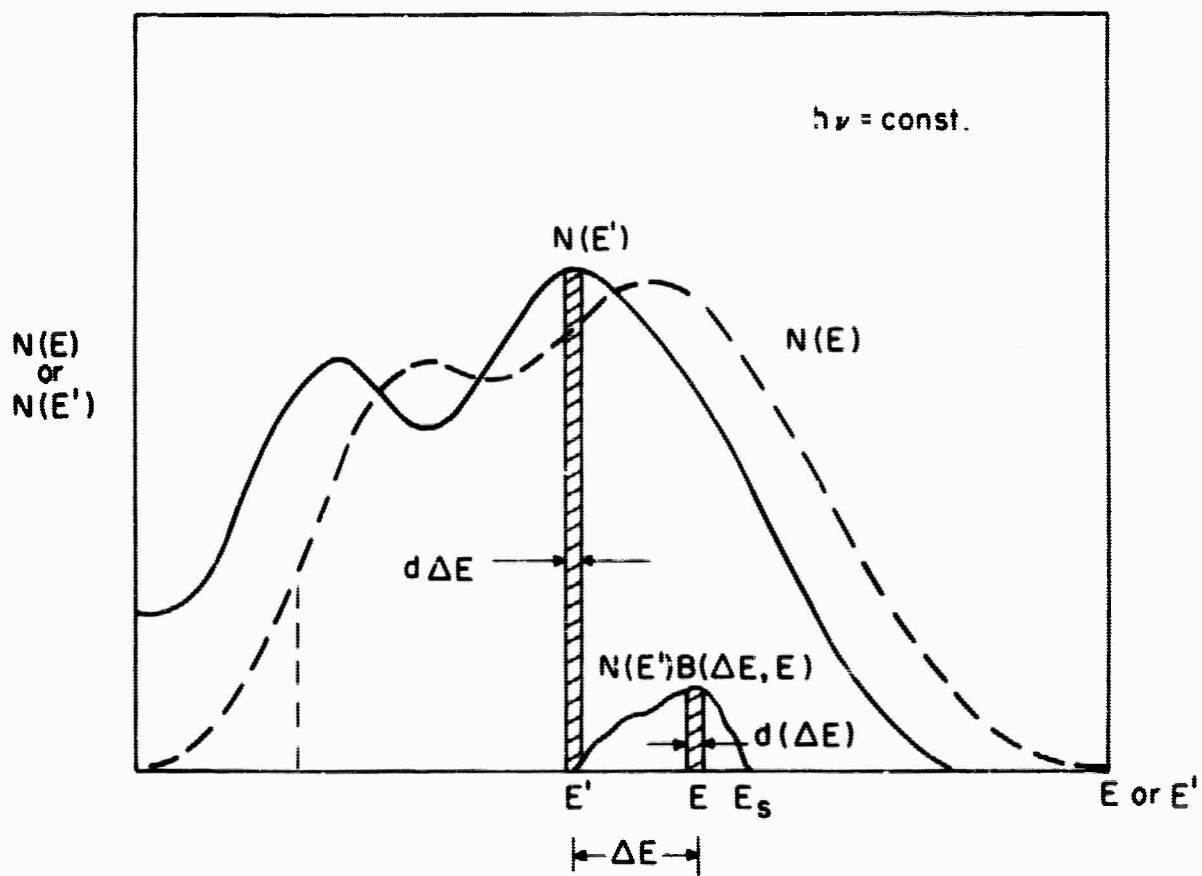


FIG. 32. USE OF THE BENDING DISTRIBUTION FUNCTION TO RELATE ENERGY DISTRIBUTIONS FOR BENT AND FLAT BANDS.

$\Delta E = 0$; however, the area under the curve as $\Delta E \rightarrow 0$ is finite so that its contribution to the energy distribution curve with band bending is also finite.

With band bending, the average shift in energy of electrons that are emitted from identical final quantum states is calculated from the distribution function of Eq. (43). The result is

$$\langle \Delta E \rangle = \Delta E_m \frac{1}{1 + \gamma/\beta} \quad (44)$$

as plotted in Fig. 34. Note that β is a function of E and $h\nu$, while γ is dependent only on the nature of the band bending as can be seen from Eq. (42). The position of a peak as a function of photon energy in the presence of band bending depends on the parameter γ/β as well as on the factors discussed in Sec. D. The change in $\langle \Delta E \rangle$ corresponding to a given percentage change in γ/β is given by the relation

$$\frac{\gamma}{\beta} \frac{d(\langle \Delta E \rangle)}{d(\gamma/\beta)} = \frac{\Delta E_m (\gamma/\beta)}{(1 + \gamma/\beta)^2} = \frac{\langle \Delta E \rangle (\Delta E_m - \langle \Delta E \rangle)}{\Delta E_m} \quad (45)$$

This relation is plotted in Fig. 34b as a function of $\Delta E / \Delta E_m$. The parameter $\langle \Delta E \rangle$ is related to γ/β through Fig. 34a. A change in γ/β will cause the largest change of $\langle \Delta E \rangle$ for $\gamma/\beta = 1$.

The standard deviation of ΔE is determined from Eq. (43) to be

$$[\langle (\Delta E)^2 \rangle - \langle \Delta E \rangle^2]^{\frac{1}{2}} = \Delta E_m \left(1 - \frac{\langle \Delta E_m \rangle}{E_m} \right) \sqrt{\frac{(\langle \Delta E \rangle / \Delta E_m)}{2 - (\langle \Delta E \rangle / \Delta E_m)}} \quad (46)$$

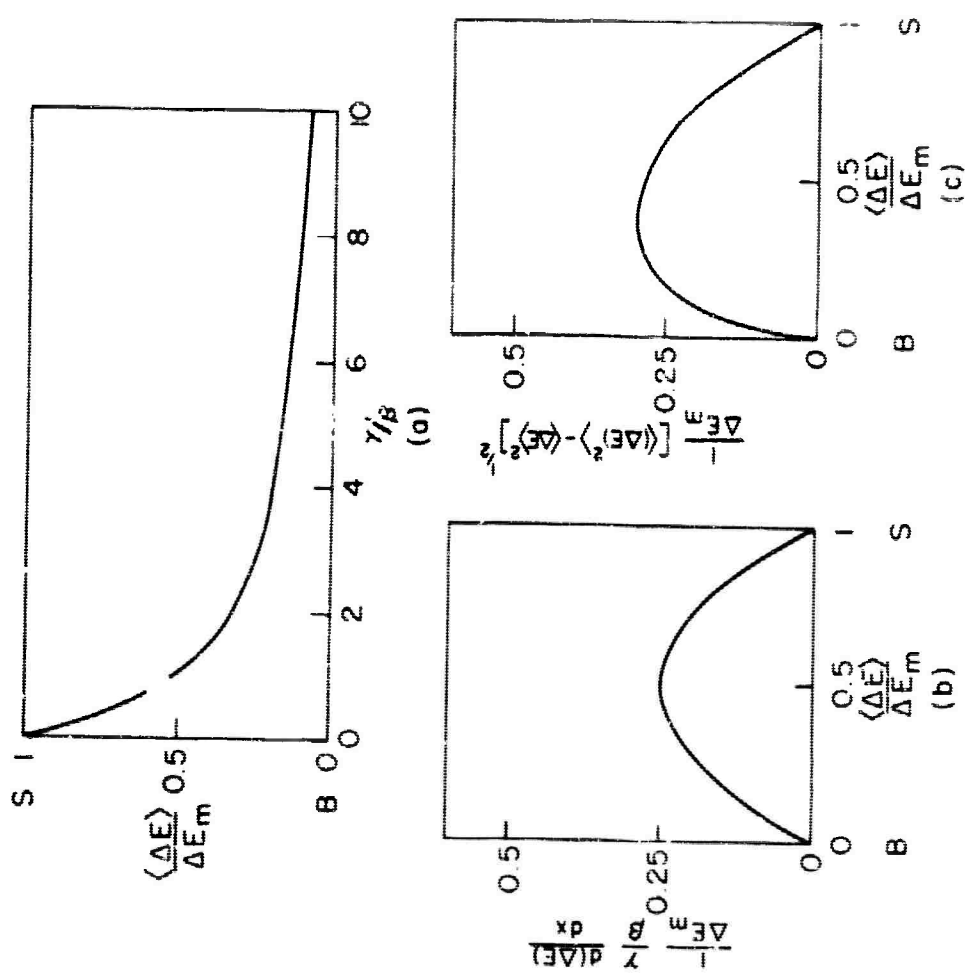


FIG. 34. AVERAGE ENERGY (a), SHIFT OF AVERAGE ENERGY (b), AND STANDARD DEVIATION (c) OF THE DISTRIBUTION FUNCTION FOR EXPONENTIAL BANDS.

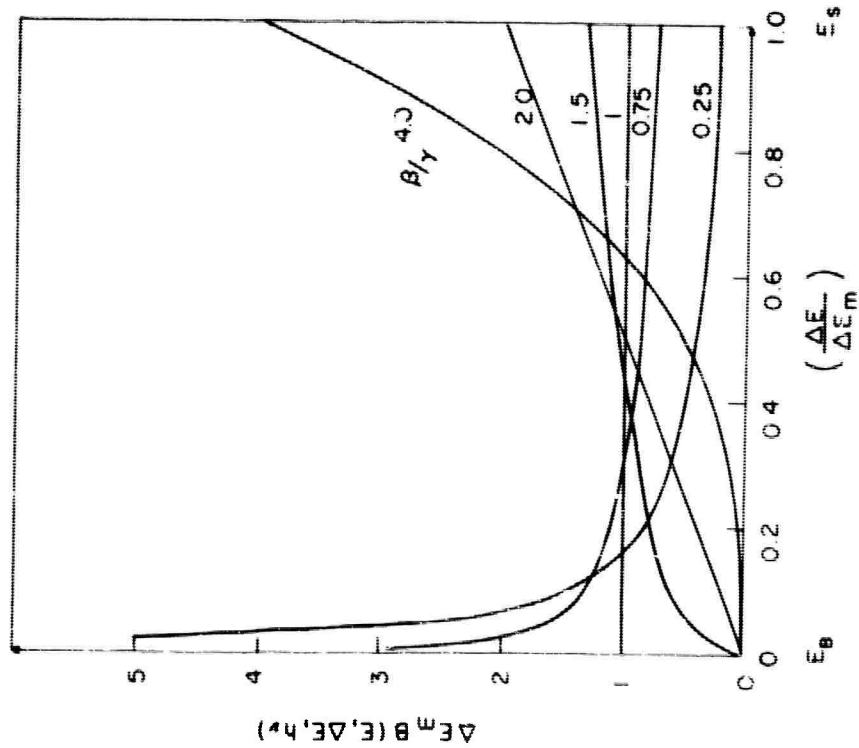


FIG. 33. BENDING DISTRIBUTION FUNCTIONS FOR EXPONENTIAL DEPENDENCE OF ENERGY ON DISTANCE.

which is plotted in Fig. 34c. This indicates that the maximum loss of resolution due to band bending occurs for $\gamma \approx \beta$ and has a value of $0.6 \Delta E_m$ which is defined here as twice the deviation.

b. Linear Potential-Versus-Distance Relation

If no net charge is available to neutralize the surface charge in the region from which photoemission can occur, the field \mathcal{E} is constant and the potential is a linear function of distance given by

$$\Delta E = E_s - F' = \mathcal{E}x \quad (47)$$

as shown in Fig. 35. This situation can exist in a material which is lightly doped, or it can occur if measurements are made at a photon energy for which the combined characteristic length for absorption and escape $1/\beta$ is small. Here, the reference energy is taken as the energy level at the surface E_s since the corresponding potential far from the surface cannot be specified. The bending distribution function is

$$B(\Delta E, E_s, hv) = \frac{\beta(E_s, hv) e^{-\beta \Delta E / \mathcal{E}}}{\mathcal{E}} \quad (48)$$

and has a mean value and a standard deviation of

$$\langle \Delta E \rangle = \mathcal{E} / \beta \quad (49a)$$

$$[\langle (\Delta E)^2 \rangle - \langle \Delta E \rangle^2]^{\frac{1}{2}} = \mathcal{E} / \beta \quad (49b)$$

respectively. The bending distribution function is plotted

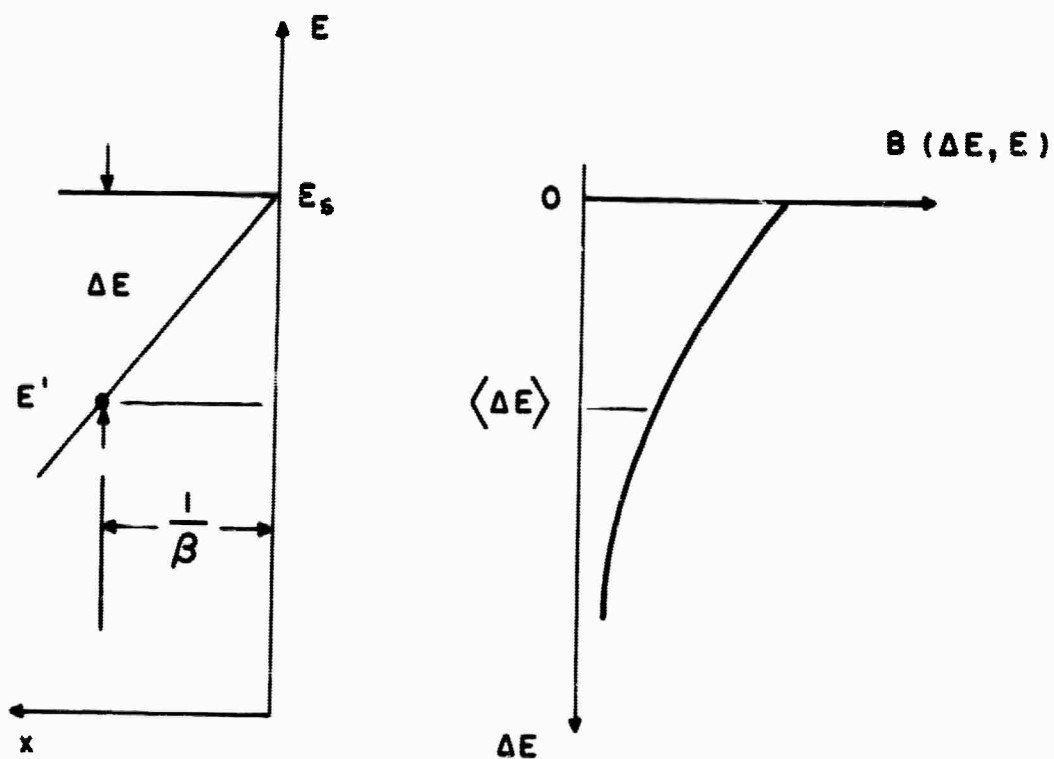


FIG. 35. ENERGY VERSUS DISTANCE DIAGRAM AND THE CORRESPONDING BENDING DISTRIBUTION FUNCTION FOR THE CASE OF A CONSTANT ELECTRIC FIELD.

in Fig. 35, and shows that electrons which are excited to a single final quantum state appear in an exponential distribution in the vacuum.

The electric field at the surface is related to the surface charge density N_s by

$$E = \frac{N_s q}{\epsilon} \quad (50)$$

in which ϵ is the dielectric constant of the material and q is the electronic charge. Equations (49) and (50) are combined into the relation

$$\Delta E = \frac{N_s q}{\beta \epsilon} \quad (51)$$

to estimate the surface charge required to produce an observable effect due to band bending. A typical example for CdS is given using a minimum observable value of ΔE of 0.1 eV, a relative dielectric constant of 11.6 and a typical characteristic length $1/\beta$ of 100 Å. The required surface charge is $N_s = 6.4 \times 10^{13}$ per cm² with a corresponding field of 10^5 v per cm.

No conclusive evidence of band bending was found in the photoemission measurements on CdS although some effects may be present. On the basis of the above discussion, it is possible that band bending could contribute a maximum of about 0.1 eV reduction in resolution and a maximum shift in peak location of ± 0.1 eV. Since the resolution of the measurements is around 0.1 eV, such effects of band bending are not considered

significant. No new peaks in the energy distributions are expected in this case as a result of band bending.

c. Special Potential-Versus-Distance Relation

Bending distribution functions have been determined graphically from the data of Dousmanis and Duncan for a surface potential of 0.5 v and a bulk potential of -0.44 v referred to the Fermi level for intrinsic material. The strong similarity between these distribution functions which are shown in Fig. 36 and the distribution functions for exponential bands shown in Fig. 33 indicates that the general features of band bending are well represented by the assumption of exponential bands.

F. THE EFFECT OF ELECTRON-ELECTRON SCATTERING ON PHOTOEMISSION FROM SEMICONDUCTORS

Electron-electron scattering resulting in pair production can distort energy distribution curves in photoemission from semiconductors. Berglund [Ref. 32] has developed an approximate theory for electron-electron scattering in metals which considers once scattered electrons. This theory is based on the assumption that the mean free path for inelastic scattering is much shorter than the absorption length which is in turn much shorter than the mean free path for elastic scattering. The theory also assumes that the scattering is the result of a short range screened coulomb interaction. Experimental evidence from photoemission curves on CdS indicates that many features of the above theory may apply to semiconductors.

The energy levels involved in this type of scattering event

are shown in Fig. 37. An electron in the conduction band with energy E' scatters to energy E by exciting an electron in the valence band with energy E_0 to an energy $E_0 + (E' - E)$ so that energy is conserved. It is assumed that conservation of \vec{k} is not required in the transitions. Each of the transitions is assumed to occur with a probability density proportional to the product of the densities of states. Thus the probability per unit time $p_s(E', E)$ of scattering from an energy E' to an energy E is given by

$$p_s(E', E) = K \int_0^\infty N_c(E) N_v(E_0) N_c(E_0 + E' - E) dE_0 \quad (52)$$

with the total probability per unit time of scattering from energy E' given by

$$P_s(E') = \int_0^\infty p_s(E', E) dE \quad (53)$$

The scattering mean free path $\ell_e(E')$ is then found by using the relation

$$\ell_e(E') = V_g(E') \tau(E') = V_g(E') / P_s(E') \quad (54)$$

and the energy distribution of photoemitted electrons becomes

$$N(E) = K_4 \frac{1}{\alpha + \frac{1}{L(E)}} \left[\alpha'(E) + 2 \int_E^{h\nu} \frac{p_s(E', E)}{P_s(E')} \alpha'(E') dE' \right] \quad (55)$$

where K_4 is an unknown constant. The attenuation length $L(E)$ may become an important factor in determining the shape of the energy distributions at high electron energies. Therefore, the

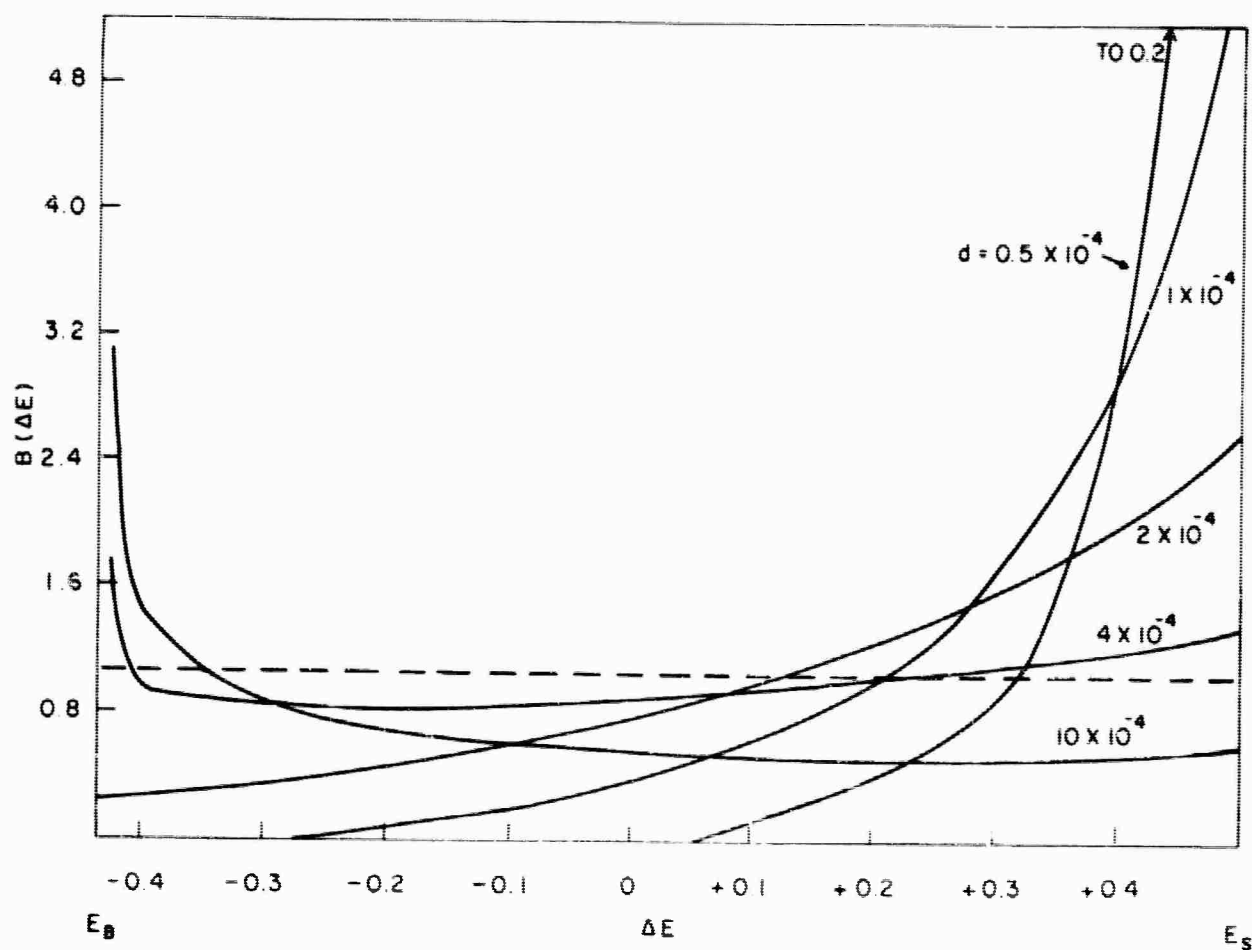


FIG. 36. BENDING DISTRIBUTION FUNCTION CALCULATED FROM DATA OF DOUSMANIS AND DUNCAN. (Compare with Fig. 33.)

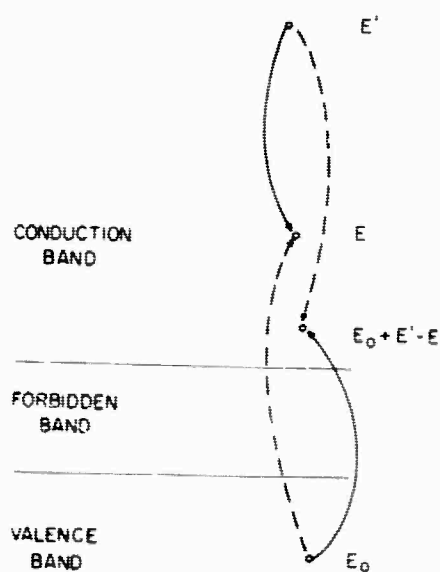


FIG. 37. ENERGY LEVEL DIAGRAM FOR ELECTRON-ELECTRON SCATTERING AND PAIR PRODUCTION IN A SEMICONDUCTOR.

term

$$\frac{1}{\alpha(h\nu) + \frac{1}{L(E)}} \quad (56)$$

must be included explicitly in the energy distribution. The dependence of $L(E)$ on $\ell_e(E)$ has been discussed in Sec. C2. From the results of age theory, one can conclude that the dependence lies somewhere between $L(E) \propto \ell_e(E)$ and $L(E) \propto \sqrt{\ell_e(E)}$. Assuming the linear dependence and constant group velocity, the first term in the energy distribution can be written approximately as

$$\frac{1}{\alpha} \cdot \frac{1}{1 + \frac{K_5 p_s(E')}{\alpha}} \quad (57)$$

where K_5 is an unknown constant. The term in the energy distribution equation given by Eq. (57) takes into account the loss of high energy electrons due to inelastic scattering as shown in Chapter IV, Sec. I.

The energy distribution of inelastically scattered and secondary electrons is taken into account by the second term in the brackets in Eq. (55). This term represents the generation rate as a function of energy for once scattered electrons and secondary electrons in the solid. The escape conditions in the presence of combined elastic and inelastic scattering are not well understood. In Chapter IV, Sec. I, this generation term is used to estimate the energy distribution of electrons due to inelastic scattering.

IV. EXPERIMENTAL RESULTS OF PHOTOEMISSION FROM CdS INTERPRETED IN TERMS OF BULK PROPERTIES

A. TEST SAMPLES AND PROCEDURES

The electrical and chemical properties of CdS samples from which photoemission measurements have been made are listed in Table I. The suppliers of the samples are also indicated.

The samples are divided into categories according to the surface preparation, and are designated by the following symbols:

- 1) VC for samples cleaved and measured in high vacuum (10^{-9} torr);
- 2) T for samples cleaved in air, sealed in a glass tube, outgassed by baking for about eight hours at 140°C , and sealed off at a pressure of approximately 10^{-8} torr; 3) AC for samples cleaved in air and immediately tested in low vacuum (H_2 atmosphere of 10^{-4} torr); and 4) LVC for the sample which was cleaved and tested in a low vacuum (H_2 atmosphere of 10^{-4} torr).

The primary purpose of this chapter is to interpret the photoemission in terms of the band structure, the optical properties, and the other mechanisms involved in bulk photoemission from CdS. The differences in the photoemission results obtained by the various techniques used in preparing the CdS surfaces, although they are large, can be attributed to physical and chemical changes near the surface that do not obscure the main features of the bulk photoemission properties. The principal changes are 1) reduction in the electron affinity, attributable to chemical changes at the surface, and 2) change in the relative amplitude of peaks in energy distributions taken at the same photon energy,

attributable to increased scattering due to adsorbed gas (see Chapter V). After photoemission from the high vacuum cleaved samples was measured, the samples were exposed to various gaseous environments and heat cycles. Photoemission measurements which were made on the samples after the vacuum was restored can be used to determine the effect of surface treatment on photoemission from CdS. These surface effects are discussed in detail in Chapter V.

TABLE 1. DATA ON CdS TEST SAMPLES

Supplier	Resistivity (Ω -cm)	Impurities	Cleavage Plane
VC1 Harshaw	2	pure*	$1\bar{2}10$
VC2 Harshaw	2	pure*	$1\bar{2}10$
VC3 Harshaw	2	pure*	$1\bar{2}10$
VC4 Harshaw	10^8 (dark)	S comp.	$1\bar{2}1c$
T1 Eagle Picher	0.1	.005% InCl_3	$U^{**}(\parallel \text{ to } c)$
T2 Eagle Picher	0.1	.005% InCl_3	$U^{**}(\parallel \text{ to } c)$
T3 Harshaw	2	pure*	$10\bar{1}0$
AC1 Eagle Picher	0.1	.005% InCl_3	$U^{**}(\parallel \text{ to } c)$
AC2 Harshaw	2	pure*	$10\bar{1}0$
AC3 Harshaw	2	pure*	$1\bar{2}10$
LVC1 Harshaw	10^8 (dark)	S comp.	$1\bar{2}10$

* Less than 1 ppm Al, Cu, Fe, Si, Li, Na, Ca; 50 ppm Zn

** U means unknown.

B. THE MEASURED ENERGY DISTRIBUTION OF PHOTOEMITTED ELECTRONS

1. Introduction

Energy distribution curves are presented in this section and are used to establish the absolute energy of maxima in the conduction and valence band densities of states. Details of the density of states functions are described in a later section.

2. Determination of the Absolute Energy Scale

The abscissa on the measured energy distribution curves presented later is the energy E_b of the electron referred to the collector. This energy in electron volts is equal to the applied retarding potential, and its value relative to the energy in the solid depends on the emitter and the collector work functions (see Fig. 25). The energy of the electron with respect to the top of the valence band is represented by E . This energy is independent of the work functions.

The energies E and E_b are related by either of the equations

$$E - E_b = \phi_m + E_F \quad (58a)$$

and

$$E - E_b = (E_A + E_G) + (\phi_m - \phi_s) \quad (58b)$$

(see Fig. 25 in Chapter IIF4, and Fig. 38). The energy at the Fermi level E_F is referred to the top of the valence band. The magnitudes of the electron affinity and of the band gap are given by E_A and E_G respectively, and the emitter and collector work functions are given by ϕ_s and ϕ_m respectively.

The energy difference $E - E_b$ is difficult to determine

exactly. It can be determined by measuring the collector work function ϕ_m (Chapter IIF4) and by determining the Fermi level from the electrical or the chemical properties of the material. However, the Fermi level at the surface may not be the same as in the bulk because of band bending or diffusion of impurities.

The energy difference can also be determined from the maximum electron energy $E_{b_{co}}$ referred to the collector, at a given photon energy $h\nu$ for which the maximum electron energy referred to the top of the valence band is $E_{co} = h\nu$. Then the energy difference is $E - E_b = h\nu - E_{b_{co}}$. The average value of the energy difference determined from several of the curves at the higher photon energies should be used. At the lower photon energies, photoemission from quantum states above the vacuum level can introduce errors. The energy distributions always extend over a greater energy range than would be predicted using the electron affinity determined from the yield curve. Most of the discrepancy is on the low energy end of the energy distribution where the photodiode goes into saturation. The uncertainty in $E - E_b$ represents a shift in the energy zero so that the spacing between peaks in the energy distribution is not affected by it.

In this work the energy difference $E - E_b$ is established using the photon energy and the maximum electron energy. The energy shift determined by adding the energy E_F to the collector work function was not used because of difficulties in determining these quantities accurately. If a marked

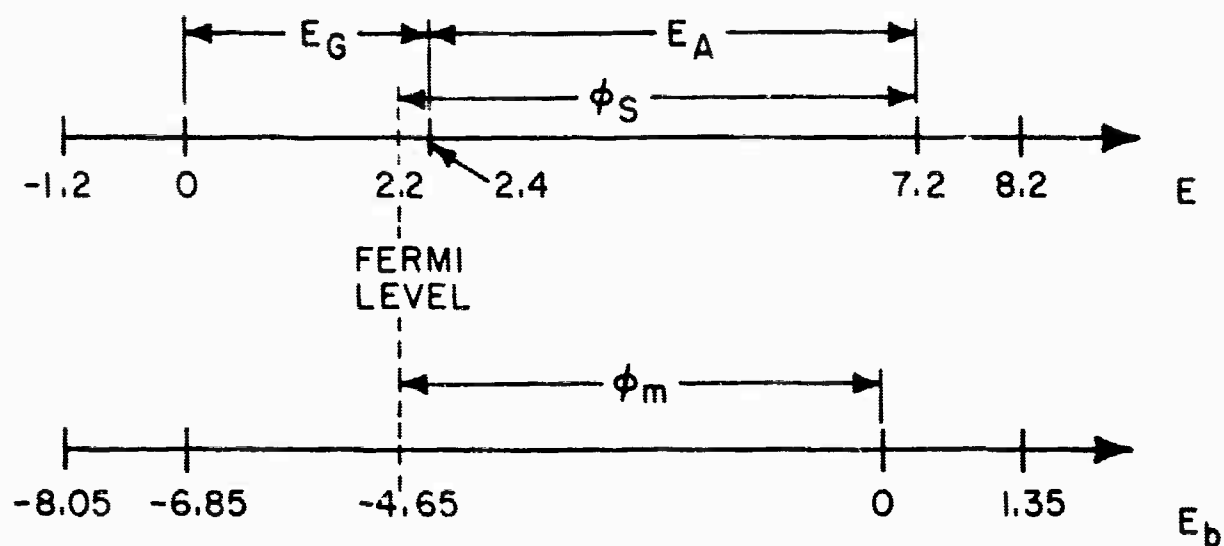


FIG. 38. ABSOLUTE ENERGY SCALES FOR PHOTOEMISSION FROM SEMICONDUCTORS. E_b is the energy referred to the collector. E is the energy referred to the maximum valence band energy.

difference is found between the energy scale shifts determined by the two methods, this indicates the presence of band bending. No band bending was detected within experimental errors.

3. High-Vacuum-Cleaved (VC) CdS

Energy distribution curves have been measured on the high-vacuum-cleaved CdS samples listed in Table 1. Measurements have been made 1) on conduction samples cleaved along two different cleavage planes parallel to the c axis, 2) on one conducting sample with and without visible light, and 3) on a photoconducting (insulating) sample which required visible illumination to obtain sufficient conductivity for the measurements. Energy distribution curves measured on the above samples at a given photon energy are substantially the same. No time variation in the shape of the curves was noted within several days after cleaving. The first curve on each sample was measured within three to five minutes after the sample was cleaved.

A typical complete set of energy distribution curves is presented for CdS sample VC-2 in Figs. 38a-f. The area under these curves has not been adjusted to be proportional to yield (normalized to yield). They were measured within one hour after the sample was cleaved.

The energy difference $E-E_b$ determined as described

in Sec. B2 is estimated to be 6.85 ± 0.2 eV for the vacuum cleaved sample under consideration. The energy scales for E and E_b are shown in Fig. 38.

A peak appears in the energy distributions of Fig. 39 which satisfies the relation [see Eq. (23)]

$$\left. \begin{aligned} E_b &= 1.35 \text{ eV} \\ E &= 8.2 \text{ eV} \end{aligned} \right\} \quad (59)$$

independent of photon energy. The peak at $E = 8.2$ eV can be associated with a maximum in the conduction band density of states located 8.2 ± 0.2 eV above the top of the valence band.

The energy distribution curves for VC2 are plotted as a function of $(E_b - h\nu)$ in Fig. 40 for photon energies from 9.8 to 11.6 eV. A peak appears in these curves at -8.05 eV independent of photon energy. This peak satisfies the relation [see Eq. (24)]

$$\left. \begin{aligned} E_b &= h\nu - 8.05 \text{ eV} \\ E &= h\nu - 1.2 \text{ eV} \end{aligned} \right\} \quad (60)$$

and can be associated with a high density of states lying

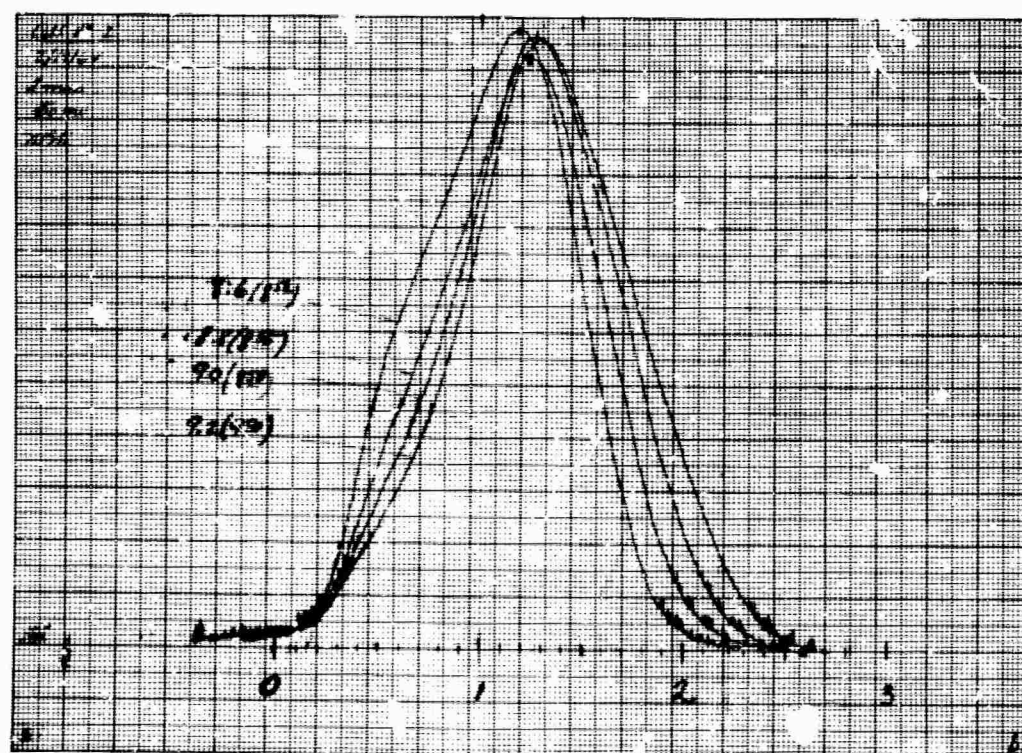
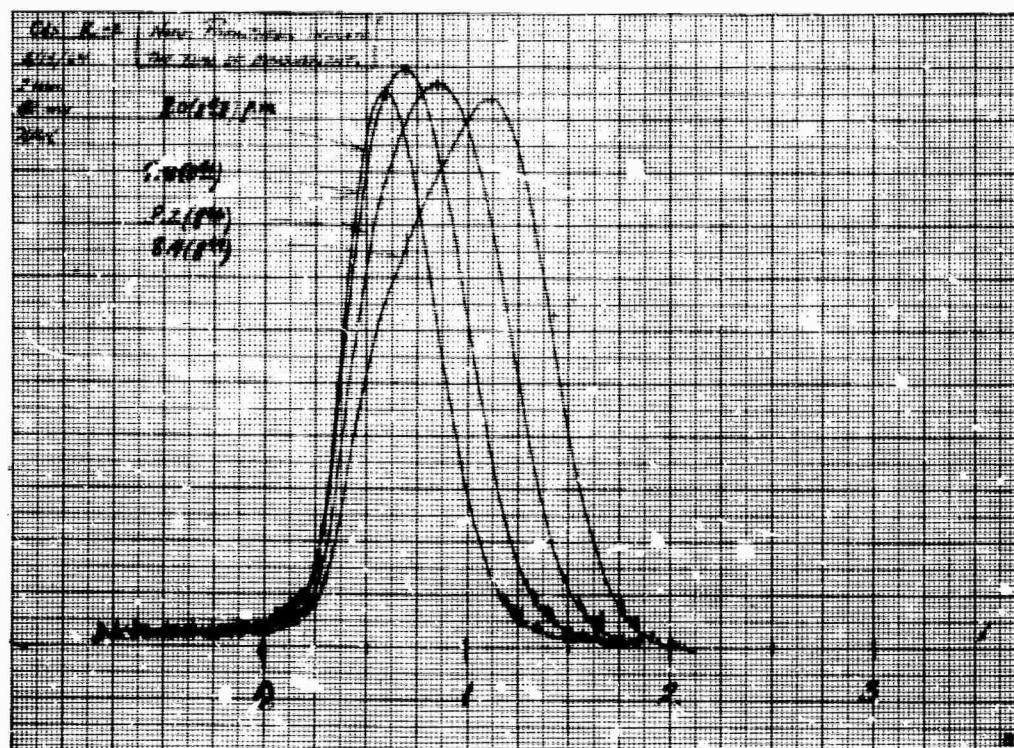
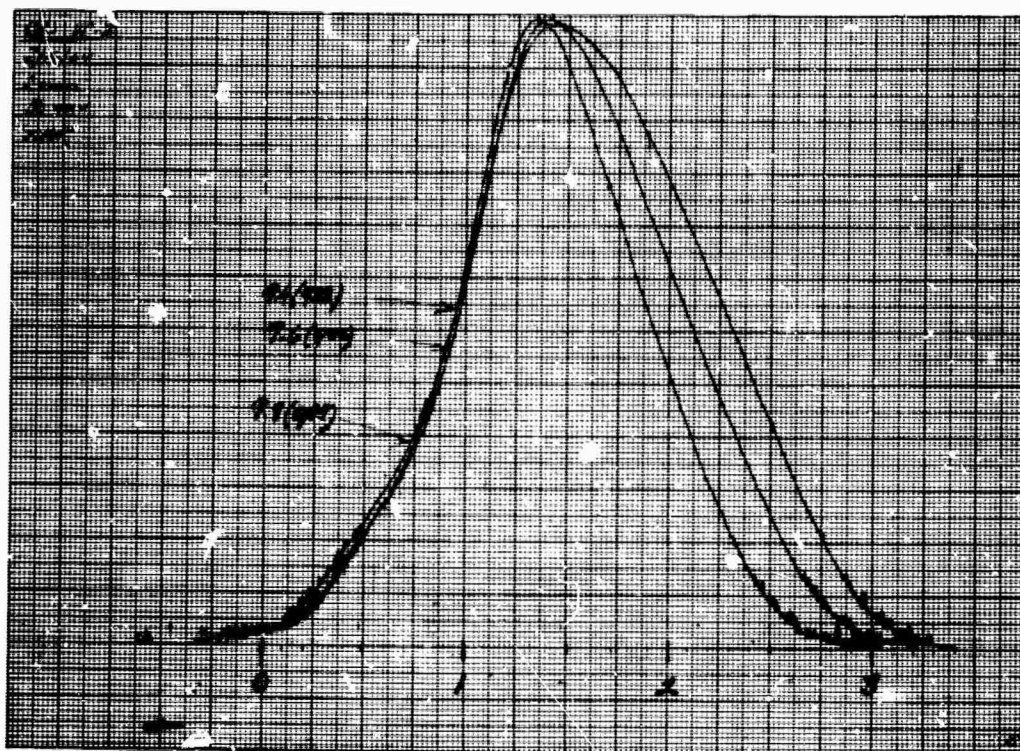
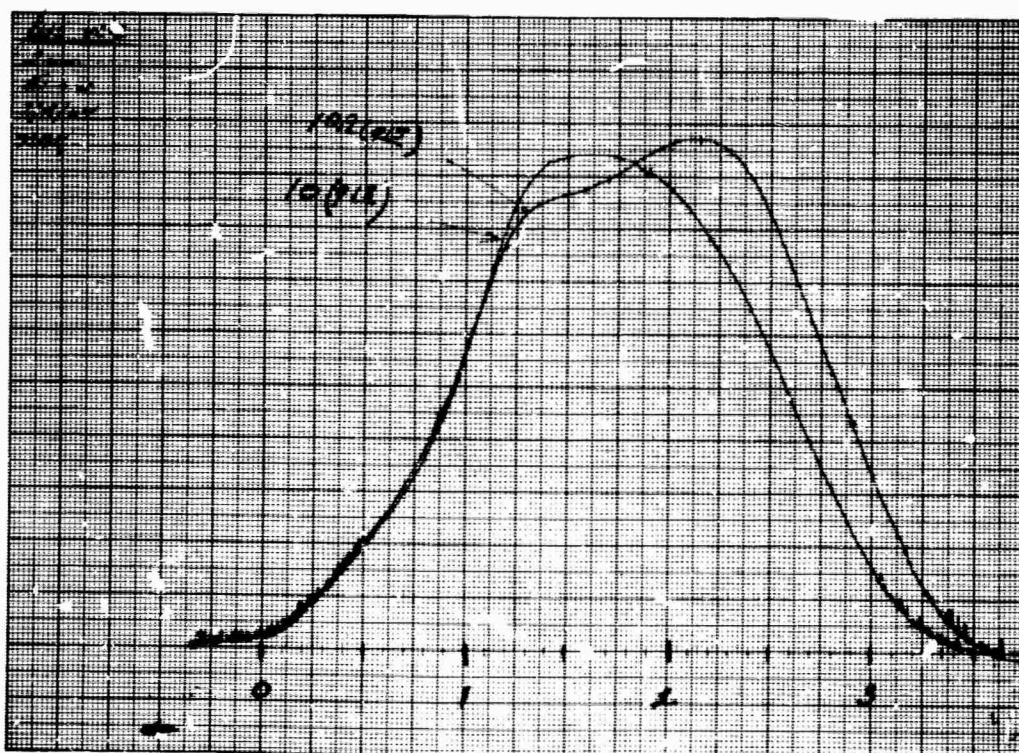


FIG. 39. ENERGY DISTRIBUTIONS FROM HIGH-VACUUM-CLEAVED Cds.

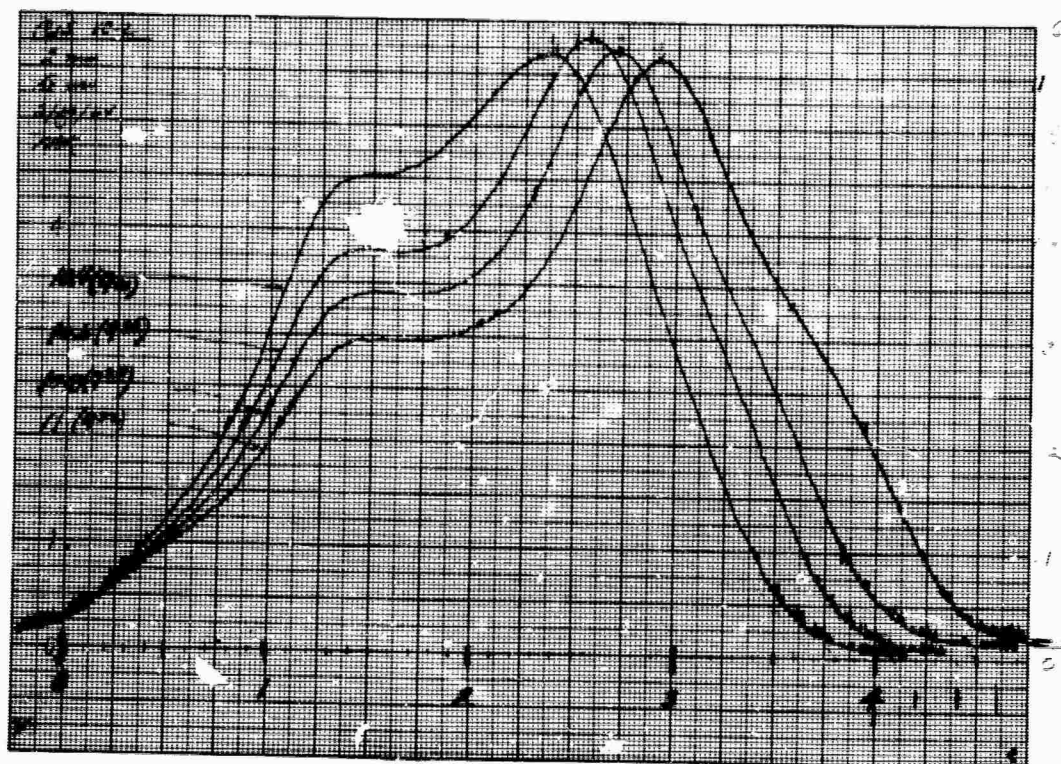


c. 9.4, 9.6, and 9.8 eV

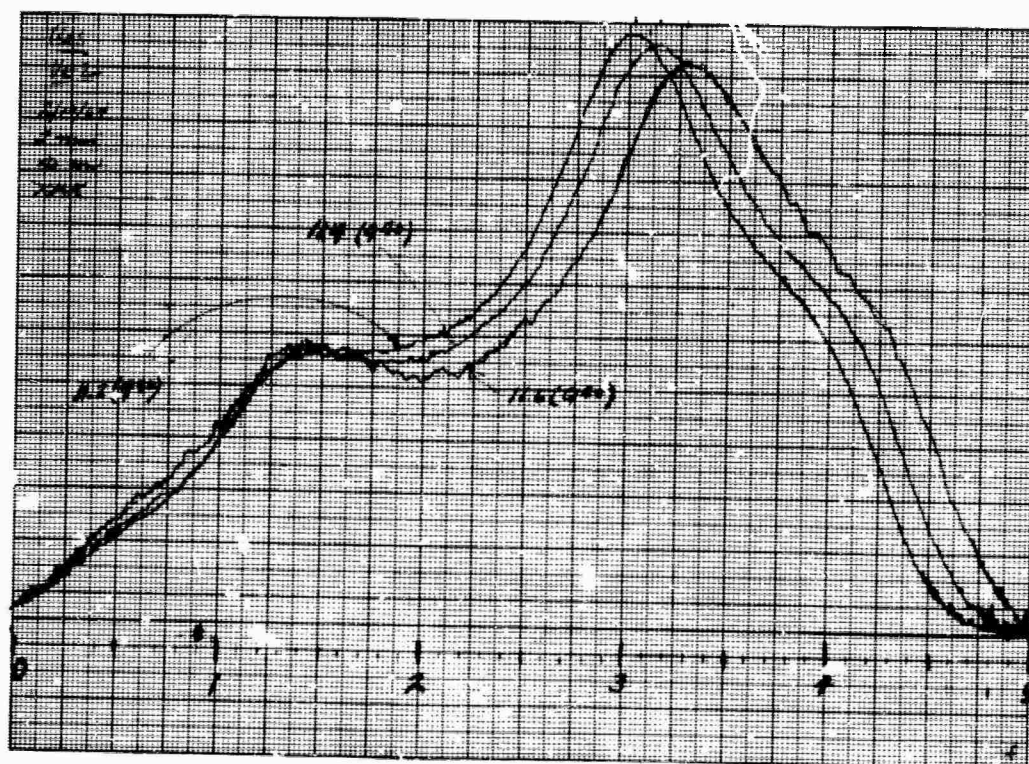


d. 10.0 and 10.2 eV

FIG. 39. ENERGY DISTRIBUTIONS FROM HIGH-VACUUM-CLEAVED CdS. (Continued)



e. 10.4, 10.6, 10.8, and 11.0 eV



f. 11.2, 11.4, and 11.6 eV

FIG. 39. ENERGY DISTRIBUTIONS FROM HIGH-VACUUM-CLEAVED CdS. (Continued)

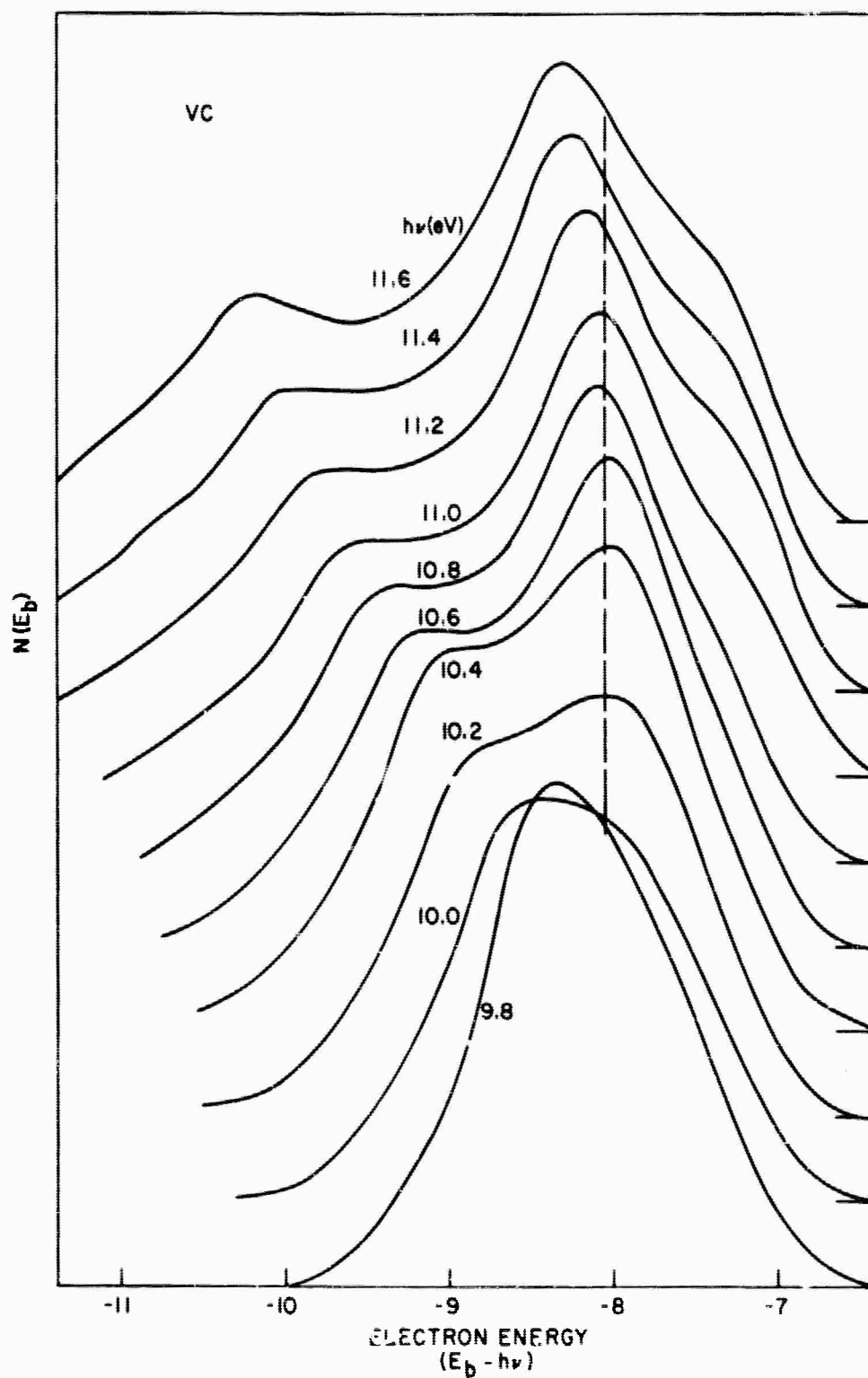


FIG. 40. ENERGY DISTRIBUTIONS FROM HIGH-VACUUM-CLEAVED CdS AS A FUNCTION OF $E_b - h\nu$. ($h\nu = 9.8$ to 11.6 eV.)

1.2±0.2 eV below the top of the valence band.

3. Low-Vacuum-Cleaved (LVC) CdS

Energy distribution curves measured on the low-vacuum-cleaved (LVC) CdS listed in Table 1 are plotted in Figs. 41 and 42 for photon energies between 8 and 10.2 eV. The energy shift in going from the solid into the vacuum is now estimated to be $E-E_b = 5.8$ eV. Peaks appear in these curves which satisfy the relations

$$\left. \begin{array}{l} E_b = 0.9 \text{ eV} \\ E = 6.7 \text{ eV} \end{array} \right\} \quad (61a)$$

and

$$\left. \begin{array}{l} E_b = 2.4 \text{ eV} \\ E = 8.2 \text{ eV} \end{array} \right\} \quad (61b)$$

These peaks can be associated with the peaks in the conduction band density of states at 6.7±0.2 eV and 8.2±0.2 eV. The absolute energies of the peaks were assigned by comparing this data with the data for the vacuum cleaved sample. The electron affinity is estimated to be 3.8±0.4 eV. The long tail of low energy electrons has not been explained. Most of the factors which contribute to lack of resolution (Chapter IIF3 and Ref. 32) have the largest effect in this region of the energy distribution curve.

For photon energies above 10.2 eV a peak appears in the energy distribution curves which satisfies the relations

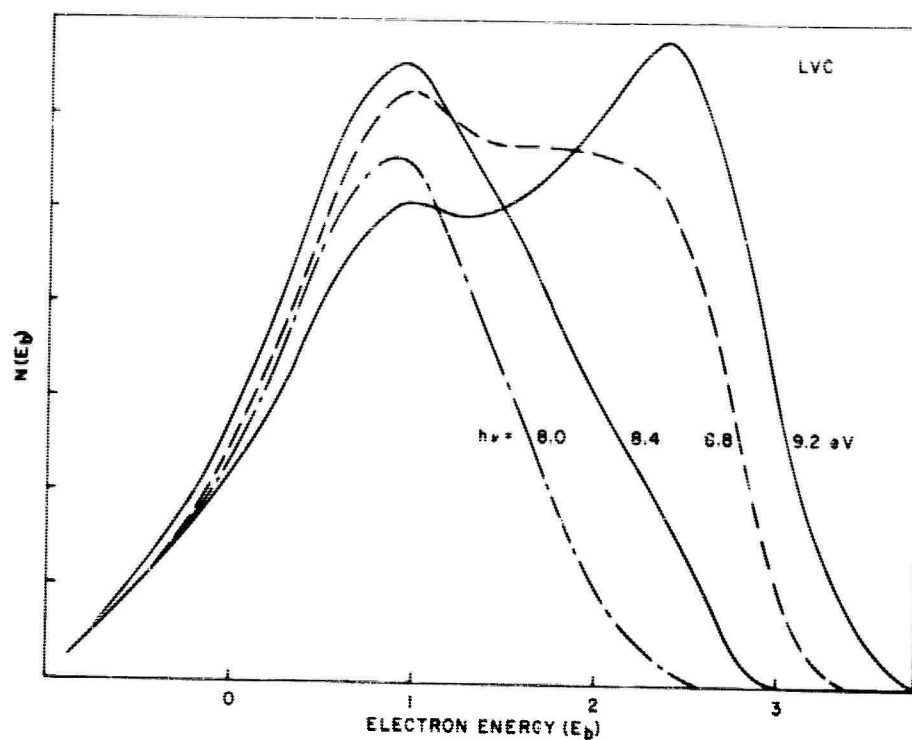


FIG. 41. ENERGY DISTRIBUTIONS FROM LOW-VACUUM-CLEAVED CdS. ($h\nu = 8.0, 8.4, 8.8$, and 9.2 eV.)

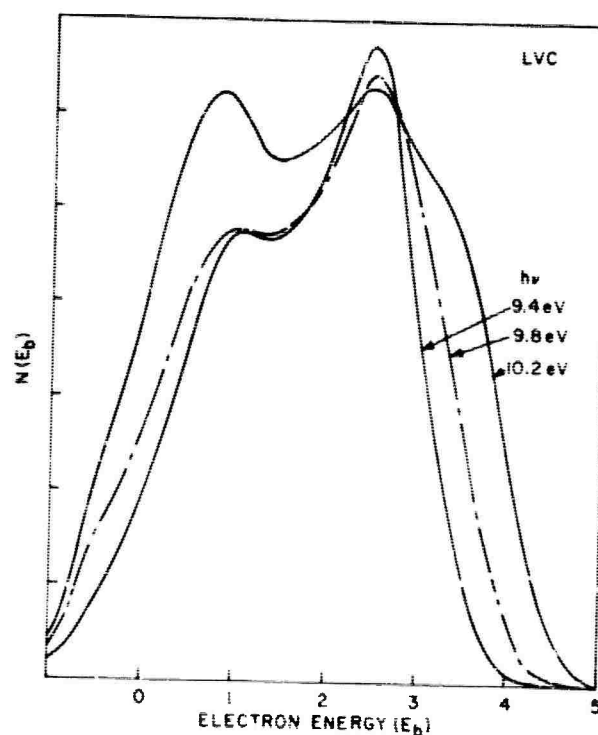


FIG. 42. ENERGY DISTRIBUTIONS FROM LOW-VACUUM-CLEAVED CdS. ($h\nu = 9.4, 9.8$, and 10.2 eV.)

$$\left. \begin{aligned} E_b &= h\nu - 7.0 \text{ eV} \\ E &= h\nu - 1.2 \text{ eV} \end{aligned} \right\} \quad (62)$$

as shown by the arrows in Figs. 43 and 44. This peak can be associated with the valence band peak located 1.2 ± 0.2 eV below the top of the valence band. The amplitude of this peak diminishes gradually at higher photon energies up to 14.2 eV as a result of scattering and a decrease in the conduction band density of states.

The LVC energy distribution at 21.2 eV is shown in Fig. 45. A peak appears in this curve at an energy $E_b = 6.0$ eV. On the basis of reflection [Ref. 7] and other photoemission data, this peak is believed to be associated with the valence band. If so, it must satisfy the relation

$$\left. \begin{aligned} E_b &= h\nu - 15.2 \text{ eV} \\ E &= h\nu - 9.4 \text{ eV} \end{aligned} \right\} \quad (63)$$

to be consistent with the other LVC data; it must, therefore, be located -9.4 eV below the top of the valence band. It is not possible to follow the movement of this peak over a wide range of photon energies to confirm its origin in the valence band. However, the following evidence indicates that the peak is probably associated with the valence band. The valence band peak at $E = -1.2$ eV is excited to the same final energy level ($E_b = 6.0$ eV) at a photon energy of 13.0 eV, and the

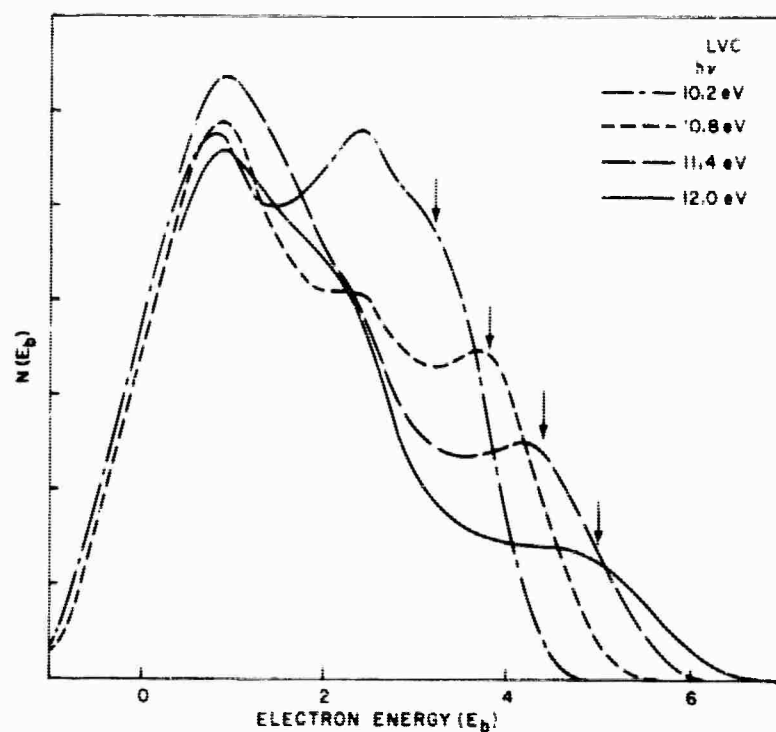


FIG. 43. ENERGY DISTRIBUTIONS FROM LOW-VACUUM-CLEAVED CdS. ($h\nu = 10.2, 10.8, 11.4, \text{ and } 12.0$ eV.)

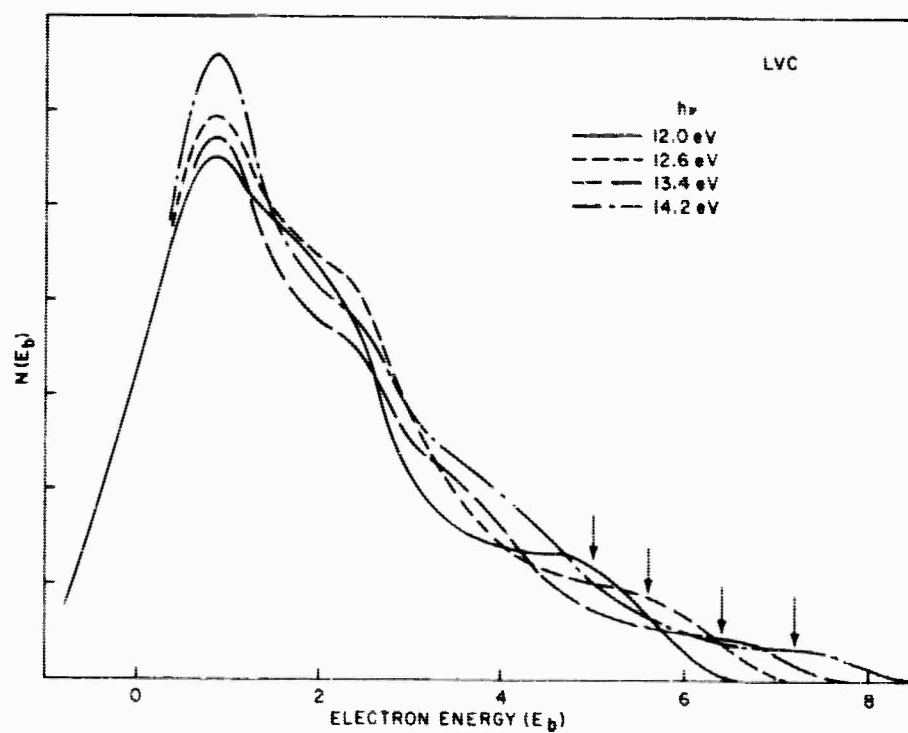


FIG. 44. ENERGY DISTRIBUTIONS FROM LOW-VACUUM-CLEAVED CdS. ($h\nu = 12.0, 12.6, 13.4, \text{ and } 14.2$ eV.)

corresponding energy distribution is plotted in Fig. 45 for comparison. From this it can be seen that a peak appearing at this final energy is not completely obscured by scattering. Figure 44 also indicates that there is no marked rise in excitations as the valence band peak $E = -1.2$ eV sweeps through the electron energy $E_b = 6.0$ eV, indicating that there is no peak in the conduction band density of states at this energy level.

Further evidence that the peak is in fact associated with a maximum in the valence band appears in the LVC energy distribution at 16.8 eV shown in Fig. 46. From Eq. (63) for $h\nu = 16.8$ eV, the peak must appear at $E_b = 1.6$ eV as indicated by the arrow labeled VB (-9.4) in Fig. 46. This energy lies between the peaks located by Eqs. (60) and (61) at $E_b = 0.9$ and 2.4 eV. Reference to the energy distribution curves in Figs. 43-46 indicates that the ratio of the lower energy peak to the higher energy peak increases for photon energies from 12 to 14.2 eV. Extrapolating to 16.8 eV, the ratio should be about 2 to 1. At $h\nu = 21.2$ eV (Fig. 45) the ratio increases to 2.5 to 1. In Fig. 46 the peak at $E_b = 2.4$ eV indicated by the arrow labeled CB (8.2) has essentially disappeared as compared with its strength in the 14.8 eV curve. Instead, a shoulder appears in the curve between $E_b = 1.5$ and 2.0 eV. This shoulder is believed to be caused by excitation from the maximum in the valence band located at $E = -9.4$ eV. If the excitation from the valence band were not present for

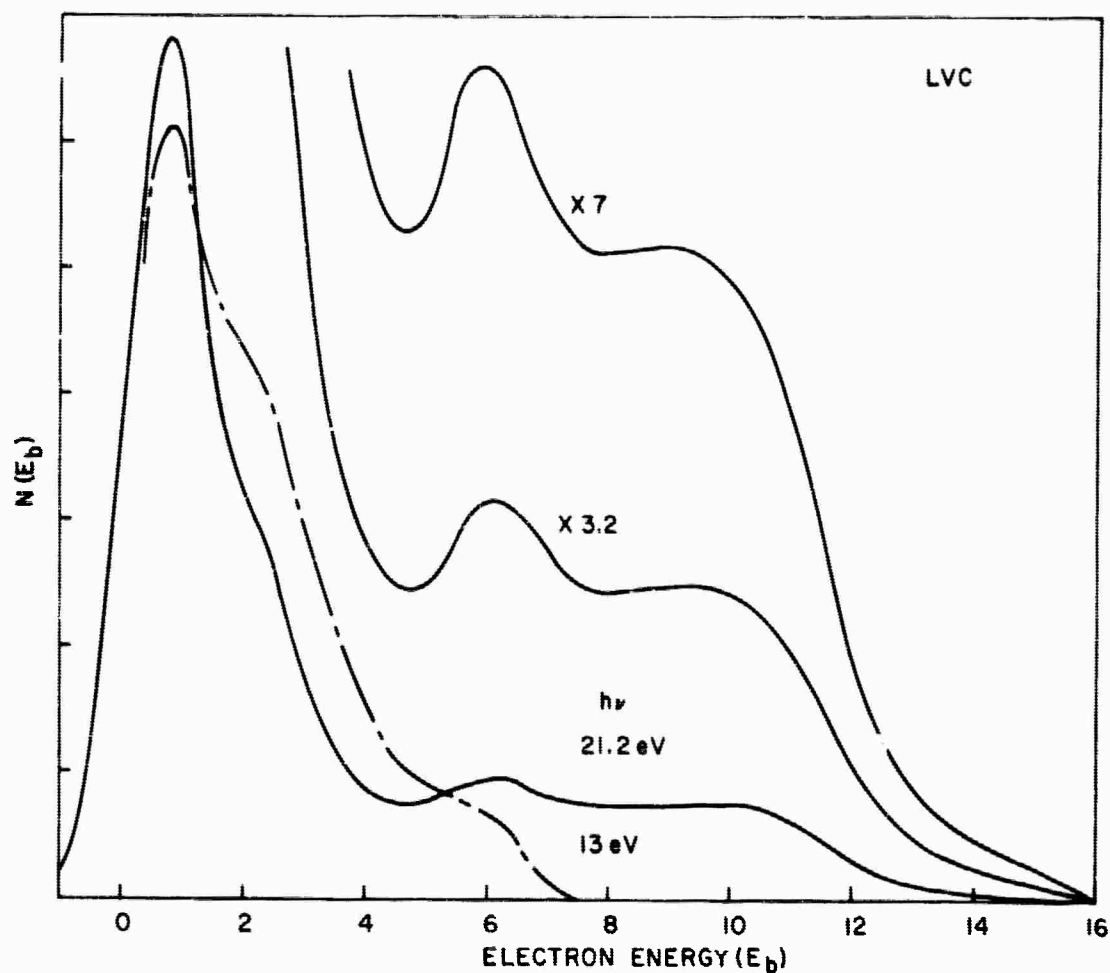


FIG. 45. ENERGY DISTRIBUTIONS FROM LOW-VACUUM-CLEAVED CdS. ($h\nu = 13.0$ and 21.2 eV.)

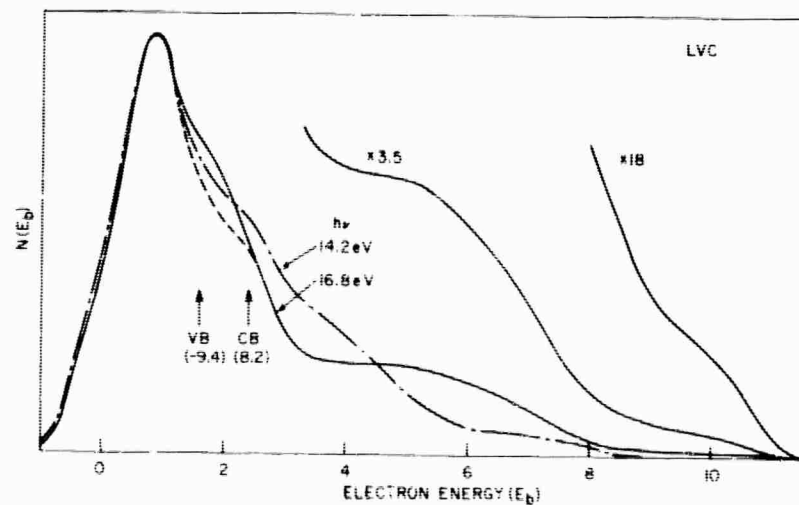


FIG. 46. ENERGY DISTRIBUTIONS FROM LOW-VACUUM-CLEAVED CdS. ($h\nu = 14.2$ and 16.8 eV.)

$h\nu = 16.8$ eV, the estimated energy distribution would be as shown by the dotted line. This estimate is qualitative and is intended to show the basis of the argument.

A peak in yield near $h\nu = 16.8$ eV (see Sec. G) provides further evidence of coupling between maxima in the conduction and valence bands. However, this rise in yield could also be attributed to secondary emission.

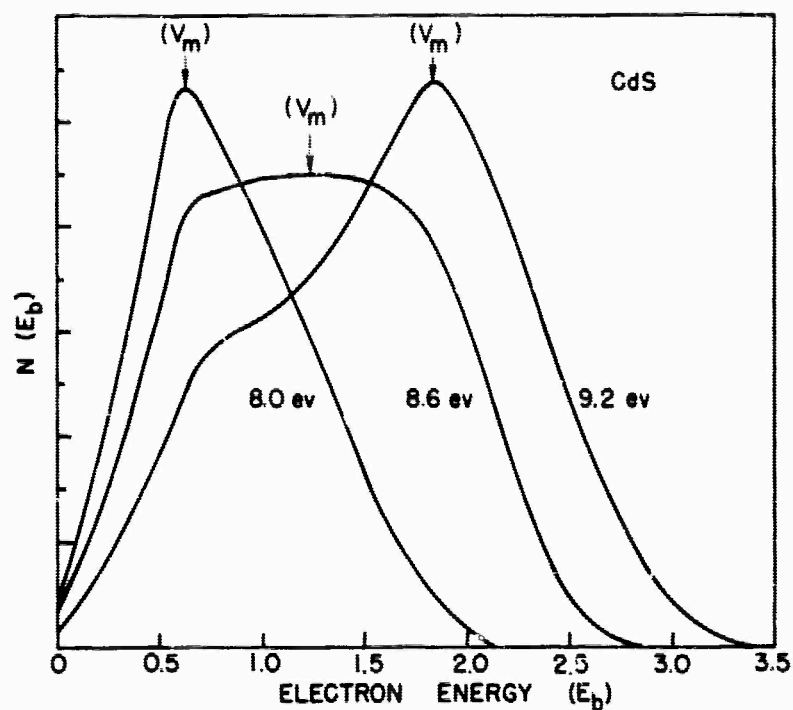
5. CdS Sealed Tubes (T)

Previously reported photoemission measurements [Ref. 57] used to determine the band structure of CdS were made on samples mounted in sealed phototubes. The results agree substantially with the results reported here. Minor differences appear in the absolute energy level of peaks. The curves differ in shape from the equivalent VC and LVC curves as a result of the change in electron affinity and a difference in impurity scattering (see Chapter V). Some of the energy distributions are shown in Fig. 47a and 47b.

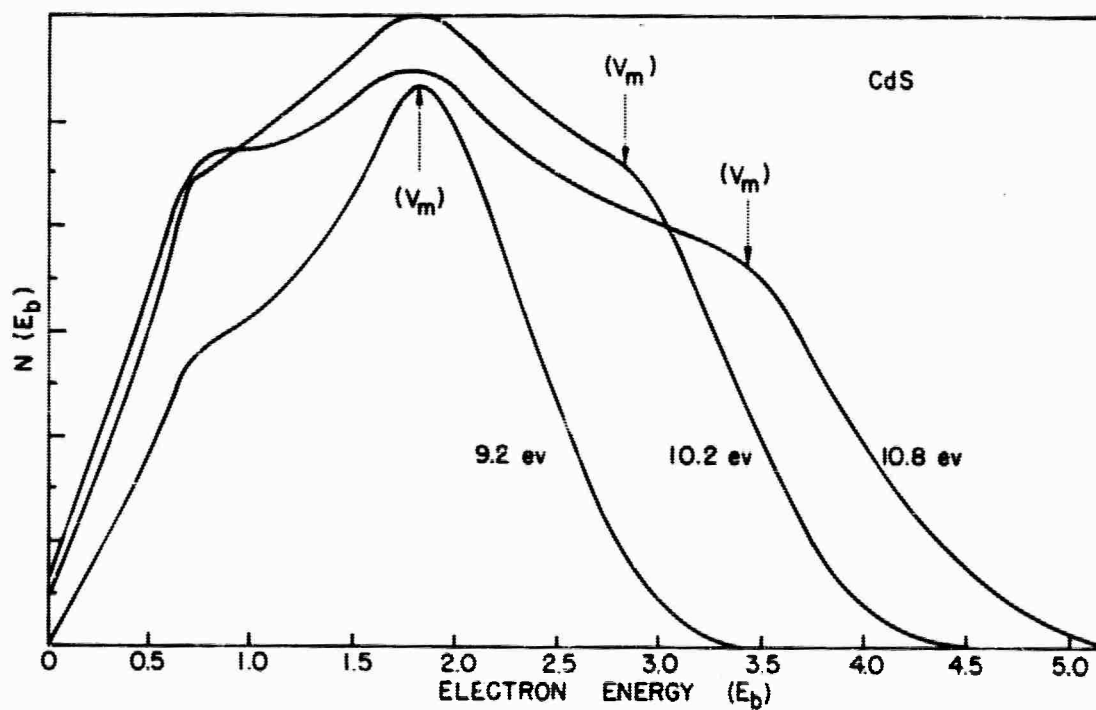
6. Air-Cleaved (AC) CdS

Detailed information about band structure was not obtained from the results of photoemission measurements on air cleaved CdS tested in low vacuum. The distortion in the energy distribution curves which obscured details is attributed primarily to impurity scattering. Band bending may be a contributing factor, although its effects are expected to be small due to the small optical absorption length. The results of these measurements are included in Chapter V.

BLANK PAGE



a. $h\nu = 8.0, 8.6, \text{ and } 9.2 \text{ eV.}$



b. $h\nu = 9.2, 10.2, \text{ and } 10.8 \text{ eV.}$

FIG. 47. ENERGY DISTRIBUTIONS FROM THE CdS PHOTOTUBE.

C. THE MEASURED BAND STRUCTURE OF CdS COMPARED WITH REFLECTION DATA

Although the absolute energy of maxima in the conduction and valence band densities of states of CdS can be determined from photoemission measurements, excitation to energy levels lying below the vacuum level cannot be measured directly. Reflection or optical absorption data can be used to determine the separation between coupled energy levels. Coupling to energy levels below the vacuum level can be directly observed only in reflection or absorption since the excited electrons cannot escape into vacuum. By comparing both types of data, a general understanding of the band structure can be obtained.

Optical conductivity is related to absorption by the expression

$$\sigma = \omega \epsilon_0 \eta k \quad (64)$$

in which $\omega/2\pi$ is the frequency of the incident radiation, η is the real part of the index of refraction and $k = \alpha\lambda/4\pi$ represents the absorption. The reflection is related to η and k by the relation

$$R = \frac{\eta^2 + k^2 - 1}{\eta^2 + k^2 + 1} \quad (65)$$

From Eq. (64) it can be seen that a peak in conductivity causes a peak in absorption through k . A peak in k has a larger effect on the numerator than on the denominator of Eq. (65). Therefore, a peak in absorption will cause a peak in reflection in the first order approximation. In the range

of photon energies of interest both η and k have values of the order of unity. The Kramers-Krönig analysis can be used to determine η and k from reflection data if they are known over a wide range of photon energies.

Figure 48 shows the energy levels of maxima in the density of states (solid lines) determined directly from photoemission measurements on vacuum cleaved CdS. Peaks in the reflection should occur when $h\nu$ is equal to the energy difference between density of states maxima and the valence and conduction bands. On this basis, peaks in reflection at 7.9 and 9.4 eV have been predicted. Figure 49 shows reflection data of Walker and Osantowski [Ref. 7] and of Cardona [Ref. 5]. Arrows indicate the energy levels at which these peaks were predicted from the photoemission data. The combined use of photoemission and reflection data makes it possible to establish the absolute energy level of additional structure in the density of states. The peak in reflection at 5.6 eV is associated with transitions from the valence band at -1.2 eV. The corresponding conduction band state is at 4.4 eV. The three peaks in reflection at high photon energies are separated in energy by about the same amount as the three peaks at lower photon energies. This can be explained in terms of a second maximum in the valence band density of states located at -9.4 eV with respect to the top of the valence band. These peaks are shown by dotted lines in Fig. 48.

Comprehensive photoemission data on CdS establish the density of states as follows. Valence band peaks are located

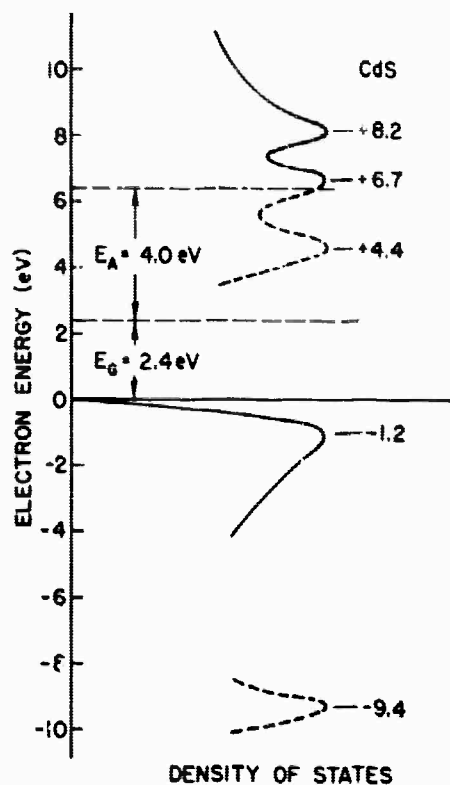


FIG. 48. ENERGY LEVELS OF MAXIMA IN THE CdS DENSITY OF STATES.

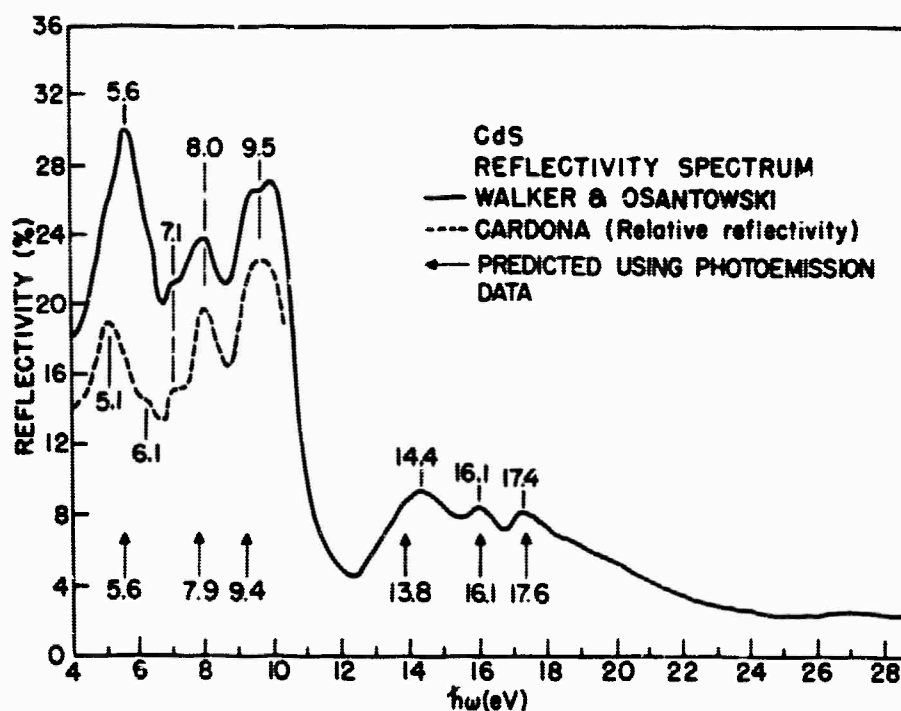


FIG. 49. REFLECTION AS A FUNCTION OF PHOTON ENERGY (WALKER AND OSANTOWSKI). The arrows indicate peaks in reflection predicted using the results of photoemission measurements.

at -1.2 and -9.4 eV referred to the valence band maximum. Conduction band peaks are located at 6.7 and 8.2 eV referred to the same level. The location of the conduction band peak at 4.4 eV is established using both photoemission and reflection data. As will be shown later, additional evidence for the location and strength of this peak can be obtained from the yield curve and from consideration of scattering of energetic electrons. The six peaks predicted using photoemission and reflection data are indicated by arrows in Fig. 49.

D. THE CALCULATED BAND STRUCTURE OF CdS

The band structures of CdS and ZnS have been calculated by Herman and Skillman [Ref. 14] who used an OPW method without considering spin-orbit splitting. The results for ZnS are shown in Fig. 50. (The CdS results were very similar so that they were not published [Ref. 53].) Even though these band structure calculations were preliminary, considerable reliance can be placed on general features. The calculations indicated three flat bands which were located approximately 2, 6, and 10 eV above the conduction band minimum, and narrow valence bands with a maximum density of states occurring about 2 and 8 eV below the valence band edge. The features of the band structure found in this work are in general agreement with the calculated band structure.

E. DETAILS OF THE DENSITY OF STATES OF CdS

The density of states of CdS has been determined by using

the methods of Chapter IIID, and by assuming that direct conservation of \bar{k} vector is not an important selection rule. Because of the assumptions, the results should only be considered as a first approximation to the actual density of states. The method does not explicitly include the effects of inelastic scattering, loss of resolution or of direct transitions. It may be possible to detect these phenomena as a result of inconsistencies in the density of states derived from different portions of the data.

The best evidence concerning the magnitudes of the densities of states is obtained from the results on high-vacuum-cleaved CdS. The energy distribution curves (VC) were measured at photon energy intervals of 0.2 eV. The method described in Eqs. (30) and (31) has been used to determine the conduction band density of states with the threshold function included, and the valence band density of states. The unknown ratio K_B/K_A in Eq. (31) is determined by normalizing the energy distributions to yield, and so depends on the uncertainty in yield. The ratio has a value close to one. Since it is a multiplying factor for the ratio of state densities separated by energy ΔE , the ratio of state densities separated by $n\Delta E$ will include the factor $(K_B/K_A)^n$. Only one conduction band peak can be observed directly in the VC curves. Two conduction band peaks can be seen in the LVC curves and their relative amplitudes can be estimated from this data since scattering does not appear to be important in the range of final energies

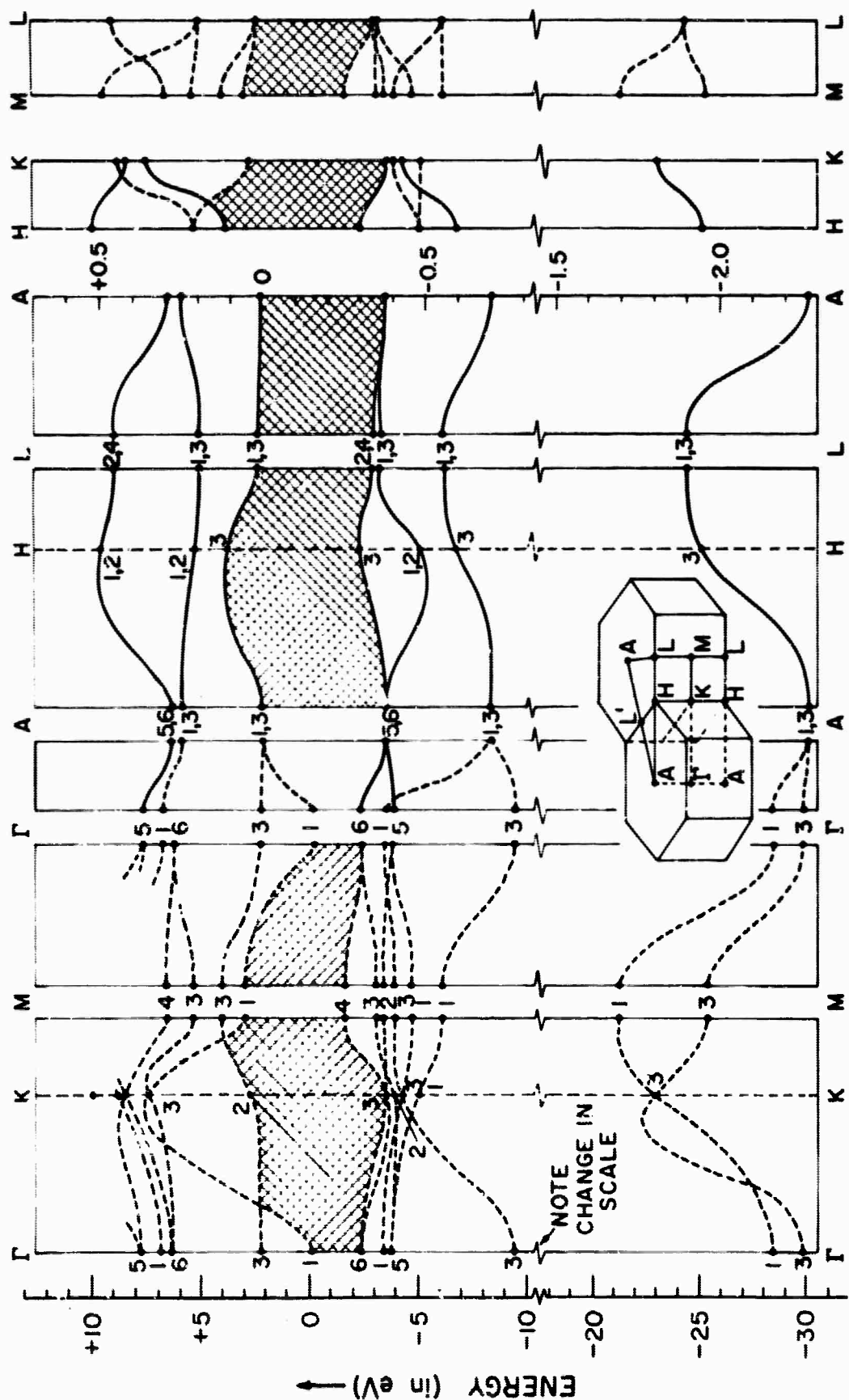


FIG. 50. THE CALCULATED BAND STRUCTURE OF ZnS (HERMAN AND SKILLMAN).
The calculated band structure of CdS is very similar.

at which they appear (to $E \approx 9$ eV). The details of the conduction band peak located below the vacuum level are determined indirectly from yield and optical conductivity. The density of states derived for CdS is shown in Fig. 51.

The maxima in the density of states used to calculate yield and optical conductivity might be expected to be sharper than those calculated directly from the energy distributions. The broadening of peaks in the energy distribution can be caused by several factors. Optical or acoustical phonon scattering can contribute [Refs. 42 and 59]. As shown in Chapter III E, band bending can cause broadening of structure. A small amount of broadening estimated to be between 0.1 and 0.2 eV is caused by resolution of the measurements. The resolution is determined by the bandwidth of the incident photon radiation, by the amplitude of the electrical signals used for measuring the energy distribution and by the details of the collector system. The sharpened density of states used to calculate all of the properties except the energy distributions is also shown in Fig. 51. The peaks appear at the same location as before but with different amplitudes. To first order, the area under the two density of states curves has been held constant.

Equation (32) and its equivalent for the conduction band have been used to check the consistency of the assumption of nondirect transitions by determining the shape of the valence band peak at -1.2 eV and of the conduction band peak at +5.2 eV as the photon energy is changed. The criterion

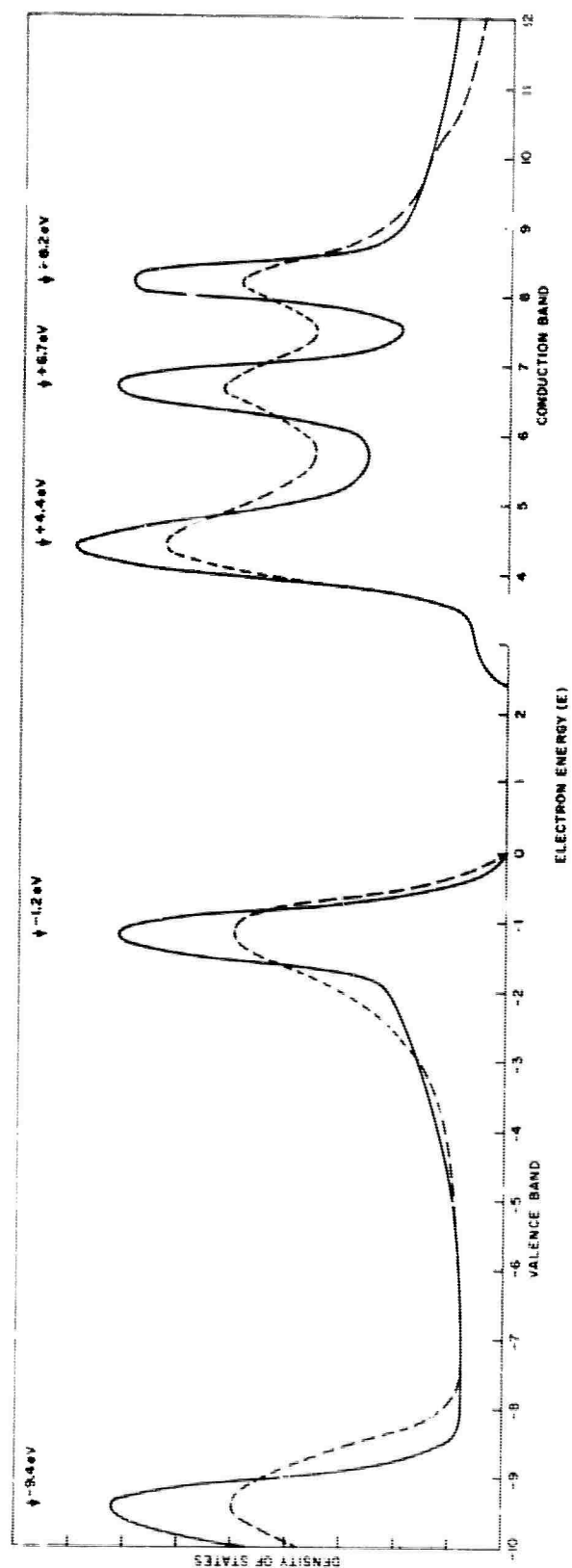
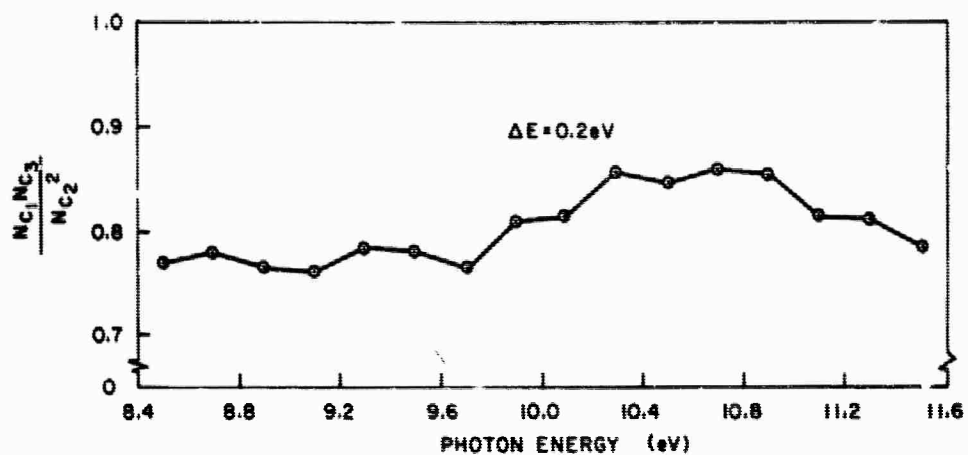


FIG. 51. THE DENSITY OF STATES OF CdS. The solid curve is a sharpened density of states.

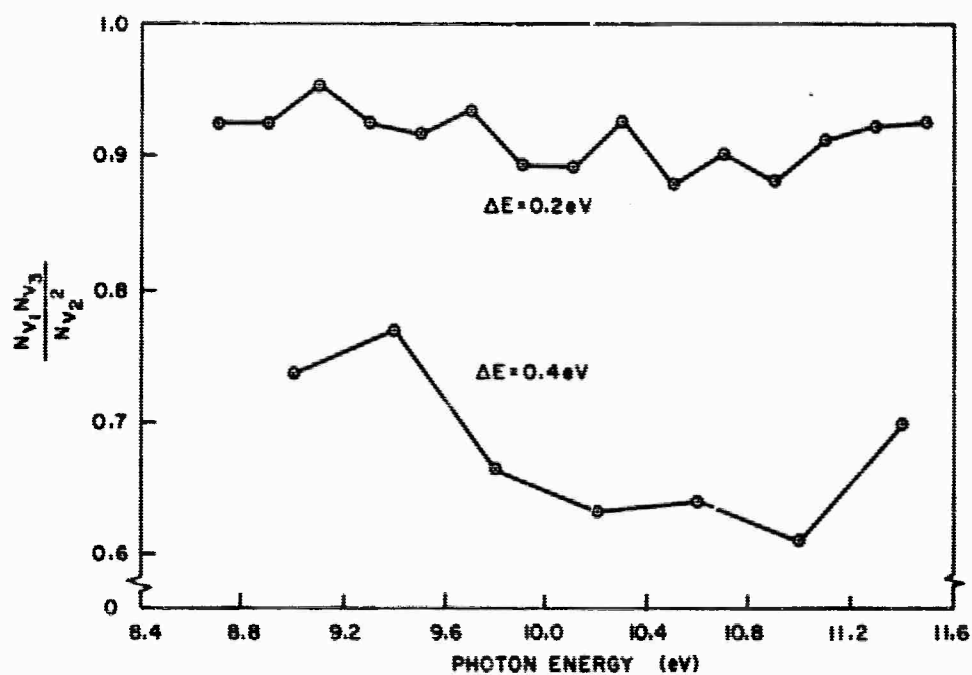
for consistency is that the ratios should be constant for all photon energies. The ratios are plotted in Fig. 52a. The ratios of the form $N_{c_1} N_{c_3} / N_{c_2}^2$ have been plotted versus photon energy for the 8.2 eV conduction band peak. For photon energies from 8.5 to 9.7 eV, the ratio has a nearly constant value of about 0.77. Above 7.9 eV it rises to about 0.85 indicating approximately a 50% broadening of the peak. The ratio then drops back to around 0.8 at 11.5 eV. The ratio $N_{v_1} N_{v_3} / N_{v_2}^2$ has also been plotted in Fig. 52b for the valence band peak at -1.2 eV, using energy distributions separated by 0.2 eV and by 0.4 eV. The 0.2 eV ratios are close to 1.0 indicating a wide peak. The 0.4 eV ratios start at about 0.75 and drop to about 0.65 at high photon energies. This indicates a moderate decrease in peak width for higher photon energies. Some of the fluctuations in the curves can be attributed to the change in background due to inelastic scattering. Changing matrix elements or direct transitions could also be responsible for some of the fluctuations.

F. OPTICAL CONDUCTIVITY ($\omega\epsilon_2$) OF CdS

The optical conductivity of CdS has been calculated by assuming constant matrix elements independent of initial and final electron energy. Equation (20) can then be integrated over energy E. The procedure is illustrated graphically in Fig. 53. The valence band density of states function is shifted with respect to the conduction band function by an energy equal to the photon energy. The area under the curve $N_c N_v$ divided



a. Conduction band-- $E = 8.2 \text{ eV}$



b. Valence band-- $E = -1.2 \text{ eV}$

FIG. 52. RATIOS DETERMINING THE SHAPE OF PEAKS IN THE CdS DENSITY OF STATES AS A FUNCTION OF PHOTON ENERGY.

by the photon energy is proportional to the optical conductivity in this approximation. The optical conductivity calculated from the derived and from the sharpened density of states is compared in Fig. 54 with the conductivity calculated by Walker and Osantowski from reflection data.

The general agreement between the optical conductivities indicates the correctness of the gross features of the density of states function determined from photoemission data and of the assumption of nondirect transitions and constant matrix elements. Further agreement is obtained in the comparison of measured and calculated yield and energy distribution curves in the following sections.

G. THE QUANTUM YIELD

1. Measured Yield

The quantum yield for high-vacuum-cleaved CdS is plotted as a function of photon energy in Fig. 55. The upper yield curve is corrected for LiF transmission and for reflection. A yield curve for the low-vacuum-cleaved (LVC) CdS is shown in Fig. 56. The calculated curve shown in Fig. 56 is discussed later. Yield curves for the other types of surfaces are presented in Chapter V. The yield rises exponentially in the threshold region to a quantum efficiency of approximately 0.1 electrons/photon. For larger $h\nu$, the yield increases very slowly, reaching a broad maximum around 12.0 eV. At 13 eV the yield drops rapidly reaching a minimum at about 15 eV. At 16.8 eV the yield has increased to a value of about

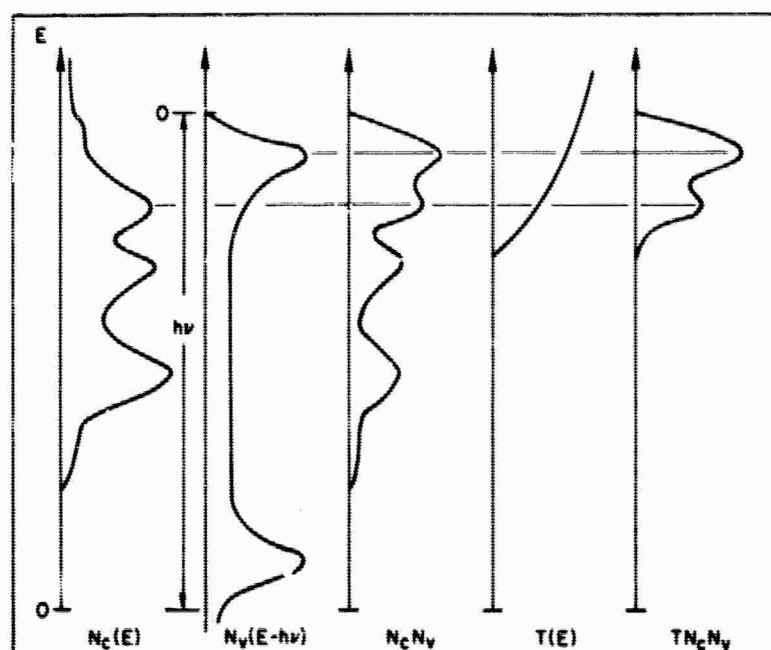


FIG. 53. GRAPHICAL ILLUSTRATION OF THE PROCEDURE FOR CALCULATING OPTICAL CONDUCTIVITY, YIELD AND ENERGY DISTRIBUTIONS FROM THE DENSITY OF STATES.

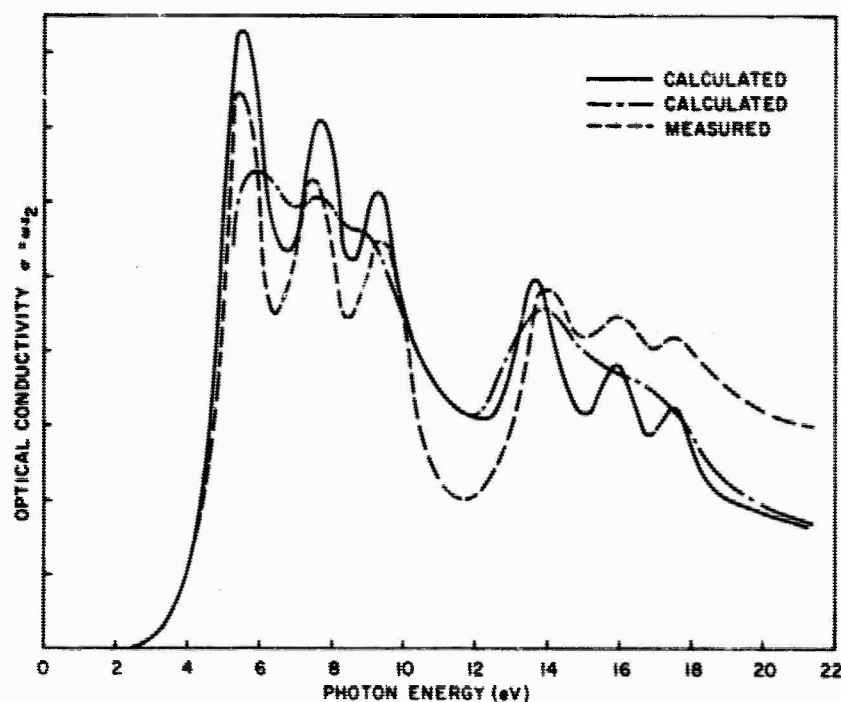


FIG. 54. COMPARISON OF THE MEASURED AND THE CALCULATED OPTICAL CONDUCTIVITY ($\omega\epsilon_2$) OF CdS. The solid curve is calculated from the sharpened density of states.

0.5 electrons/photon. At 21.2 eV the yield is somewhat smaller.

Some of the details of the yield curves can be interpreted by the use of Eq. (14) in which the term $[1 + 1/\alpha L]^{-1}$ is assumed to be constant. From Eq. (20) the absorption above and below the vacuum level is given by

$$\alpha_a = \int_{E_G + E_A}^{h\nu} \alpha'(E) dE \quad \text{and} \quad \alpha_b = \int_{E_G}^{E_G + E_A} \alpha'(E) dE$$

respectively. If reflection is neglected and a step threshold function is assumed, the quantum yield is given approximately by

$$Y \approx \frac{\alpha_a}{\alpha_a + \alpha_b} \quad (66)$$

as shown by Spicer [Refs. 42, 59, and 60]. The inflection in the yield curves at about 7.9 and 9.4 eV can be understood by reference to Eq. (58). The term α_a becomes large at photon energies which produce coupling between a high density of initial states and a high density of final states above the vacuum level. That this coupling occurs near 7.9 and 9.4 eV will be shown in Sec. G2. Since this term is a larger fraction of the numerator than of the denominator, it will tend to cause a peak in yield. The inflection at 8.5 eV is not understood. The prominence of this peak depends on the history of the surface.

The structure in the yield curve of Fig. 56 at photon

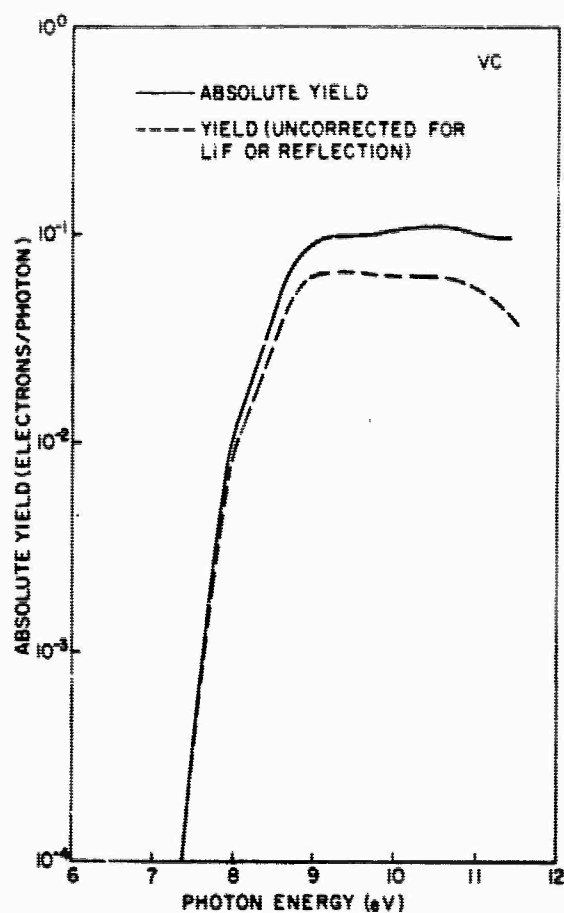


FIG. 55. THE MEASURED ABSOLUTE QUANTUM YIELD OF HIGH-VACUUM-CLEAVED CdS.

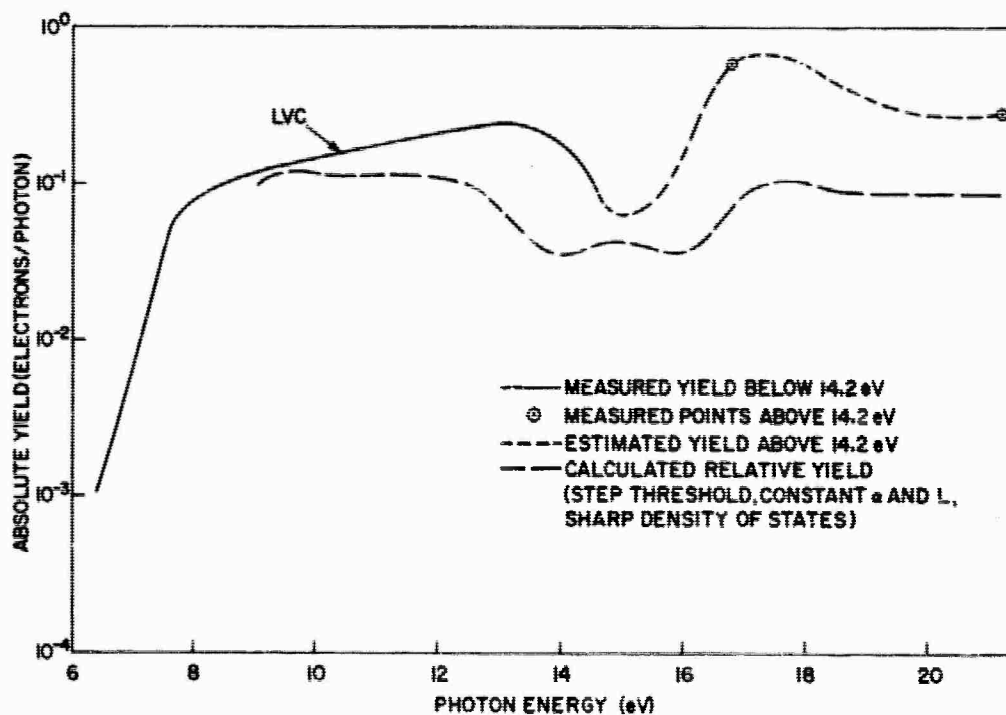


FIG. 56. THE MEASURED ABSOLUTE QUANTUM YIELD OF LOW-VACUUM-CLEAVED CdS. Comparison with the relative yield calculated from the density of states.

energies beyond the cutoff of LiF (11.6 eV) can be attributed to two different effects. The dip in the curves starting at about 13 eV is caused primarily by the strong absorption between a deep valence band peak (-9.4 eV) and a final conduction band state below the vacuum level. This absorption causes the term α_b in the denominator of Eq. (58) to increase and produce a corresponding decrease in yield. Electron scattering is also important at these photon energies and can contribute to the reduction in yield. The maximum in yield which occurs near 16.8 eV is attributed to the strong absorption to final states above the vacuum level due to coupling from the -9.4 eV valence band peak (an increase in α_a). The escape of secondary electrons resulting from pair production also contributes to the yield in this region.

The electron affinity of CdS is found to be 4.8 ± 0.3 eV for low-vacuum-cleaved (LVC) samples. The electron affinity for the low-vacuum-cleaved sample is difficult to determine because a portion of the yield in the threshold region may occur from occupied surface states above the valence band. Scheer and van Laar [Ref. 45] and Spicer [Ref. 55] have discussed the effect of surface states in detail.

All of the yield curves which were measured show exponential dependence in the threshold region. Redfield [Ref. 61] and Dexter [Ref. 62] have discussed reasons for the exponential dependence of the absorption edge. This could contribute to the exponential dependence of the quantum

yield near the threshold in photoemission from CdS. Band bending may also produce exponential dependence as can be seen from the bending distribution functions in Eqs. (43) and (48).

The shape of the calculated yield curve in the threshold region depends primarily on the shape of the valence band density of states near the band edge and on the threshold function. A wide range of power law curves or an exponential yield curve can be predicted theoretically depending on the assumptions made [Refs. 42, 60, and 63]. The conduction band will have a smaller effect on the yield curve near the threshold unless the threshold occurs near strong structure in the conduction band density of states.

2. Calculated Yield Curves

The yield is calculated by the use of Eq. (14) with the assumption that inelastically scattered electrons are lost from the energy distribution. For the calculations in this section the term $[1 + 1/\alpha(h\nu)L(E)]$ is assumed to be a constant independent of E and $h\nu$. The reflection is neglected since the measured yield curves have been corrected for reflection. Calculations are made either with a step threshold function or with the threshold function given by Eq. (22). The energy associated with the critical momentum in Eq. (22) is arbitrarily assumed to be 0.8 eV. This low value is chosen because photoemission near the threshold is expected to occur from relatively narrow bands as can be seen from the band structure diagram

in Fig. 50. In addition, the effects of elastic scattering may make the threshold function rise more rapidly than predicted by the Fowler theory. The method of calculating yield is illustrated in Fig. 53. The absolute yield per absorbed photon is obtained under the above assumptions by dividing the area under the $TN_c N_v$ curve by the area under the $N_c N_v$ curve.

The calculated yield is plotted in Fig. 57 for comparison with the VC curve. Both types of threshold function and both the derived and sharpened densities of states have been used. The corresponding curves for α_a and α_b are shown in Figs. 58a and 58b for the derived and for the sharpened density of states, respectively. The step threshold function gives the best approximation to the shape of the yield curve. The resulting absolute yield, however, is too large by a factor of 2 at high photon energies. The assumed Fowler type threshold function gives the correct yield at high photon energies but gives too low a yield in the threshold region. The structure at about 7.9 and 9.4 eV is somewhat more apparent for the sharpened density of states.

An estimate of the attenuation length $L(E)$ can be made from the above calculations by using the absorption length obtained from reflection data [Ref. 7] shown in Fig. 59. In the worst case, for an absorption length of 100 \AA , an attenuation length of 100 \AA would be required to compensate for the approximate factor of 2 discrepancy between the yield calculated with a step threshold and the measured yield. If the threshold

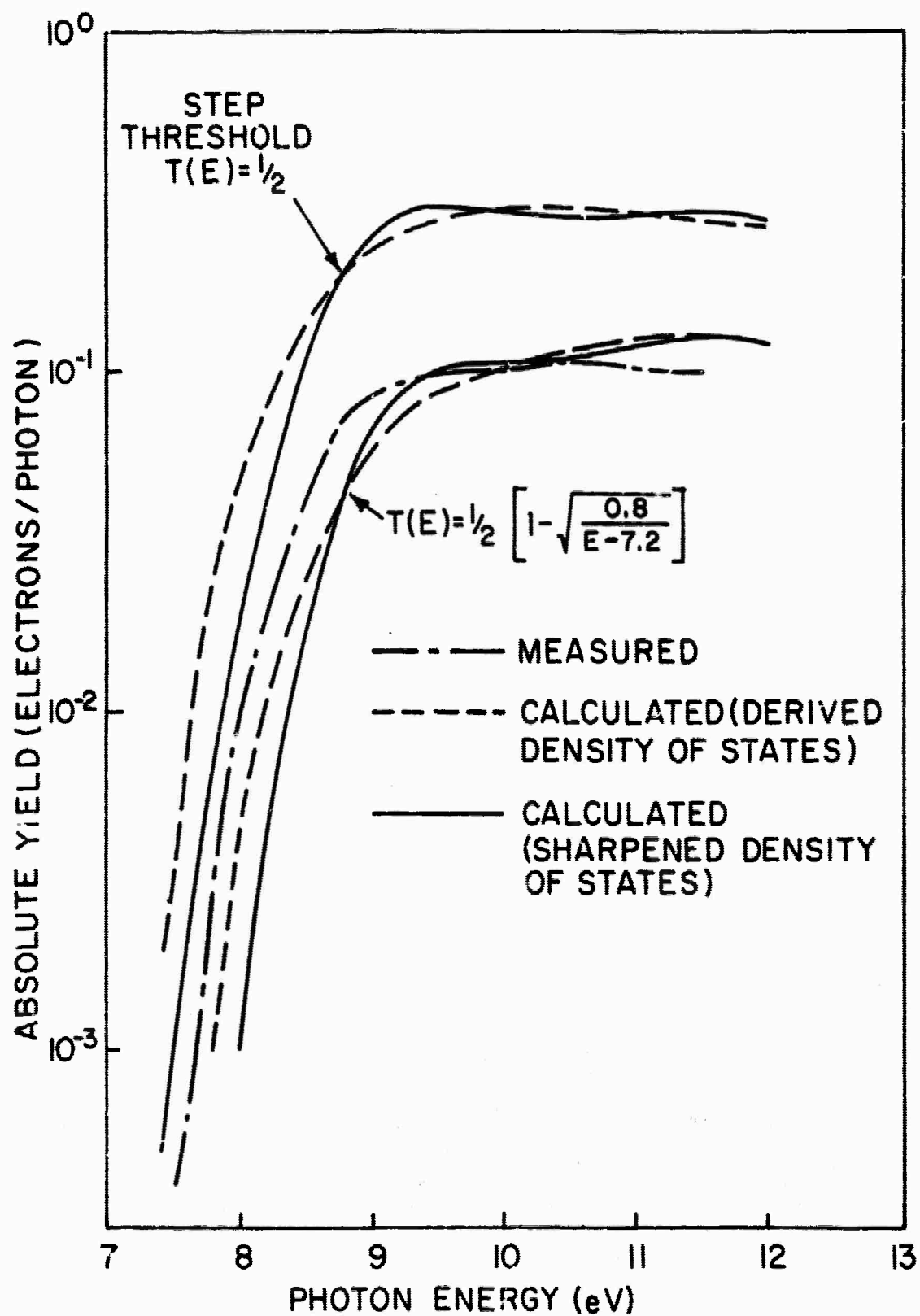
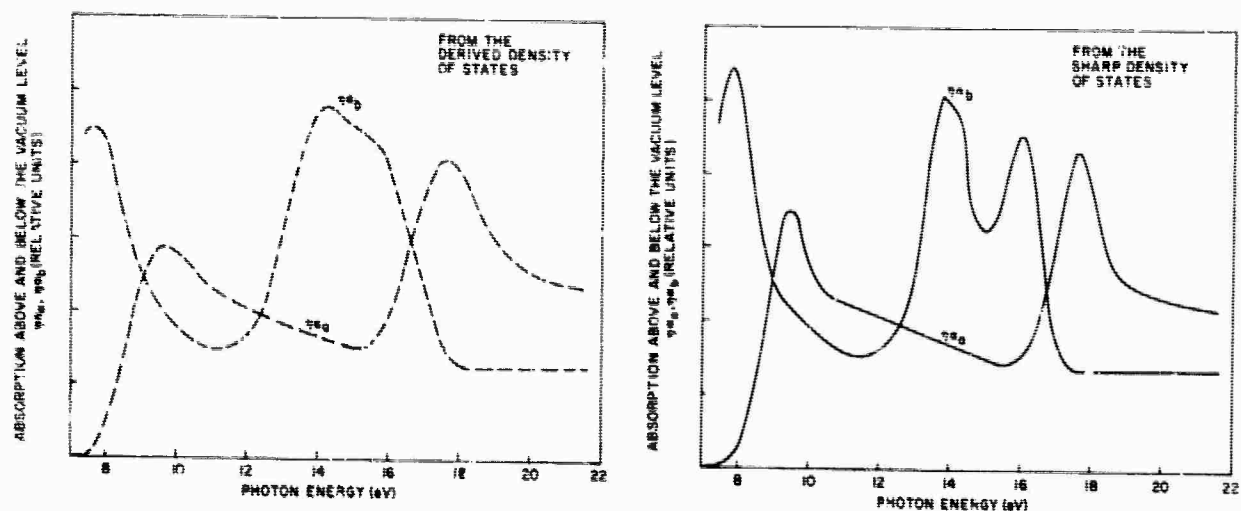


FIG. 57. COMPARISON OF THE MEASURED AND CALCULATED ABSOLUTE YIELD OF CdS.



a. From the derived density of states

b. From the sharpened density of states

FIG. 58. CALCULATED ABSORPTION ABOVE AND BELOW THE VACUUM LEVEL.

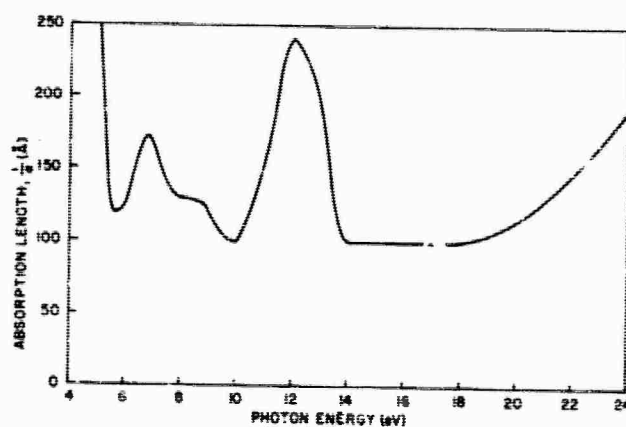


FIG. 59. THE ABSORPTION LENGTH $1/\alpha$ IN CdS AS A FUNCTION OF PHOTON ENERGY. (From reflection data of Walker and Osantowski.)

function reduces the yield by an additional factor of 2 over the step threshold function, then the required value of $L(E)$ would be large compared to an absorption length.

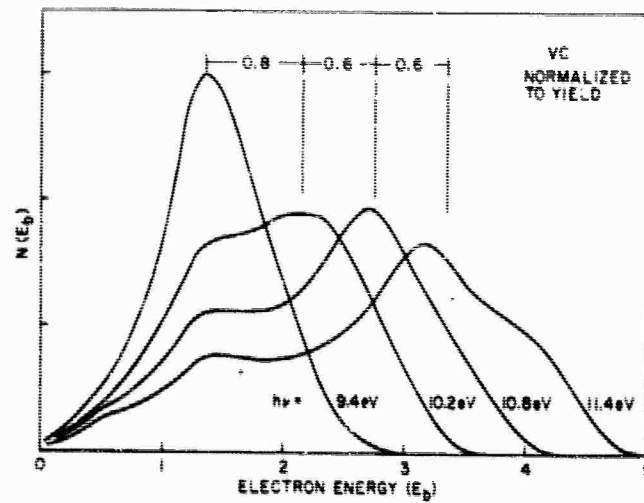
The calculated relative quantum yield out to 21.2 eV is shown in Fig. 56. The absolute value has been adjusted for easy visual comparison. From this curve it can be seen that optical excitation to final quantum states above the vacuum level decreases above photon energies of $h\nu = 13$ eV and increases near $h\nu = 16.8$ eV in qualitative agreement with the measured yield curves. The small hump in the calculated curve at $h\nu = 15$ eV is caused by a corresponding dip in α_p . This is not present if the derived density of states is used. This calculation does not include the effects of inelastic scattering or pair production which are important factors in this range of photon energies. The apparent disagreement may be due to this exclusion. Since only two widely spaced, measured values of yield are available above $h\nu = 14.2$ eV, only a qualitative comparison can be made between the calculated and the measured curve in this range.

The general agreement between the calculated and the measured yield combined with the agreement in calculated and measured conductivity in Sec. F indicates that the calculated density of states represents a good first approximation. Since the detailed nature of the threshold function is not known, considerable uncertainty is introduced into the calculations. The lack of detailed consideration of inelastic

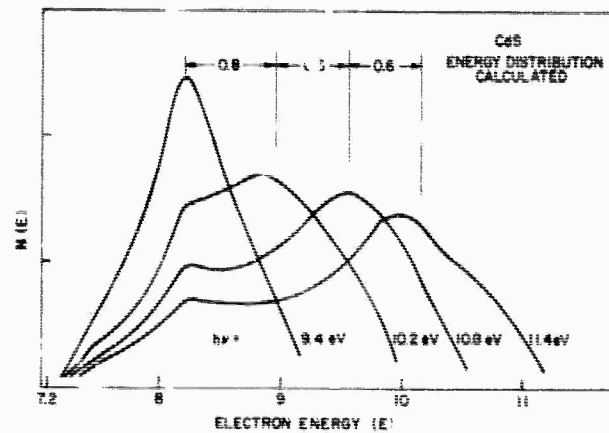
scattering in the calculated yield curve introduces an additional uncertainty into the calculations.

H. THE ENERGY DISTRIBUTION OF PHOTOEMITTED ELECTRONS

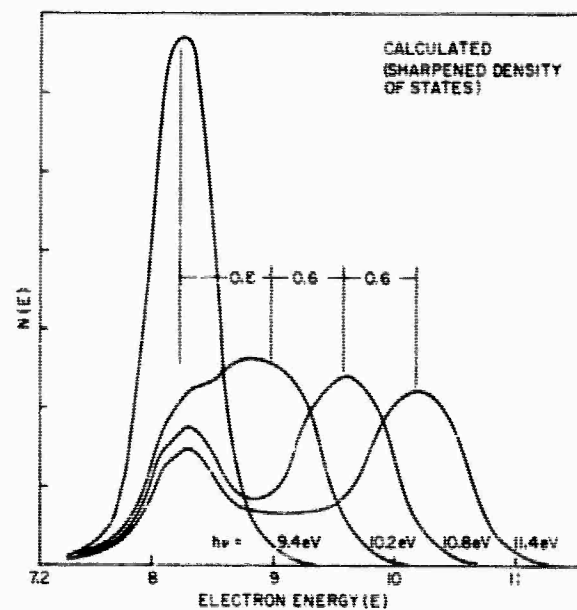
The CdS density of states shown in Fig. 51 has been used to calculate the energy distributions at 9.4, 10.2, 10.8, and 11.4 eV. The results for both the derived and the sharpened densities of states are compared with the energy distributions for vacuum cleaved samples in Fig. 60. It is not surprising that the density of states derived from one pair of energy distribution curves should reproduce the energy distributions from which it was derived. However, the requirement that the density of states so derived must reproduce energy distributions of the correct shape at all other photon energies is more stringent. The strictest requirement is that the area under the calculated energy distribution curve divided by the measured yield should be constant at all photon energies. This is equivalent to normalizing the measured curves to yield assuming α is constant. The good agreement over a wide range of photon energies supports the assumption of nondirect transitions and indicates that the assumption of constant matrix elements is a good approximation. The required sharpening of the density of states to obtain better agreement with yield and optical conductivity, although not understood in detail, is reasonable since all of the effects listed in Sec. E would tend to broaden the distributions.



(a)



(b)



(c)

FIG. 60. COMPARISON OF MEASURED AND CALCULATED ENERGY DISTRIBUTIONS. (a) Measured energy distribution normalized to yield. (b) Calculated energy distribution (derived density of states). (c) Calculated energy distribution (sharpened density of states).

I. THE EFFECTS OF SCATTERING

1. General Discussion of Effects

Several effects of scattering by pair production can be seen in the LVC energy distributions (Figs. 41-46). A peak occurs at the high energy end of the distribution due to electrons excited from the valence band peak at $E = -1.2$ eV. This peak steadily diminishes in size for increasing photon energy due to inelastic scattering of electrons. The scattered electrons appear at lower energy levels causing a large peak in the energy distribution near $E_p = 0.9$ eV. In addition, a shoulder appears in the energy distributions for $h\nu = 16.8$ and 21.2 eV. This shoulder starts to rise at an energy about 3.0 eV below that of the most energetic electrons regardless of the photon energy. It reaches a plateau at about 6.0 eV below the maximum electron energy. In the energy distributions for the high-vacuum-cleaved CdS, the notch in the peak associated with excitation from the valence band for photon energies about 10.8 eV may be caused by inelastic scattering, although it can also be explained by a dip in the density of states at $E = 10.0$ eV or by a direct transition.

In the following paragraphs, these phenomena are explained on a qualitative basis. The calculations represent possible explanations of the relationship between the density of states and scattering phenomena. Both the loss of high energy electrons and the generation of lower energy electrons by one inelastic scattering event are considered. Multiple

scattering is certainly present but is not considered in detail here.

2. The Loss of High Energy Electrons Due to Scattering

The loss of high energy electrons in the energy distribution is estimated by using Eq. (56) given by

$$\left[1 + \frac{1}{\alpha(h\nu)L(E)}\right]^{-1} \quad (67)$$

The qualitative effects of this term can be estimated by making some approximation on $L(E)$. If the elastic scattering mean free path ℓ_p is assumed to be independent of energy, the attenuation length $L(E)$ can be determined graphically using the inelastic scattering mean free path as shown in Fig. 61. The relation between $L(E)$ and ℓ_e is obtained from the results of the Monte Carlo calculations [Ref. 53] or age theory [Ref. 52]. A typical value of the attenuation length $1/\alpha_0$ is indicated in the figure. At low electron energies where $\ell_e > \ell_p$, the relation between $L(E)$ and ℓ_e is complicated. However, in this energy range Eq. (67) will have an almost constant value near unity independent of fluctuations in $L(E)$. At energies where $L(E)$ and $1/\alpha$ become comparable, it may be assumed that $L(E)$ is almost a linear function of ℓ_e . If the scattering is based on a density of states argument assuming constant matrix elements, nondirect transitions (see Chapter IIIF), and constant electron velocities, then ℓ_e is inversely proportional to the integrated scattering probability $P_s(E')$ which is plotted for CdS in Fig. 62. Then Eq. (67) reduces to a form similar to

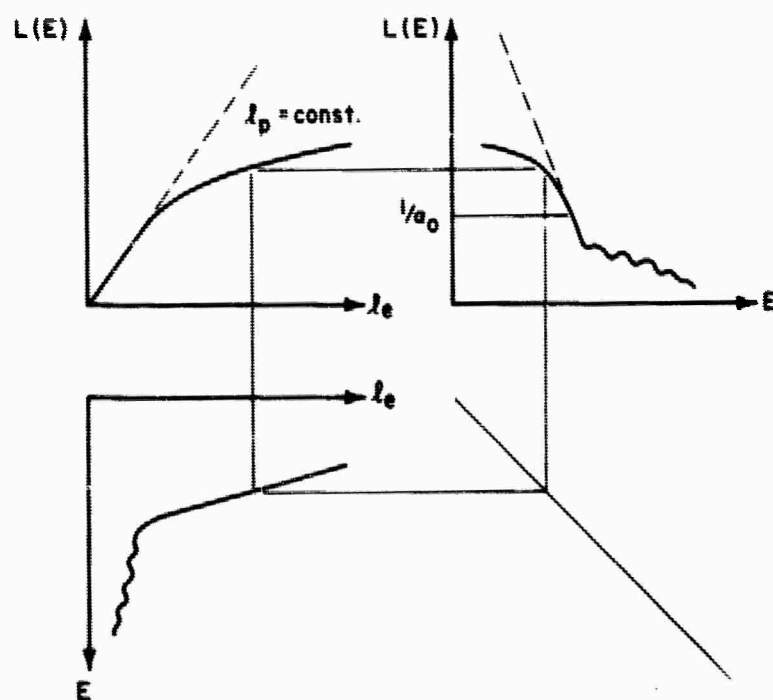


FIG. 61. GRAPHICAL RELATION BETWEEN THE ATTENUATION LENGTH $L(E)$, THE ELASTIC SCATTERING MEAN FREE PATH l_p , AND THE INELASTIC SCATTERING MEAN FREE PATH l_e .

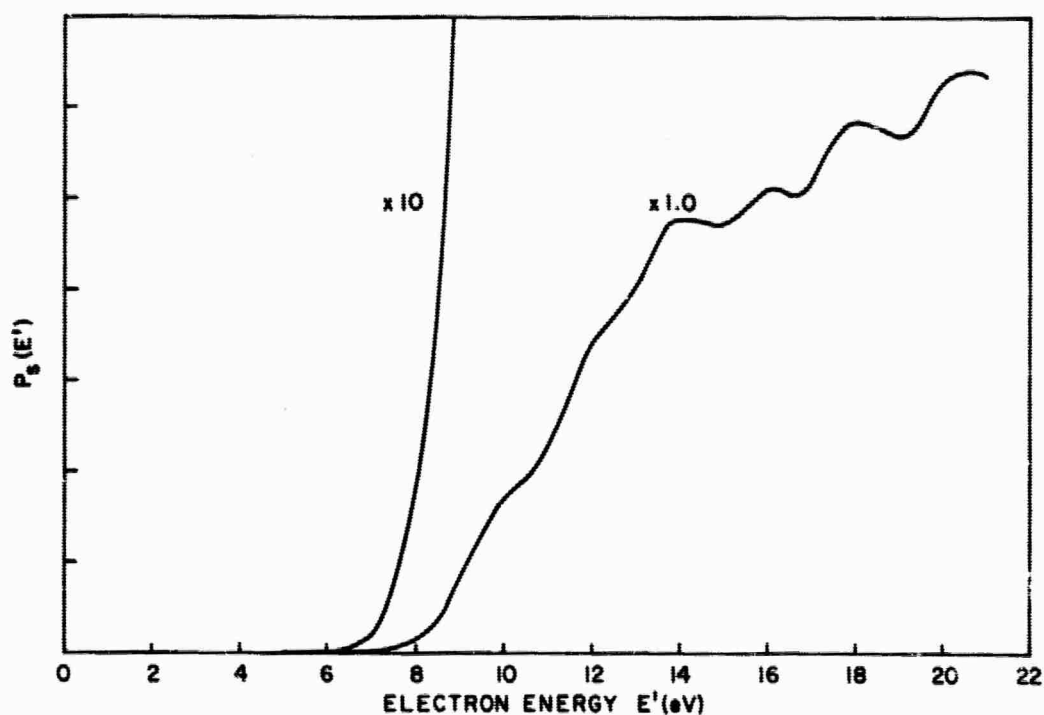


FIG. 62. THE INTEGRATED SCATTERING PROBABILITY FOR CdS.

Eq. (57):

$$\left[1 + \frac{K_5 P_s(E')}{\alpha(h\nu)} \right]^{-1} \quad (68)$$

in which K_5 is a constant chosen to give the correct value of ℓ_e at an energy where it is known. Even though the constant K_5 is not known for CdS, Eq. (68) can still be used to qualitatively indicate the effects of scattering. Eq. (68) is plotted in Fig. 63 as a function of E' assuming that K_5 is a constant and that α is a parameter. The values of α chosen are 1, 2, 4, 8, and 16 times an arbitrarily chosen reference value given by α_0 . As α decreases the correction factor dips to a value much smaller than unity at high electron energies. The variation of α as a function of photon energy is obtained from Fig. 59. Calculated energy distribution curves are plotted in Fig. 64a for a photon energy of 11.0 eV with and without the effect of scattering included. The curve marked $16\alpha_0$ in Fig. 63 has been used. At 11.6 eV, α has decreased roughly by a factor of 2 so that the curve marked $8\alpha_0$ in Fig. 63 must be used to correct the energy distribution for scattering. The results are shown in Fig. 64b. The increase in absorption length has caused the effects of scattering to be more apparent at the higher photon energy. A change in ℓ_p can cause a similar effect in energy distributions taken at the same photon energy on two differently prepared samples. This type of phenomenon is discussed in more detail in Chapter V.

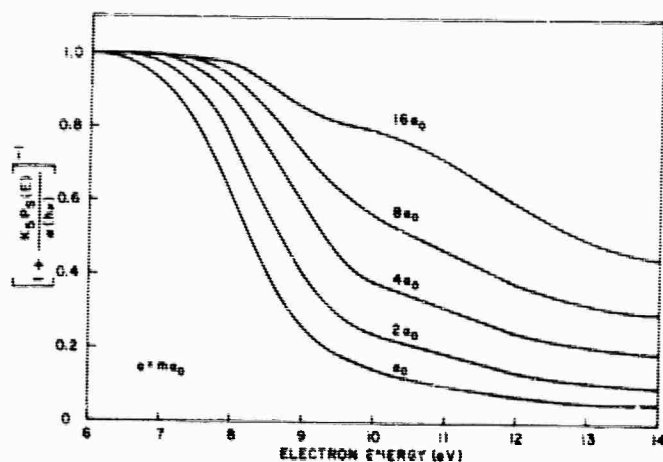
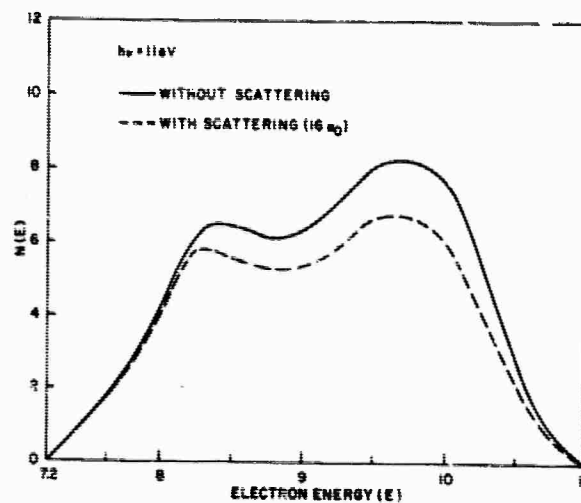
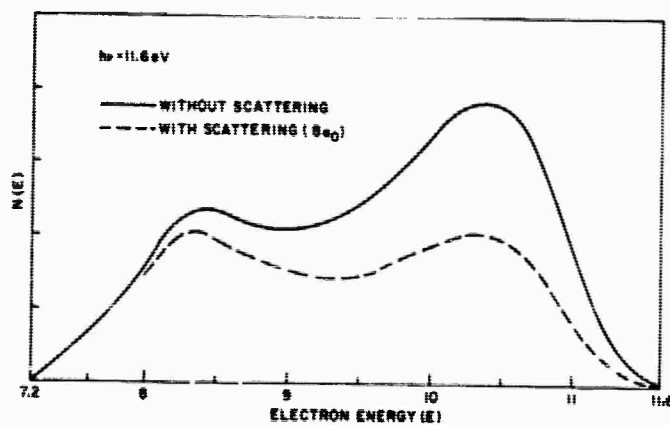


FIG. 63. GRAPHICAL ILLUSTRATION OF THE ATTENUATION OF HIGH ENERGY ELECTRONS DUE TO SCATTERING.



a. At 11 eV



b. At 11.6 eV.

FIG. 64. HYPOTHETICAL ILLUSTRATION OF THE EFFECT OF VARIATIONS IN ABSORPTION LENGTH ON THE CALCULATED ENERGY DISTRIBUTIONS.

3. The Energy Distribution of Once-Scattered Electrons

At high photon energies, scattered and secondary electrons may escape from the solid and appear in the energy distributions. The distribution of energies of these electrons may provide useful information about the relationship between the band structure and the scattering processes.

A qualitative estimate of the energy distribution of once-scattered electrons is made here using the theory developed by Berglund ([Ref. 32] and Chapter III F). The second term in the brackets of Eq. (55) reproduced here as Eq. (69) can be used to calculate an estimated energy distribution of once-scattered electrons in the solid

$$g(E) = 2 \int_E^{E+h\nu} \frac{p_s(E', E)}{P_s(E')} \alpha'(E') dE' \quad (69)$$

Several approximations can be made in Eq. (69) for scattering calculations in CdS at photon energies of 16.8 and 21.2 eV.

1) Optical excitation occurs from the valence band peak at $E = -1.2$ eV to final conduction band energies between about 19 and 21.2 eV where the conduction band density of states is nearly constant. Therefore, $\alpha'(E)$ is proportional to $N_v(E' - h\nu)$. 2) $P_s(E')$ is approximately constant over the same range of final energies, as can be seen in Fig. 62. 3) The conduction band density of states $N_c(E)$ is assumed to be constant over the range of final energies E to which electrons can scatter from E' . 4) Based on assumption 3) and the

assumption of scattering due to nondirect transitions, and constant matrix elements, the scattering probability in Eq. (52) is proportional to $(E'-E)\sigma(E'-E)$ [see Eq. (20)].

Using the above assumptions, Eq. (66) can be written as

$$g(E) \propto \int_E^{hv} N_V(E'-hv) \int_0^\infty N_V(E_0) N_C(E_0+E'-E) dE_0 dE' \quad \left. \begin{array}{l} \text{or} \\ \\ g(E) \propto \int_E^{hv} [N_V(E'-h\nu)](E'-E)[\sigma(E'-E)dE'] \end{array} \right\} \quad (70)$$

Energy distributions of once-scattered electrons calculated using Eq. (70) are compared in Fig. 65 with the measured energy distribution. The electron energy referred to the maximum possible energy is plotted as the abscissa. A shoulder in the measured curves which reaches a plateau near -6.5 eV is qualitatively predicted by the theory. The number of electrons losing an energy just larger than the band gap (arrow) in the measured curve is much larger than predicted by the theory. Part of the discrepancy may be caused by additional energy dependent factors in the matrix elements, and by the assumption of a constant final density of states.

Other evidence appears in the energy distributions to indicate that a measurable number of electrons lose an amount of energy just larger than the band gap. This can be seen by

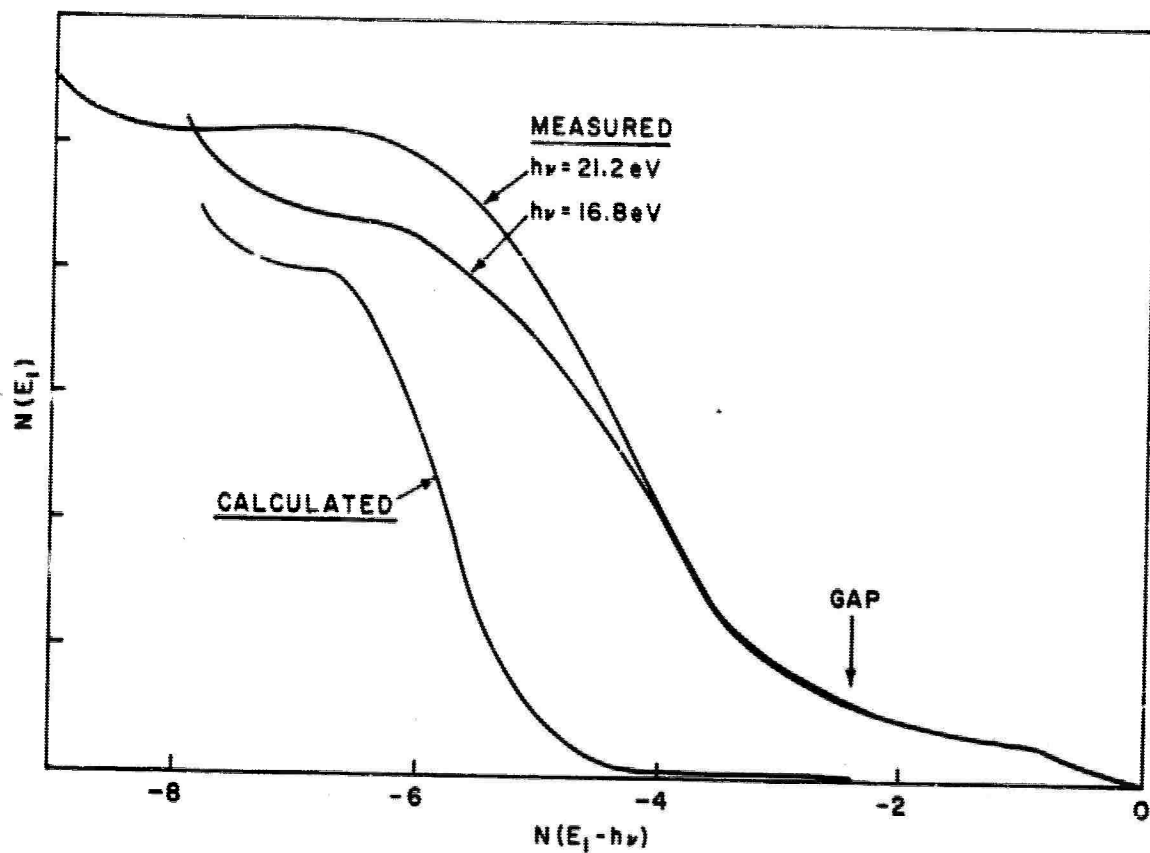


FIG. 65. MEASURED ENERGY DISTRIBUTIONS AT 16.8 AND 21.2 eV COMPARED WITH THE CALCULATED ENERGY DISTRIBUTION OF ONCE-SCATTERED ELECTRONS.

comparing the ratio of the magnitude of the peak at $E_b = 0.9$ eV to that of the peak at $E_b = 2.4$ eV in the LVC energy distributions (Figs. 43-46). This ratio is plotted in Fig. 66. The ratio increases for increasing photon energies up to $h\nu = 11.2$ eV. Then it dips through a rather sharp minimum at $h\nu = 12.2$ eV. From 14.0 eV, it rises gradually to a value of 2.5 at $h\nu = 21.2$ eV. The minimum occurs when the average energy of the excited valence band electrons is $E_b = 11.0$ eV. This indicates that a maximum in the energy distribution of scattered electrons occurs in this photon energy range for an energy loss of about 2.8 eV.

It may be possible to deduce information about the conduction band density of states below the vacuum level using the energy distribution of once-scattered electrons. For example, note that if the valence band peak were a delta function, the energy distribution of once-scattered electrons under the above assumptions would be a mirror image of the conduction band density of states as shown in Fig. 67. The high density of states at the top of the valence band of CdS roughly approximates the delta function.

In conclusion, the above calculations give possible explanations of features appearing in the energy distributions due to scattering. The failure to include multiply-scattered electrons, the lack of knowledge of the density of states at high energies, and the assumptions of constant matrix elements contribute to the lack of detailed agreement.

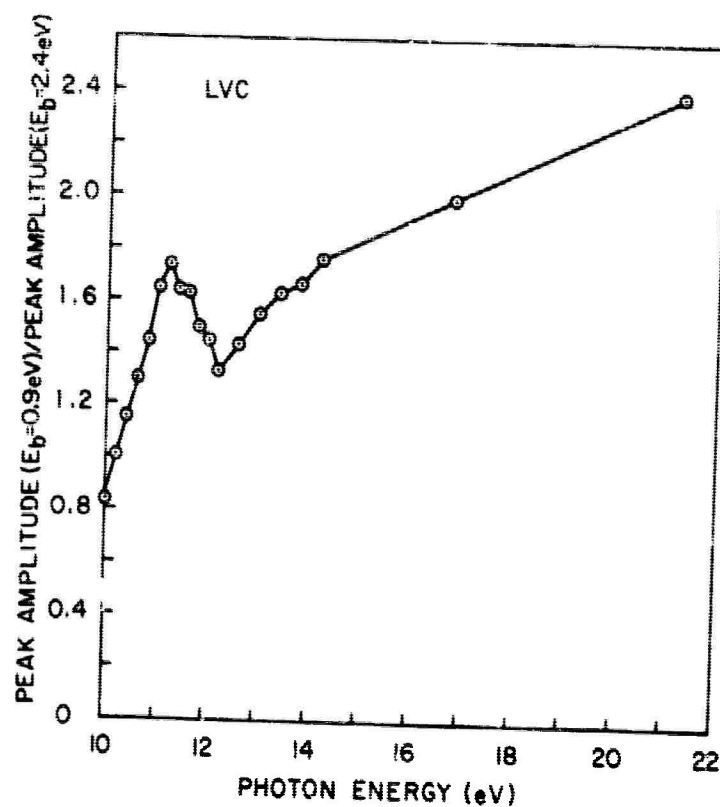


FIG. 66. THE RATIO OF PEAK HEIGHTS IN THE ENERGY DISTRIBUTIONS FOR LOW-VACUUM-CLEAVED CdS AT $E_b = 0.9$ AND 2.4 eV.

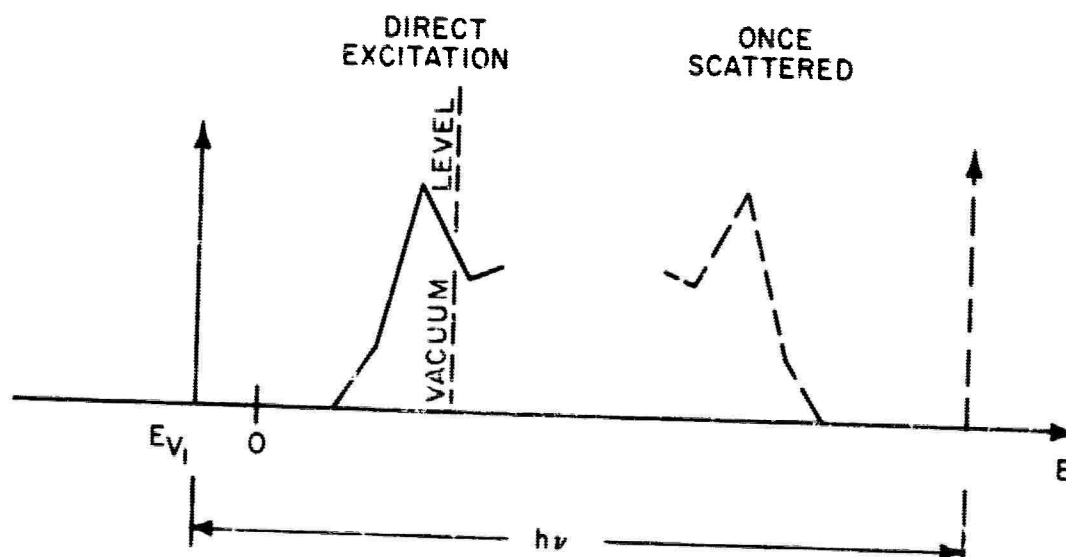


FIG. 67. HYPOTHETICAL ENERGY DISTRIBUTION OF ONCE-SCATTERED ELECTRONS.

V. EXPERIMENTAL RESULTS OF PHOTOEMISSION FROM CdS INTERPRETED IN TERMS OF SURFACE PROPERTIES

A. CONTROL OF SURFACE CONDITIONS

Use of the high vacuum test chamber and cleaving mechanism described in Chapter II has made it possible to prepare a fresh, uncontaminated CdS surface for study by photoemission. The resulting VC energy distribution and quantum yield measurements provide a standard of photoemission from the clean surface. The high-vacuum-cleaved VC sample can be exposed intentionally to controlled gaseous impurities and to other environmental factors such as heat and optical radiation. By this method it is possible to study the effect of surface treatment on photoemission and to simulate environmental conditions which are present when CdS surfaces are prepared by other than the VC method. The energy distribution curves taken after exposure are compared with those from the VC sample to study surface effects produced by the exposure.

The principle features of energy distributions which can be compared are 1) the energy separation between peaks, 2) the width of peaks, 3) the relative amplitudes of peaks or the slope of the curves in energy ranges where there are no peaks, 4) the electron affinity, and 5) the absolute energy E_p at which important features appear. In the following sections these features of the energy distributions as well as limited comparisons of the quantum yields are used to deduce information about the effects of CdS surface history on photoemission

processes.

B. EFFECTS OF EXPOSURE TO AIR - SIMULATION OF THE SEALED PHOTOTUBE

Energy distribution curves taken at a photon energy of 10.8 eV are compared in Fig. 68 for the following surfaces: high-vacuum-cleaved (VC); high-vacuum-cleaved sample exposed to air (VC-A); high-vacuum-cleaved sample exposed to air and baked (VC-B); air cleaved (AC); and surfaces cleaved in air, mounted in the phototube, and sealed (T). The relative energy scale on the abscissa was established by aligning the high energy end of the energy distribution curves. The estimated error in this process is ± 0.2 eV. The purpose of this set of experiments was to determine the effect of exposure to air on photoemission from CdS and to simulate the environmental conditions present during the preparation of the sealed phototubes. The phototubes provided an easy means of making initial measurements on CdS prior to the time that the high vacuum test chamber was available. They are of interest now primarily for the study of surface effects.

The VC sample was prepared and tested in high vacuum by the methods described in Chapter IIB3 and Chapter IID. The energy distribution of the VC sample exhibits two definite peaks at energies of -1.65 and -3 eV on the energy scale. The larger (high energy) peak is associated with excitation from the maximum in the valence band density of states. The smaller (low energy) peak is associated with excitation to a

maximum in the conduction band density of states. The electron affinity of the vacuum cleaved sample is higher than for any of the other samples.

The T sample was prepared and tested by the methods described in Chapter IIB3 and Chapter IIC. The CdS surface was prepared by cleaving in air. Within one to twelve hours after cleaving, the sample was installed in a glass envelope and a rough pressure of 10^{-3} torr was established. Approximately ten hours were required to reduce the pressure to the 10^{-8} torr range using an oil-diffusion pump and a liquid nitrogen trap. During this time, the assembly was baked at 140°C . The assembly was returned to room temperature when the pressure stabilized and, then, the tube was sealed off. The energy distribution curve from this surface (marked T) has peaks at the same energy levels as the VC energy distributions. The high energy peak is now much smaller than the low energy peak in contrast with the VC curve. In addition, both peaks are much broader than before. Additional peaks appear at relative energies of -3.9 and -4.5 eV. The peak at -3.9 eV is associated with the conduction band and is peculiar to samples which have been exposed to contamination. It is strongest for the T samples. The peak at -4.5 eV results from the exposure of the sample to ultraviolet radiation as described in more detail in a later section. The electron affinity is approximately 0.8 eV smaller than for the VC sample and is found to decrease with ultraviolet radiation. Even though the T sample was cleaved

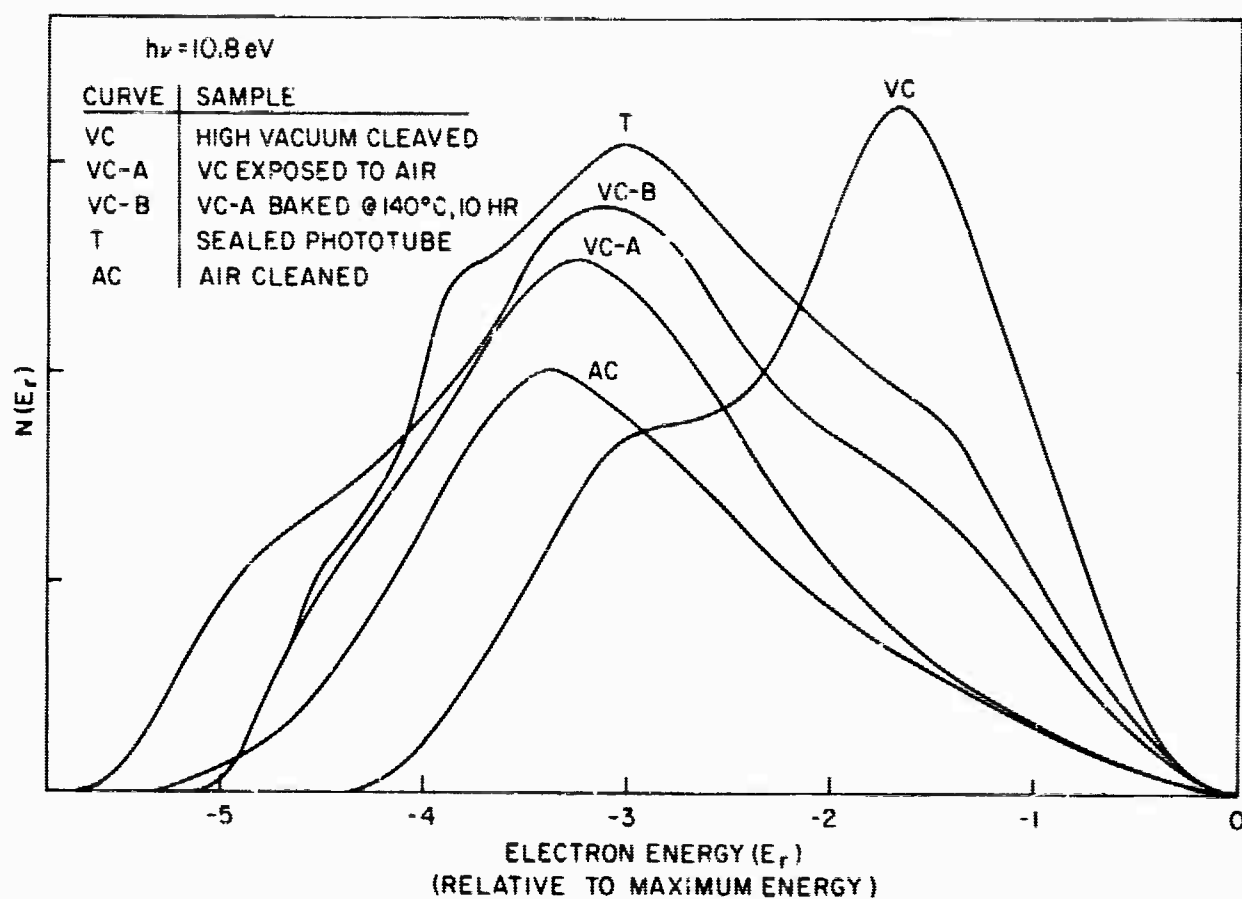


FIG. 68. COMPARISON OF ENERGY DISTRIBUTIONS AT $h\nu = 10.8 \text{ eV}$ FROM CdS SURFACES PREPARED BY DIFFERENT METHODS.

in air, it exhibited many features characteristic of photo-emission from VC CdS.

A CdS sample AC was cleaved in air and tested in low vacuum in attempt to extend the useful range of measurements to photon energies beyond the cutoff of LiF at 11.8 eV. It was then mounted in a windowless metal test chamber. The test chamber was evacuated and then connected to the main chamber of the vacuum monochromator within five minutes after the sample was cleaved. Due to the hydrogen arc, the main chamber contained principally hydrogen. The pressure was maintained at about 10^{-4} torr by continuous pumping with an oil-diffusion pump. The AC energy distribution is considerably different from the VC energy distribution. The high energy peak associated with excitation from the valence band has completely disappeared. The low energy peak appears at a lower energy level than before and is very broad. The apparent electron affinity is about the same as for the T sample. The energy distribution cannot be used to analyze the band structure of CdS.

A VC sample which had been tested was subsequently exposed to air for the VC-A measurements. The measurements were made to determine the extent to which the environment of the vacuum monochromator affected the AC measurements. In addition, the sample was later used in an attempt to simulate the processing of the T samples. The VC-A sample was exposed to air from the atmosphere for a period of two days. Then, the test

chamber was evacuated to a pressure of about 10^{-9} torr and photoemission measurements were made. The VC-A energy distribution is very similar to the AC energy distribution. A broad low energy peak appears at a slightly different energy level. The electron affinity is about the same as for the T and AC samples.

Simulation of the preparation of the T sample was accomplished by baking the VC-A sample for ten hours at a temperature of 140°C . The high vacuum test chamber was pumped continuously. The VC-B measurements were made after the sample had cooled to room temperature. The structure observed in both the VC and the T samples has reappeared with approximately the same strength as in the T energy distribution. A new peak that can be associated with conduction band structure has appeared near -4.7 eV. The electron affinity is smaller than for any of the other samples. This suggests that the important step in preparation of the T samples is the low temperature bake. (A higher temperature could not be used because of the contacts.) The yield curves for VC, AC, and T samples are compared in Fig. 69. The LVC curve is discussed in the next section. The yield curve rises much more slowly for the AC sample but reaches approximately the same final quantum yield near 11.5 eV. Inflections appear in the threshold region of the curves at approximately the same photon energies. This suggests that the optical excitation is not a strong function of surface history. The changes in threshold

energy are in approximate agreement with the changes in electron affinities deduced from the energy distribution curves.

From the above comparison of the energy distribution and yield curves, it can be concluded that the band structure of CdS remains basically unchanged by exposure to air. In other words, the conditions for optical excitation do not appear to be greatly affected. The major differences in the curves are believed to result from changes in the conditions for the escape of the electrons after excitation including changes in the elastic scattering mean free path, the probability for internal reflection of the electron at the surface, and the electron affinity.

One possible mechanism for the changing escape conditions is the diffusion of gaseous impurities into the CdS. This diffusion could occur since the CdS lattice is sufficiently loosely packed so that atoms the size of oxygen or nitrogen could be present and diffuse interstitially. It is hypothesized that the presence of interstitial atoms can reduce the scattering mean free path for elastic collisions. As a result of this change, the attenuation length would also be reduced as can be seen from the results of age theory or the Monte Carlo calculations (see Chapter IIIC2). This phenomenon would allow peaks in the energy distribution curves to appear at the same energy level due to optical excitation and would explain the variation in the peak heights and widths on the basis of scattering.

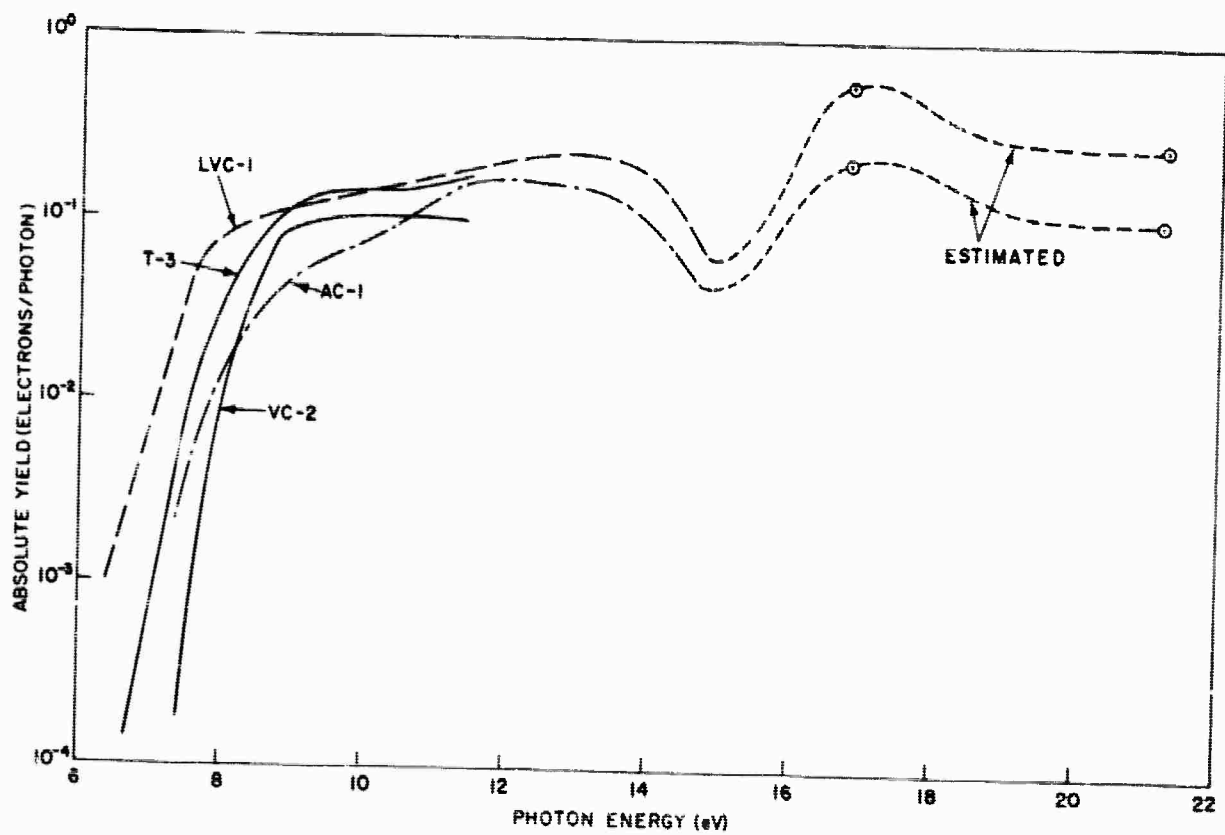


FIG. 69. COMPARISON OF ABSOLUTE QUANTUM YIELD CURVES FROM CdS SURFACES PREPARED IN DIFFERENT WAYS.

The relationship between the elastic scattering mean free path ℓ_p , the inelastic scattering mean free path ℓ_e , and the attenuation length $L(E)$ can be seen by reference to Fig. 29 which resulted from the Monte Carlo calculations. Qualitatively, a decrease in ℓ_p causes an increase in the average integrated distance traveled by an electron before reaching the surface. This increases the probability that an inelastic scattering event will occur before the electron reaches the surface. If Fig. 29 is used in conjunction with Fig. 61 and Eq. (67), the effect of the changes in attenuation length on an energy distribution curve can be seen. For the uncontaminated surface the high energy peak appears in an energy range where scattering is not important, or where it is just starting to be important. If the phonon mean free path decreases after exposure, the effects will start to appear at the high electron energies, causing the high energy peaks to be attenuated more than the low energy peaks.

The energy gained or lost in an elastic scattering event is small but finite. If many elastic scattering events occur on the average before an electron reaches the surface, peaks in the energy distributions will be broadened.

The change in electron affinity is believed to be the result of a reaction at the surface (on an atomic scale). One possible explanation of this is that oxygen atoms might replace the sulfur atoms in the atomic layer just behind the surface. Since the oxygen atom is smaller and more

electronegative than sulfur, an electric dipole could be established which would reduce the electron affinity. Water vapor cannot be ruled out as the cause of the change in electron affinity. The lowest electron affinity occurred for the LVC sample discussed in the next section.

C. SURFACE EFFECTS ON THE LOW-VACUUM-CLEAVED SAMPLE

A CdS sample has been cleaved in the vacuum of the vacuum monochromator by using the high vacuum test chamber with the LiF window and the high vacuum pumping equipment removed. Energy distributions were measured within two to three minutes after the sample was cleaved. The LVC energy distribution is compared with that for a VC sample in Fig. 70. Peaks appear in the LVC energy distribution which correspond to the high and low energy peaks in the VC energy distribution. An additional peak which can be associated with conduction band structure appears at -4.5 eV on the energy scale. The peaks are somewhat broader than for the VC sample. The relative heights of the two peaks which can be compared lie between those for the VC sample and those for the T sample. The electron affinity is lower than for any of the other samples discussed in the previous section.

The LVC yield curve is compared in Fig. 69 with the curves discussed in the previous section. It exhibits the same general features except that the yield reaches a value of 0.1 electrons/photon at a lower photon energy due to the reduction of electron affinity. An inflection appears in this yield curve

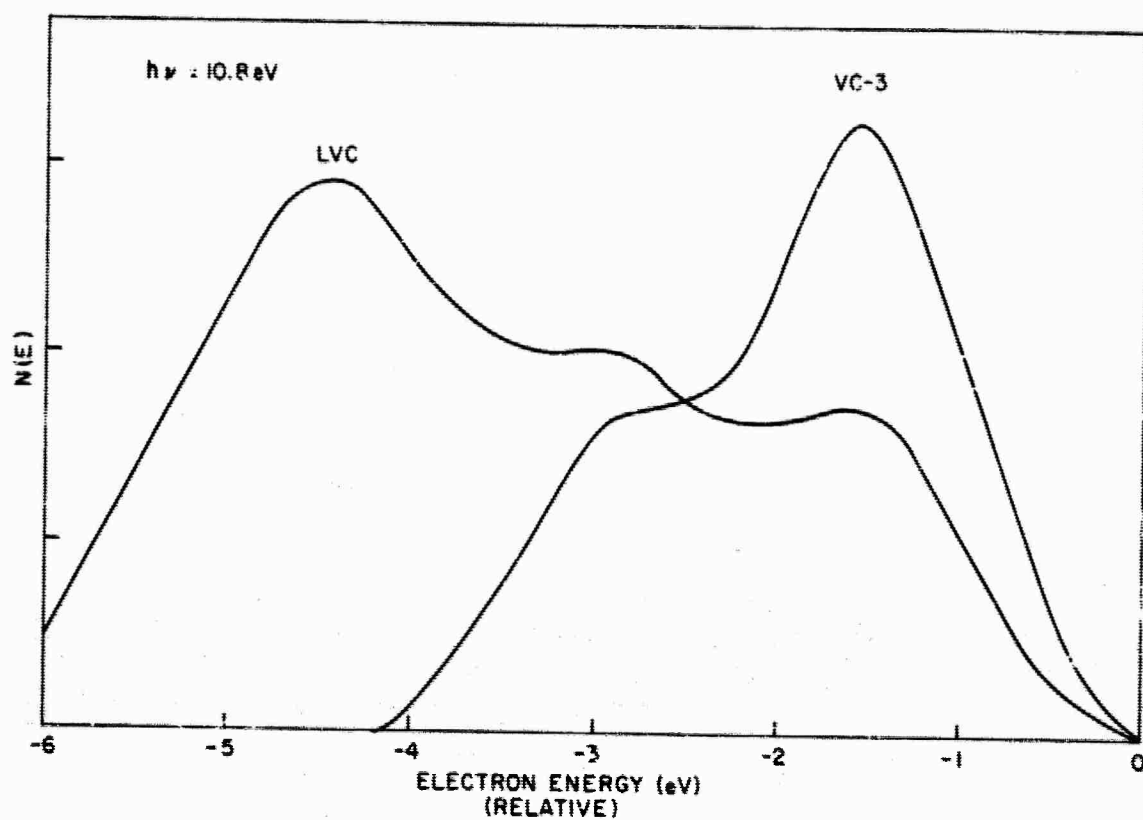


FIG. 70. COMPARISON OF ENERGY DISTRIBUTIONS FROM HIGH-VACUUM-CLEAVED AND LOW-VACUUM-CLEAVED CdS AT $h\nu = 10.8 \text{ eV}$.

at approximately the same photon energy as in the other curves near $h\nu = 7.8$ eV. The yield in the high energy region above 14.2 eV is considerably larger than for the AC sample.

From these comparisons it can be concluded that the interpretation of the LVC curves in terms of band structure is basically correct provided that the difference in scattering is considered. It also appears that the surface reaction which occurs in air tends to protect the surface from the larger effect which lowers the electron affinity of the low-vacuum-cleaved sample as compared with the high-vacuum-cleaved sample.

D. EXPOSURE OF CdS TO N_2 AND O_2

An attempt has been made to determine the constituents of air which contribute to the observed changes discussed in Sec. B. A CdS sample freshly cleaved in high vacuum was subsequently exposed to either N_2 or O_2 obtained from one liter Linde pure gas flasks. The experimental details are discussed in Chapter IID. The forechamber of the vacuum system was flushed several times with the pure gas before the gas was admitted to the main test chamber. The sample was exposed to the gas at a given pressure for a selected period of time. Then the test chamber was evacuated and measurements were made.

If the samples were exposed to pressures of the order of 10 to 50 torr for about thirty minutes before making the measurements, only a small change appeared in the energy

distributions. The relative heights of peaks changed and a small decrease in the electron affinity was observed. The shift in electron affinity was slightly larger for O_2 than for N_2 and was of the order of 0.2 to 0.4 eV as shown in Fig. 71.

A sample which was exposed to oxygen in the same manner after exposure to nitrogen did not exhibit as large a shift in electron affinity. When this sample was exposed later to oxygen at a pressure of 50 torr for about twelve hours, a noticeable decrease in electron affinity occurred. Energy distributions for the high vacuum cleaved sample, for the same sample after exposure to nitrogen, and for the sample after further exposure to oxygen are shown in Fig. 72, plotted as a function of the electron energy E_b corresponding to the applied voltage. Note the difference in the collector work function resulting from exposure to the gas.

The results of these experiments are not conclusive since only a small number of experiments have been done and since the experimental conditions have not been exactly duplicated for the two gases. This information is presented to indicate the capability of observing small changes in surface conditions by using photoemission measurements.

E. THE EFFECT OF ULTRAVIOLET RADIATION

A pronounced decrease of electron affinity induced by exposure to ultraviolet light was observed in the CdS samples mounted in a sealed phototube. This effect is illustrated

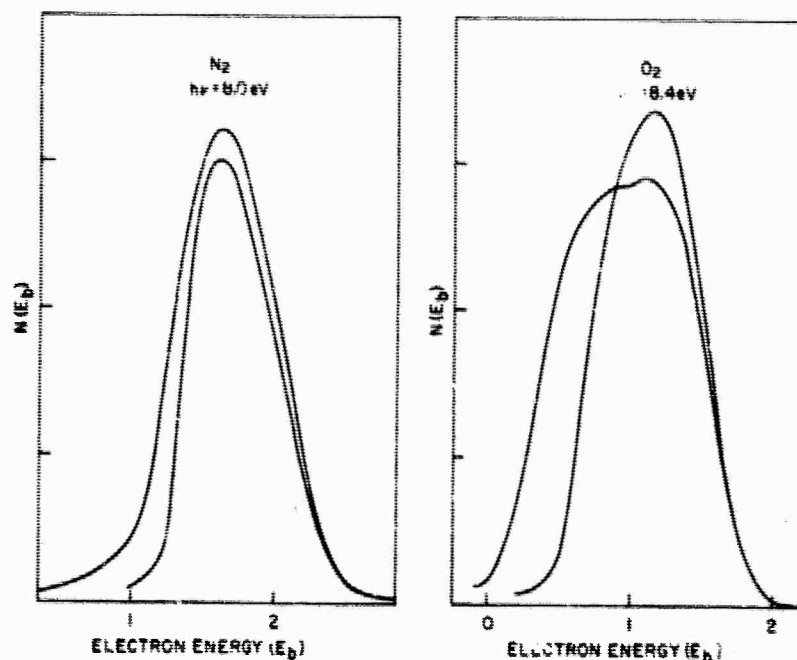


FIG. 71. COMPARISON OF THE EFFECTS OF EXPOSING CdS TO O₂ OR N₂ FOR A SHORT TIME.

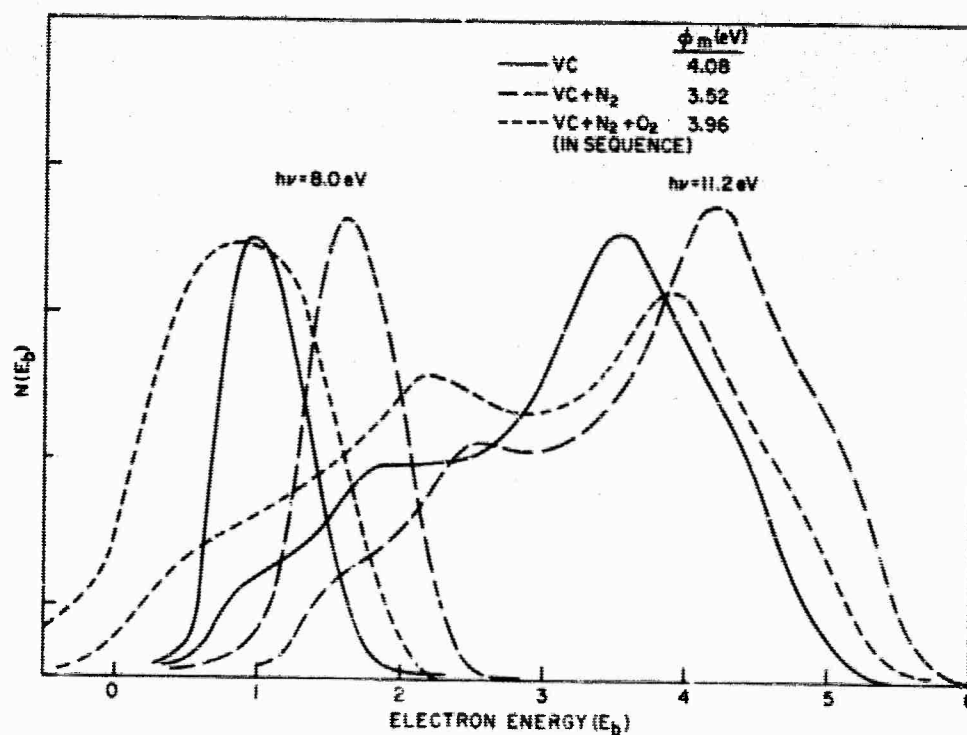


FIG. 72. COMPARISON OF ENERGY DISTRIBUTIONS AT $h\nu = 8.0$ AND 11.2 eV FROM A FRESHLY CLEAVED CdS SURFACE, THE SAME SURFACE EXPOSED TO NITROGEN, AND THE SAME SURFACE EXPOSED TO OXYGEN AFTER THE NITROGEN WAS REMOVED.

in Fig. 73. The photon energy threshold for the reaction lies between 8 and 10 eV. A sample exposed to a given integrated photon flux at about 8 eV did not exhibit the effect. However, exposure to the same integrated photon flux at 10.2 eV did cause the shift in electron affinity. This phenomenon also appeared but was much weaker in some of the samples exposed to O_2 or N_2 . The cause of this phenomenon is not known.

F. CONCLUSIONS ABOUT SURFACE STUDIES

The most important conclusions which can be drawn from the study of surface effects in photoemission from CdS are the following:

1. Exposure of CdS to air, N_2 or O_2 appears to have no significant effect on optical excitation processes but has a large effect on the electron escape mechanisms involved in photoemission.
2. Air cleaved CdS can be moderately heated in vacuum ($140^\circ C$) to improve the conditions for escape of high energy electrons.
3. Long exposure of high vacuum cleaved CdS to ultraviolet radiation causes no significant changes in the photoemission. The same exposure in the sealed tubes causes a noticeable decrease in the electron affinity. A small effect was noted after exposure in the presence of O_2 or N_2 .

VI. CONCLUSIONS

Photoemission measurements on CdS have been used to determine important features of the band structure. Four maxima in the density of states have been detected directly in photoemission measurements. Two maxima in the valence band density of states occur at -1.2 ± 0.3 eV and at -9.4 ± 0.5 eV.

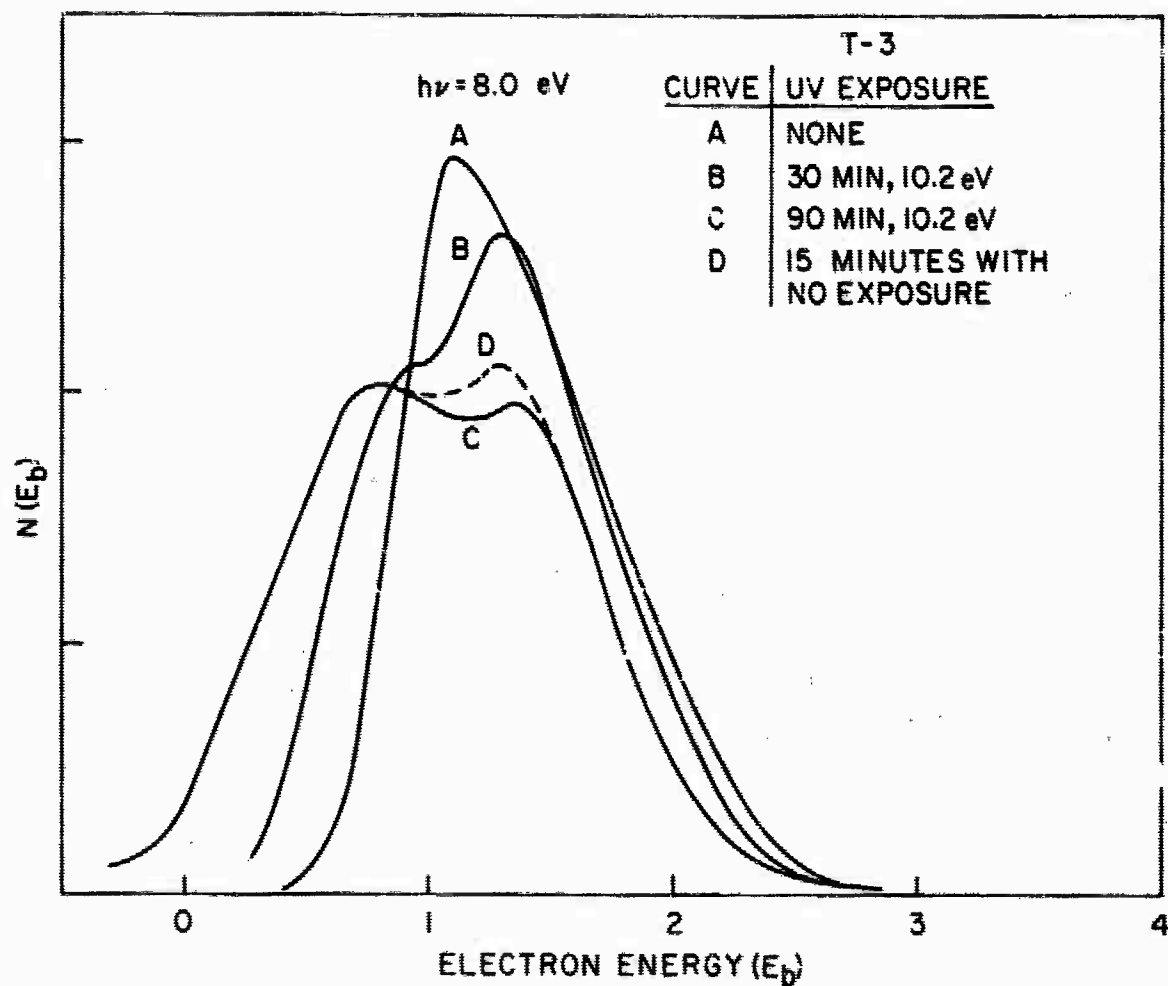


FIG. 73. THE EFFECT OF ULTRAVIOLET RADIATION ON PHOTO-EMISSION FROM A SEALED PHOTOTUBE FOR $h\nu = 8 \text{ eV}$.

The former is probably derived principally from the p-atomic levels of sulfur; whereas, the latter probably is derived principally from the d-atomic levels of Cd. Two maxima in the conduction band density of states are located at 6.7 ± 0.3 eV and at 8.2 ± 0.3 eV above the top of the valence band.

A dip in the quantum yield above 13 eV and the energy distribution of scattered electrons at higher photon energies provide indirect evidence for the location of a third maximum in the conduction band density of states at 4.4 ± 0.5 eV above the top of the valence band. This maximum has been more accurately located by the combined use of reflection and photoemission data.

The sharp structure in the density of states near the top of the valence band and at relatively high energy levels in the conduction band compared with the 2.4 eV band gap of CdS is in general agreement with the band structure calculated by Herman and Skillman [Ref. 14] and may be useful in adjusting parameters in their band structure calculations.

Many details of the density of states have been obtained from the photoemission measurements by assuming that direct conservation of \vec{k} vector is not important and that the matrix elements for optical transitions are constant. There are two probable reasons for the predominance of nondirect transitions. First, the flat bands occurring in the calculated band structure indicate that a summation of a large number of Bloch states is required to represent many of the electronic wave

functions. From this, one can conclude that the Bloch representation may not be the best representation, and, therefore, that the \vec{k} vector resulting from the Bloch representation may not be important in allowing optical transitions. Second, the crystal potential may be nonperiodic as a result of strong electron-lattice interactions again resulting in a breakdown of the Bloch model. The general features of the band structure calculated using the Bloch model still seem to be in general agreement with the experimentally determined band structure.

First order agreement is obtained between optical conductivity calculated from the derived density of states and that determined by Walker and Osantowski [Ref. 7] from reflection measurements. This provides an independent check on the determination of band structure and optical selection rules. The yield calculated from the density of states is also in first order agreement with the measured yield.

A qualitative indication of the broadening occurring due to the combined effects of scattering, band bending, and measuring techniques can be obtained by comparing the derived density of states with the sharpened density of states which gave more detailed agreement with the optical conductivity.

The investigation of the effects of surface conditions on the photoemission measurements from CdS has provided useful information about surfaces, and has served as a guide for the interpretation of the data from surfaces prepared by different

methods. It has been found that optical excitation is not greatly affected by the surface conditions studied. The effects of air on a sample can be partially reversed by baking the sample in vacuum at a moderate (140°C) temperature. Scattering due to gas atoms or molecules which diffuse into the surface is suggested as the most probable cause of broadening and loss of structure. Theoretical study of the effects of band bending on energy distributions indicate that band bending can introduce broadening. Because of the small absorption length in CdS, however, band bending does not produce a large effect in the observed location of peaks.

The experimental techniques and equipment developed are applicable to the study of many other II-VI compounds by photoemission measurements. The continued systematic study of the cubic and hexagonal crystals in this class of compounds is necessary to determine the role played by crystal symmetry as compared with the role played by the constituent atoms in determining the band structure of the compounds.

REFERENCES

1. Iu. A. Shuba, Soviet Phys. Tech. Phys., 1, 1103, 1956.
2. W. E. Spicer, J. Phys. Chem. Solids, 20, 134, 1961
3. J. J. Scheer and J. van Laar, Phillips Res. Repts., 16, 323, 1961.
4. V. F. Bibik, Ukrayin, Fiz. Zh., (USSR), 7, 643, 1962.
5. M. Cardona, Phys. Rev., 129, 1068, 1963.
6. M. Cardona, Solid State Comm., 1, 109, 1963.
7. W. C. Walker and J. Osantowski, J. Phys. Chem. Solids, to be published.
8. W. C. Walker, in preparation.
9. J. F. Hall, J. Opt. Soc. Am., 46, 1013, 1956.
10. R. H. Bube, Photoconductivity of Solids, John Wiley and Sons, Inc., New York, 1960.
11. R. Williams, J. Phys. Chem. Solids, 23, 1057, 1962.
12. G. Wlerick, Physica, XX, 1099, 1954.
13. K. W. Böer, Physica, XX, 1103, 1954.
14. F. Herman, Proc. of the International Conference on Semiconductor Physics, Prague, 1960, p. 20.
15. F. Herman, et al, Phys. Rev. Lett., 11, 541, 1963.
16. J. L. Birman, Phys. Rev., 109, 810, 1958.
17. J. L. Birman, Phys. Rev. Lett., 2, 157, 1959.
18. J. L. Birman, Phys. Rev., 114, 1490, 1959.
19. J. L. Birman, Phys. Rev., 115, 1493, 1959.
20. A. F. Joffé, J. Phys. Chem. Solids, 8, 6, 1959.
21. R. A. Smith, Wave Mechanics of Crystalline Solids, John Wiley and Sons, Inc., New York, 1961, p. 346.

22. C. Herring, Proc. of the International Conference on Semiconductor Physics, Prague, 1960.
23. J. Mort and W. E. Spear, Phys. Rev. Lett., 8, 314, 1962
24. W. E. Spicer, Phys. Rev. Lett., 11, 243, 1963.
25. L. Apker, E. A. Taft, and J. Dickey, J. Opt. Soc. Amer., 43, 78, 1953.
26. W. E. Spicer, J. Phys. Chem. Solids, 22, 365, 1961.
27. P. Williams, J. Phys. Chem. Solids, 22, 129, 1961.
28. R. W. G. Wyckoff, Crystal Structures, Interscience Publishers, New York, 1948, Ch. III, illus. p. 4.
29. H. Lipson and W. Cochran, The Determination of Crystal Structures, G. Bell, London, 1953.
30. P. Bardell, private communication.
31. C. A. Mead and W. G. Spitzer, Appl. Phys. Lett., 2, 74, 1963.
32. C. N. Berglund, "Band Structure and Electron-Electron Interactions in Copper and Silver - Photoemission Studies," Rept. SEL-64-053 (TR No. 5205-1) Stanford Electronics Laboratories, Stanford, California, June 1964, p. 25.
33. A. M. Smith, "Investigations of Photoconductivity and Photoemission in Lead Sulfide in the Vacuum Ultraviolet," Ph.D. Dissertation, Institute of Optics, The University of Rochester, Rochester, New York, 1961, p. 116.
34. W. E. Spicer, private communication.
35. K. Watanabe and C. Y. Inn, J. Opt. Soc. Amer., 43, 32, 1953.
36. R. E. Simon, E. K. Gatchell, C. R. Fuselier, Research in Electron Emission from Semiconductors, Rept. No. 18, Contract DA36-039AMC-02221(E), 2nd Quarterly Report, RCA Laboratories, Princeton, New Jersey, Nov 1963, p. 15.
37. W. E. Spicer and C. N. Berglund, in preparation.
38. T. S. Gray, Applied Electronics, John Wiley & Sons, Inc., New York, 1953, p. 143.
39. L. Apker, E. Taft, and J. Dickey, Phys. Rev., 74, 1462, 1948.

40. W. E. Spicer, Phys. Rev. Lett., 9, 385, 1962; and references therein.
41. W. E. Spicer, RCA Rev., 19, 555, 1958.
42. W. E. Spicer, J. Appl. Phys., 31, 2077, 1960.
43. J. J. Scheer, Philips Res. Repts., 15, 584, 1960.
44. J. van Laar and J. J. Scheer, Philips Res. Repts., 17, 101, 1962; J. van Laar and J. J. Scheer, Zeit. f. Phys., in press.
45. J. J. Scheer and J. van Laar, Phys. Lett., 3, 246, 1963.
46. F. G. Allen and G. W. Gobell, Phys. Rev., 127, 19, 1962.
47. D. Redfield, Phys. Rev., 124, 1809, 1961.
48. A. J. Dekker, Solid State Physics, Academic Press, Inc., New York, 1958, Ch. 17.
49. C. N. Berglund and W. E. Spicer, in preparation.
50. J. C. Phillips, D. Brust, and F. Bassini, Phys. Rev. Lett., 9, 389, 1962; J. C. Phillips, Phys. Rev., 133, A452, 1964; D. Brust, Phys. Rev., 134, A1337, 1964.
51. C. J. Delbecq, B. Smaller, and P. H. Yuster, Phys. Rev., 111, 1235, 1958.
52. B. Davidson, Neutron Transport Theory, Oxford University Press, New York, 1958.
53. R. Stuart, F. Wooten, W. E. Spicer, Monte Carlo Calculations Pertaining to the Transport of Hot Electrons in Metals, UCRL-7626, University of California, Lawrence Radiation Laboratory, Livermore, California, Jan. 17, 1964.
54. C. Herring and M. H. Nichols, Rev. Modern Phys., 21, 185, 1949.
55. A. H. Sommer and W. E. Spicer, "Photoemission," Photoelectric Effects, ed. S. Larach, D. van Nostrand, in press.
56. G. C. Dousmanis and R. C. Duncan, J. Appl. Phys., 12, 1627, 1958.
57. W. E. Spicer and N. B. Kindig, Solid State Communications, 2, 13, 1964.
58. F. Herman, private communication.

59. W. E. Spicer, Proc. IEEE, 51, 1119, 1963.
60. W. E. Spicer, Phys. Rev., 112, 114, 1958.
61. D. Redfield, Phys. Rev., 130, 914 and 916, 1962.
62. D. L. Dexter, Nuovo Cimento Suppl., VII, 245, 1958.
63. E. O. Kane, Phys. Rev., 127, 131, 1962.